Localization Model description of interfacial dynamics of free-standing nanoparticles and thin films, and nanoparticle on supporting interacting substrate

by

Gazi Arif Mahmud

A thesis submitted in partial fulfillment of the requirements for the degree of

Doctor of Philosophy

in

Materials Engineering

Department of Chemical and Materials Engineering

University of Alberta

Abstract

Localization model (LM) relates, without any free parameter, slow dynamics of α-relaxation time (τ_α) to fast dynamics of Debye-Waller Factor (DWF) or $\langle u^2 \rangle$, which is the mean square displacement of particles at a caging time on the order of picoseconds. Moreover, localization model can also predict the diffusion coefficient D when combined with the 'decoupling' or Fractional Stokes-Einstein (FSE) relation linking τ_α to D. Recently, this excellent model has been proven to be useful to predict τ_α and D of Cu-Zr metallic glass with wide range of compositions from $\langle u^2 \rangle$ without any free parameter over a wide range of temperature. Later, the same model is tested for crystalline UO_2 under superionic conditions. In the present work, we begin with testing LM for free-standing $Cu_{64}Zr_{36}$ metallic glass thin films (MGTF) of different thicknesses. We tested LM in overall MGTF, in interfacial region of MGTF where particles have higher mobility, and core or inside of MGTF where particles have less mobility. Free surface of crystalline metallic materials has dynamics similar to the amorphous materials. Hence, in addition to MGTF, we tested this model for interfacial regions of free-standing crystalline Cu thin films with different crystallographic orientation of free surface. After successfully testing LM for overall free-standing $Cu_{64}Zr_{36}$ MGTFs and their interfaces and cores, we continued the usefulness of this model for the interfacial regions, core, and overall of free-standing $Cu_{64}Zr_{36}$ metallic glass nanoparticles (MGNP) with different sizes and interfacial regions Cu nanoparticles with different sizes. Finally, we tested this model for interfacial regions, both free interface and Cu-C interface region of Cu NP, of Cu nanoparticles supported on interacting graphene substrate with varying interaction strength between Cu atoms of nanoparticle and C atoms of graphene substrate. We found this model to be very useful to estimate slow dynamics of τ_α and D to the fast dynamics of

DWF for all the cases we studied. In addition to the localization model, we conduct detailed study interfacial dynamics of free standing $Cu_{64}Zr_{36}$ metallic glass thin films and nanoparticles and crystalline Cu thin films and nanoparticles. Especially, we focused on the interfacial dynamics of Cu NP supported on an interactive supporting graphene substrate and the effects of substrate on the overall dynamics of Cu NP. Moreover, we show that Tammann Temperature (T_{TA}), the minimum temperature for free interface to have enhanced mobility of particles, can be obtained from the intersection of extrapolated $\langle u^2 \rangle$ curves of core and interface. We found that the supporting graphene substrate lowers both melting temperature and Tammann temperature of supported Cu NP indicating the higher interfacial activities and, as a result, higher catalytic activities of supported Cu NP.

Preface

This thesis is based on an international research collaboration directed by Professor Hao Zhang of the University of Alberta, Edmonton, Alberta, Canada and Dr. Jack F. Douglas of the National Institute of Standards and Technology (NIST), Gaithersburg, Maryland, USA.

Chapter 3 of this thesis has been published as Gazi A Mahmud, Hao Zhang, Jack F Douglas, "Localization Model Description of the Interfacial Dynamics of Crystalline Cu and $Cu_{64}Zr_{36}$ Metallic Glass Films", Journal of Chemical Physics, 2020, 153 (12), 124508. Chapter 4 has been published as Gazi A Mahmud, Hao Zhang, Jack F Douglas, "Localization Model Description of the Interfacial Dynamics of Crystalline Cu and $Cu_{64}Zr_{36}$ Metallic Glass Nanoparticles", European Physical Journal (EPJ) E 2021, 44 (3), 33. Chapter 5 has recently been published as Gazi A Mahmud, Hao Zhang, Jack F Douglas, "The Dynamics of Metal Nanoparticles on a Supporting Interacting Substrate", Journal of Chemical Physics, 2022, 157, 114505.

The idea of this research was initiated by Dr. Hao Zhang and Dr. Jack F Douglas. I was responsible for running simulations, data collection, data analysis under direct supervision of Professor Hao Zhang. The manuscripts were written by me, Professor Hao Zhang and Dr. Jack F. Douglas.

Acknowledgement

First of all, it is my pleasure to express my appreciation to my supervisor Professor Hao Zhang. His passionate guidance, deep knowledge on computational materials engineering, surface science, and molecular dynamics simulation made it possible to finish this research. He was especially helpful during the lockdown due to the global CoViD19 pandemic for two years of my PhD study. I would like to thank Professor Phillip Choi and Professor Hongbo Zeng for all their supports during this study. I would also like to appreciate the help from my group members, especially Dr. Mohammad Khalkhali and Dr. Xinyi Wang. I also like to acknowledge the financial supports from the Natural Sciences and Engineering Research Council of Canada.

Contents

List of Figures

Chapter 1

Chapter 2

Chapter 3

Chapter 4

Chapter 5

Chapter 1: Introduction

First known history of glass making dated back to 3500BC in ancient Mesopotamia and Egypt. It is impossible to recognize modern word without glasses due to their wide varieties of uses including window panels, mirror, eye-glasses, drinking pots, decorative items, light bulbs, TV screen, smartphone screen, computer screen, fiber optic cables, amorphous semiconductors, and so on [1]. In addition to transparency, heat resistance and chemical resistance, Glasses are recyclable multiple times and easy to deform into desirable shapes at higher temperature. Besides regular glasses, metallic glass or amorphous metal or metal alloys are a new addition to modern material technology. Incredible properties of glasses are drawing attentions of manufacturers and researchers for thousands of years.

One of the very important properties of glass that allows us to give it very complex structural shapes is its as much as 20 orders of magnitude deviation in viscosity (η) over ~200K temperature variation [2]. Viscosity of glass-forming liquid increases upon cooling from high temperature and sharply increases below glass-transition temperature (T_g). Cooling below this glass transition temperature results solidification at amorphous state, called glass. Glass-formation is in the center of attention of scientific community for hundreds of years due to its importance on development of new fabrication processes, yet, knowledge of glass-formation is still limited to

date [1]. One of the very important aspects of glass-formation is structural relaxation. First, we will discuss about structural relaxation of glass and theory of glass-formation.

1.1 Structural Relaxation of Glass

Any material in liquid state under liquidus temperature is called super-cooled liquid (SCL). This metastable super-cooled liquid state exists between glass-transition temperature (T_g) and melting temperature (T_m). Further cooling of SCL below the T_g results freezing of SCL structure which is non-crystalline and thermodynamically unstable. This unstable non-crystalline disordered solid is called glass which spontaneously relaxes to become SCL and eventually crystallize [3,4]. The rate of relaxation depends on temperature, pressure, and chemical composition. There are different types of structural relaxations including the slowest α-relaxation or primary relaxation and fast β-relaxation or secondary relaxation. α-relaxation is very slow process at lower temperature and can be in a scale of minutes [5–9]. Figure 1.1 shows relaxation times of glass-forming liquid at high and low temperature. In the very beginning, particles move ballistically before any collision with neighboring particles for a very small period of time. After that, particles start colliding with neighboring particles and they become "caged" where β-relaxation happens. Finally, α-relaxation takes place where large-scale particle diffusion and momentum diffusion take place.

α-relaxation time allows us to understand basic glass-formation processes and characteristic temperatures related to glass formation. Knowing relaxation time is also important for many industrial and scientific applications including annealing, tempering, vitrification, study of metallic glasses, optical fibers, and so on [5] because relaxation time affects many properties of metallic glasses – electrical, magnetic, elastic, viscoelastic, corrosion, etc. [10,11].
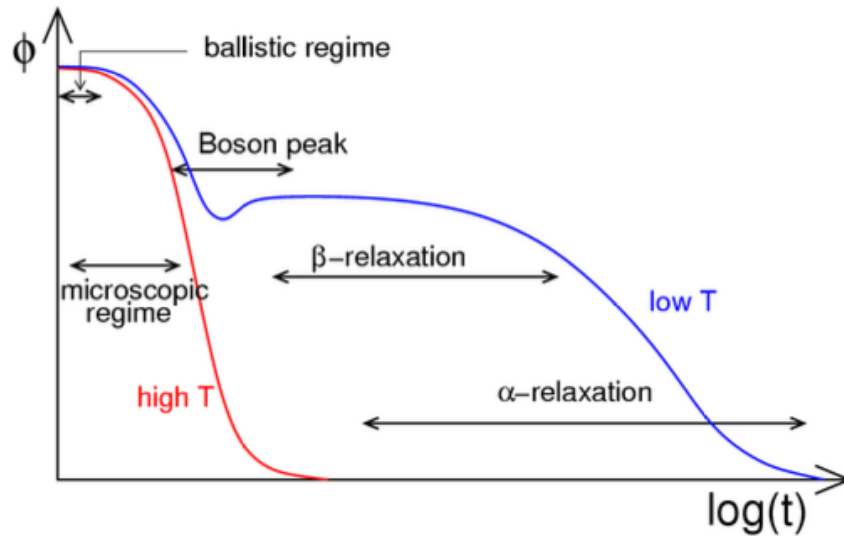
Figure 1.1: Relaxation times over time of glass-forming liquid at high and low temperatures. [12]

Fourier transform of the van Hove correlation function or atom displacement distribution function, $G_s(r, t)$ gives the self-intermediate scattering function (SSIF), [13]

$$F_s(q, t) = \langle exp\{-i\boldsymbol{q}[\boldsymbol{r_i}(t) - \boldsymbol{r_i}(0)]\}\rangle \qquad (1.1)$$

3

α-relaxation time (τ_α) can be estimated from F_s (q, t) by fitting the curve using the equation,[14]

$$F_s(q, t) \propto exp\left[-(t/\tau_\alpha)^{\beta_s}\right] \qquad (1.2)$$

where, β_s is a fitting parameter and $0 < \beta_s < 1$. The value of β_s is not apparent, but there is general trend in β_s values of glass-forming liquids.

1.2 Theory of Glass-Formation

Theories of glass-formation is continuously evolving, however, some of the basic theories are crucial to understand the glass-formation. Simon and Kauzmann concluded that the sudden increase in viscosity as well as α-relaxation time during glass-formation are associated with the sudden decrease in entropy of glass-forming (GF) liquids [15]. Adam and Gibbs hypothesized that, there are "cooperatively rearranging regions (CRR)" or "dynamic clusters" in GF liquids that grows upon cooling and as a result, structural relaxation time increases and diffusivity decreases sharply [16]. According to Adam-Gibbs (AG) theory of glass-formation, the activation energy of relaxation, $\Delta G_a = z \Delta \mu_a$, where, z is the "size" or number of particles in CRR and $\Delta \mu_a$ is the activation free energy temperature high enough where there is no cooperative motion of particles. Furthermore, AG theory proposed that z is inversely proportional to the configurational entropy,

S_c, such that $z = S_c^*/S_c$, where, S_c^* is the high temperature limit of $S_c(T)$. Based on AG theory, α-relaxation time can be estimated by the AG relation,

$$\tau_\alpha = \tau_0 exp[\beta \Delta G_a] = \tau_0 exp[\beta \Delta \mu_a z] = \tau_0 exp\left[\frac{\Delta \mu_a}{k_B T} \cdot \frac{S_c^*}{S_c}\right] \qquad (1.3)$$

where, β is a temperature dependent constant and τ_0 is the limiting relaxation time at high temperature which has expected value of $O(10^{13})$. This relation between fluid configurational entropy and structural relaxation time is known as Generalized Entropy Theory (GET).

Debye-Waller Factor (DWF) or $\langle u^2 \rangle$ which is the mean square displacement of particles in very small time when particles are "caged". We will discuss about DWF or $\langle u^2 \rangle$ in detail later. $\langle u^2 \rangle$ can be related to the configurational entropy by the relation, $S_c T \sim \langle u^2 \rangle$. Combining this relation and AG relation gives the Buchenau relation,

$$\tau_\alpha \approx \tau_0 exp(u_0/\langle u^2 \rangle) \qquad (1.4)$$

where u_0 is an adjustable constant [1,17].

Hall and Wolynes (HW) derived the simple relation between τ_α and $\langle u^2 \rangle$ from Random First Order Transition (RFOT) that suggests a near linear relationship between $log\tau_\alpha$ and $1/\langle u^2 \rangle$ [8,18–20], which gives us the same relationship is –

$$\tau_\alpha \sim exp(u_0^2/\langle u^2 \rangle) \qquad (1.5)$$

where, u_0^2 is the minimum particle oscillation distance to escape it's cage [18].

1.3 Characteristic Temperatures of Glass Formation

In order to have deeper knowledge on glass formation, we must understand some characteristic temperatures of glass-formation. We can obtain characteristic temperatures of glass-formation from generalized entropy theory (GET) as well as directly from $\langle u^2 \rangle$. Figure 1.2 shows $\langle u^2 \rangle$, normalized by the square of average interparticle distance, σ, of bulk $Cu_{64}Zr_{36}$ metallic glass, plotted against temperature, T. Inset of the Figure 1.2 shows the displacement vectors of a Cu atom rattling in the free volume.

Characteristic Temperature T_A: Characteristic temperature T_A is the temperature above which τ_α has Arrhenius dependence with T and below which τ_α follows VFT relation with T. T_A is the lowest temperature for atoms to become caged [18] and particles exhibit high temperature behavior of liquid above this temperature [1]. According to GET,

$$\Delta H_a(T)/\Delta H_a(T_A) \approx 1 + C(T/T_A - 1)^2 \qquad (1.6)$$

where $\Delta H_a(T)$ is the activation enthalpy at any T above T_c and below T_A, $\Delta H_a(T_A)$ is the apparent activation enthalpy at T_A and C is the measure of fragility at higher T. Previous study on Cu-Zr bulk metallic glass with range of compositions shows $\Delta H_a(T)/\Delta H_a(T_A)$ follows linear relation with $(T/T_A - 1)^2$. We can estimate T_A from the fitting of this plot [14].

Glass-transition Temperature, T_g: At glass-transition, primary relaxation time, τ_α is in the order of 100 s [21]. Therefore, T_g can be determined experimentally. Also, T_g can be determined from another characteristic temperature T_A because,

$$T_g = (1/2 - 2/3)T_A \qquad (1.7)$$

Cross-over Temperature, T_c: DWF or $\langle u^2 \rangle$ increases with increasing T at lower T but starts to increase faster after cross-over temperature, T_c. So, we can say T_c separates low and high temperature regimes of glass-formation. Details of finding exact value of T_c can be found in the literature [1]. Briefly, T_c can be estimated using the relation,

$$\tau_\alpha / \tau_0 \sim [(T - T_c)/T_c]^{-\gamma} \qquad (1.8)$$

here, τ_0 is the vibrational relaxation time and γ is a scaling exponent.

Vogel-Fulcher-Tammann (VFT) Temperature, T_0: The temperature at which glass-formation is completed is called VFT temperature, T_0. In Figure 1.2, T_0 can be estimated from the intersection of the extrapolated linear fit of $\langle u^2 \rangle$ at low temperature regime and T axis where $\langle u^2 \rangle$ is zero. T_0 can also be estimated from the Vogel-Fulcher-Tammann equation,

$$\tau_\alpha / \tau_{VFT} \sim exp[D_f T_0 / (T - T_0)] \qquad (1.9)$$

here, $1/D_f$ is the fragility of glass-formation above T_g and below T_c. Note that, VFT equation only works between T_c and T_g. Fragility of glass-formation is the strength of temperature dependence of viscosity of glass-forming liquid [2,21,22].
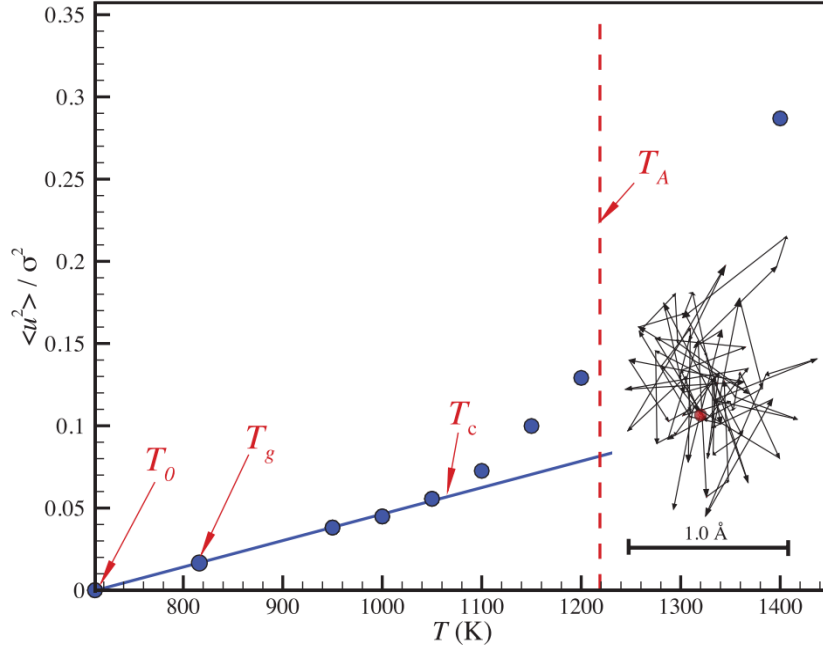
Figure 1.2: Characteristic temperatures are shown on the Debye-Waller Factor (DWF) or $<u^2>$ plot of $Cu_{64}Zr_{36}$ bulk metallic glass (BMG) against temperature, T. Inset is showing the rattling of a caged copper (Cu) atom of $Cu_{64}Zr_{36}$ BMG at 1000K.[8]

1.4 Diffusivity and Debye Waller Factor (DWF) or $\langle u^2 \rangle$

Diffusion coefficient or Diffusivity (D) can be easily determined from the slope of mean square displacement or MSD curve plotted against time from the following equation –

$$D = MSD/6t = \langle \frac{1}{N} \sum_{n=1}^{N} \{(x_i - x_0)^2 + (y_i - y_0)^2 + (z_i - z_0)^2\} \rangle \Big/ 6t \qquad (1.10)$$

Where, (x_0, y_0, z_0) and (x_i, y_i, z_i) are, respectively, initial positions and final position of particles after time t and N is the number of particles.

The very beginning of the MSD curve is the "Ballistic" regime where particles ballistically move with constant velocity for a very short time before any collision between particles take place.

8

After that, in the "caging" regime, particles start to have collision with nearest neighboring particles and as a result, become "caged" for an order of picoseconds (ps) and particles experience "rattling motion" in this regime. Finally, particles start to diffuse, and "Diffusive" regime appears. From the slope of this regime, diffusivity constant (D) can be calculated [23]. Debye-Waller Factor (DWF) or $\langle u^2 \rangle$ is simply the mean square displacement calculated after a short time (t_{cage}) when particles are going through the rattling motion. Free volume, which is related to DWF and estimated by $\langle u^2 \rangle^{3/2}$, is the volume over which the center of a particle can translate. Note that the free volume is different from Voronoi volume or cavity volume [14,24].
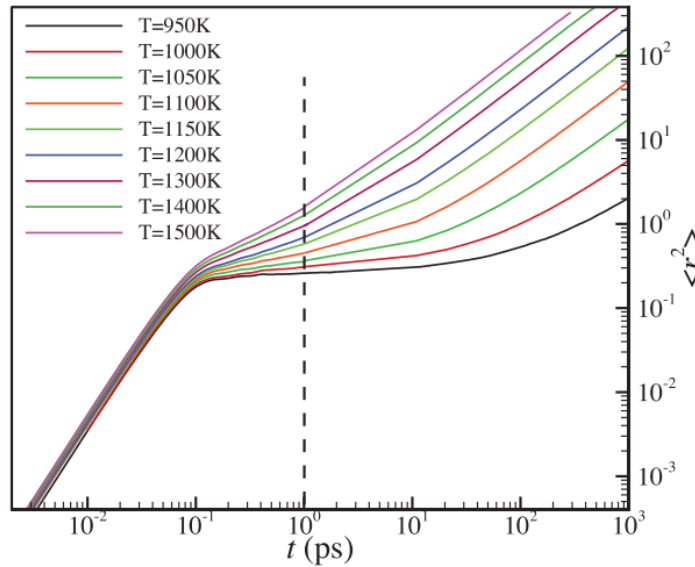
Figure 1.3: Mean square displacement against time plot for $Cu_{64}Zr_{36}$ bulk metallic glass showing ballistic, caging and diffusive regimes . [8]

1.4 Relation between fast and longtime dynamics

So far, we discussed the importance about α-relaxation time (τ_α) and the rapid increase of viscosity as well as τ_α at lower temperature. Unfortunately, determining α-relaxation times can be difficult at lower temperature, especially computationally. However, it is easy to determine DWF or $\langle u^2 \rangle$ both numerically and experimentally. Therefore, we can try to predict long-time or slow dynamics of τ_α from short-time or fast dynamics of $\langle u^2 \rangle$ using HW relation,

$$\tau_\alpha = \tau_0 exp(u_0/\langle u^2 \rangle) \qquad (1.11)$$

After conducting extensive studies to prove this relation, it has been concluded that the HW relation displays a systematic curvature instead of near linear. Thus, an improvement of HW relation was proposed based on the free volume, v_f [4,25,26], where local anisotropy of v_f is emphasized. The classical free volume theory of relaxation relates τ_α to v_f by an exponential relationship [27] –

$$\tau_\alpha = \tau_0 exp(v_0/v_f) \qquad (1.12)$$

where τ_0 and v_0 are constants. But, Starr et al [24] proposed relation between free volume and DWF,

$$v_f \propto \langle u^2 \rangle^{3/2} \qquad (1.13)$$

From the Equation (1.12) and (1.13), we get the proposed modified HW relation,

$$\tau_\alpha(\langle u^2 \rangle) = \tau_u exp\left[(u_0^2/\langle u^2 \rangle)^{\alpha/2}\right] \qquad (1.14)$$

Here, τ_u is a constant prefactor, α is another constant that depends on free volume anisotropy, and u_0^2 is the minimum particle oscillation distance for particles to scape it's cage. The value of α is 3 if the system is not highly anisotropic, but this value can be different for highly anisotropic system.

Notice that the modified HW relation still has free parameters. Later, therefore, unspecified parameters τ_u and u_0^2 have been replaced by the α-relaxation time and $\langle u^2 \rangle$ at the characteristic temperature T_A to derive a very useful relation without any free parameter to predict τ_α from $\langle u^2 \rangle$. We can substitute $u_0^2 = u_A^2 \equiv \langle u^2(T_A) \rangle$ and $\tau_u = e\tau_A \equiv e\tau_\alpha(T_A)$, where e is Euler's number and τ_A is τ_α at T_A, the temperature at which τ_α and τ_β becomes equal. Assuming the system is isotropic, for which $\alpha = 3$, will give us the relation; [18]

$$\tau(u^2) = \tau_A exp\left[(u_A^2 / \langle u^2 \rangle)^{3/2} - 1\right] \tag{1.15}$$

This relation is the Localization Model description to predict long-time slow dynamics of τ_α from short-time fast dynamics of $\langle u^2 \rangle$. Therefore, we need to determine $\langle u^2 \rangle$ at T_A, τ_α at T_A and $\langle u^2 \rangle$ at a particular temperature T to determine τ_α at T, but we don't need any free parameter to find τ_α at T. Later in this report, we will discuss about the characteristic temperature T_A which is the onset temperature where particle caging first emerges.

1.5 Localization Model (LM)

1.5.1 Localization Model to Predict τ_α

The main purpose of the localization model (LM) is to predict α-relaxation time (τ_α), which can be difficult to measure due to its slow nature, directly from fast dynamics of DWF or $\langle u^2 \rangle$ without any fitting parameter. The brief background of this model is described here. Motivated by Hall and Wolynes's [20] computational work and experimental evidence from the research of Buchenau and Zorn's [17] work, Starr et al [24] attempted to describe the relation between relaxation

time and free volume or $\langle u^2 \rangle^{3/2}$. Leporini et al [4,26] and Simmons et al [25] attempted to improve the relationship between relaxation time and DWF, but all of their proposed relations have free parameters which inhibits direct estimation of relaxation time from DWF. Finally, Betancourt et al [18] proposed a relationship between relaxation time and DWF without any free parameter. They derived a relationship which involved relaxation time and DWF at characteristic temperature, T_A.

Localization Model can predict, without any free parameter, α-relaxation time (τ_α) from the mean square atomic displacement $\langle r^2 \rangle$ at a characteristic caging time (t_{cage}) on the order of a ps or DWF ($\langle u^2 \rangle$). The localization model description is shown in the equation below,

$$\tau_\alpha(T) = \tau_\alpha(T_A)exp\left[\{\langle u^2(T_A)\rangle/\langle u^2(T)\rangle\}^{3/2} - 1\right] \tag{1.16}$$

where, $\tau_\alpha(T)$ and $\tau_\alpha(T_A)$ are α-relaxation time at temperature T and T_A respectively, and $\langle u^2(T)\rangle$ and $\langle u^2(T_A)\rangle$ are DWF or $\langle u^2 \rangle$ at temperature T and T_A respectively [8,18,25].

1.5.2 Localization Model to Predict *D*

In order to use localization model to predict diffusion coefficient, we must relate diffusivity (*D*) to relaxation time (τ_α). Previous study on superionic crystalline UO_2 shows the diffusion coefficient of oxygen atoms (D_O) can be relate with τ_α to a good approximation by an inverse relation $D_O/k_B T \sim 1/\tau_\alpha$ [9]. Diffusion coefficient and relaxation time of glass forming liquids generally follows Fractional Stokes–Einstein (FSE) relation [19] given in equation,

$$D/T \sim (\tau_\alpha)^{1-\zeta} \tag{1.17}$$

where ζ is the decoupling exponent of material.

By combining LM relation to predict relaxation time from DWF and FSE relation, we can deduce a new localization model description to relate diffusivity and relaxation time shown below,

$$ln[\{D(T)/T\}/\{D(T_A)/T_A\}] = (1 - \zeta)[\{\langle u^2(T_A)\rangle/\langle u^2(T)\rangle\}^{3/2} - 1] \qquad (1.18)$$

where, $D(T)$ and $D(T_A)$ are diffusion coefficient at temperature T and T_A, respectively.

Previously, Douglas et al [8] tested the localization model for Cu-Zr bulk metallic glass with wide range of compositions and confirmed that α-relaxation time and diffusivity at wide range of temperature can be estimated from DWF without any free parameter. Later, the model was tested by Zang and coworkers [9] to estimate α-relaxation time and diffusivity of superionic crystalline UO₂ from DWF. This time, localization model was tested on wide range of temperature and pressure.

1.6 Motivation and Goal of this Study

Previously, it has been reported for bulk glass-forming Cu-Zr alloys with range of compositions that localization model description can estimate relaxation time and diffusion coefficient from Debey-Waller factor. Later, usefulness of the same model has been proved for Superionic UO₂ crystal [9] which shows many important features similar to glass-forming liquids [28].

The main focus of this computational scientific study is further testing the usefulness of localization model for free interfaces of metallic glass and crystalline metal thin films and nanoparticles, and interface of crystalline metallic nanoparticles and its interacting supporting substrate using molecular dynamics simulation. After studying free standing thin films and nanoparticles, we focused on the interfacial dynamics of nanoparticles on the interacting substrate.

In addition to testing localization model, we also determined Tammann temperature, the temperature at which mobile interfacial layer first immerges.

1.7 Surface Melting and Surface Thickness

It has been shown both experimentally and numerically that the molecules or atoms near free surface have mobility higher than the bulk and, as a result, free surface has lower melting point than their bulk counterpart – a phenomena known as "surface melting". Melting temperatures (T_m) of thin films with very small thickness or nanoparticles with very small diameter are lower than bulk materials of same chemical composition because overall thin film or nanoparticle is influenced by their surface with higher mobility. The same phenomenon is observed for amorphous materials where glass transition temperature (T_g) of structures with low dimensions are lower than bulk material of same kind. Melting temperature or glass transition temperature of thin films and nanoparticles is size dependent – lower the thickness or diameter, lower the melting or glass transition temperature. The higher mobility near surface and lower melting or glass transition temperature results many interesting properties of nanostructures. The Figure 1.4 below shows the change in melting temperature with changing the size of Ni nanoparticles.
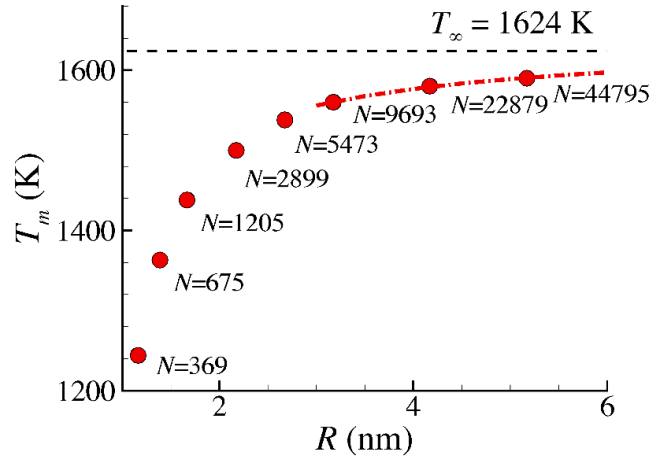
Figure 1.4: Melting temperature of Ni NP with changing radius of Ni NP. [29]

Similarly, glass transition temperature of $Cu_{64}Zr_{36}$ metallic glass thin films and nanoparticles are shown in the Figure 1.5.
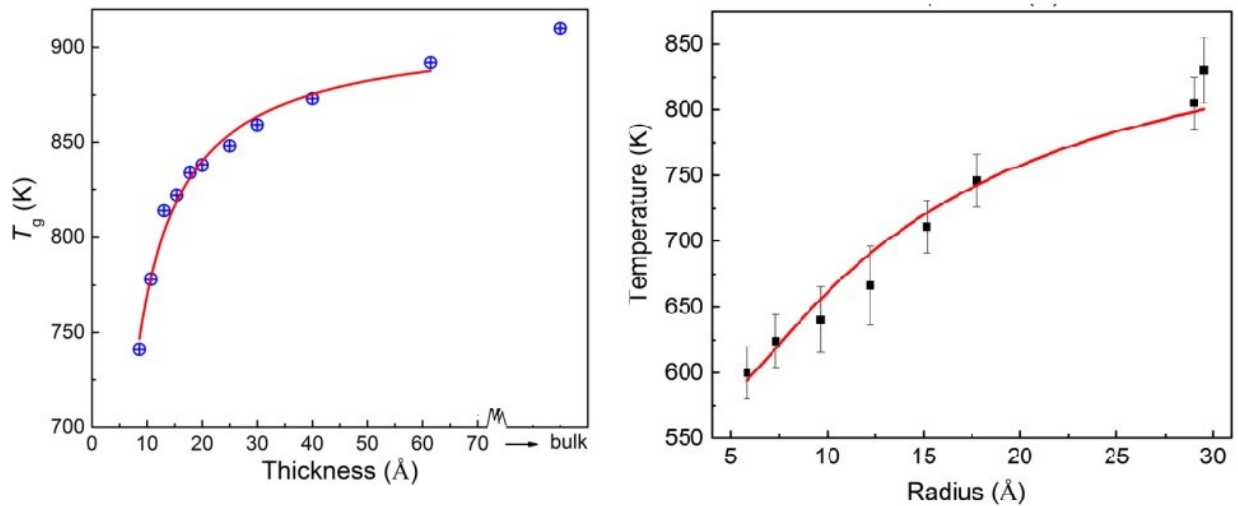
Figure 1.5: Glass transition temperature of $Cu_{64}Zr_{36}$ metallic glass thin films as function of film thickness and glass transition temperature of $Cu_{64}Zr_{36}$ metallic glass nanoparticles as function of radius. [30]

Higher mobility of atoms or molecules near free surface is not a monolayer, rather the thickness of the layer with higher mobility can be several angstroms. We measure the thickness of surface with higher mobility from the point where the mobility is 5% higher than the bulk or interior mobility to the free surface. The details of finding mobile surface layer thickness are discussed later.

1.8 Glass Transition and Tammann Temperature

Tammann temperature (T_{TA}) is the temperature where surface melting starts, which is normally (1/2 to 2/3) of melting temperature. Besides testing localization model, we also focused on Tammann temperature. We can determine Tammann temperature from the intersecting point of the linear parts of Debey-Waller factor plots of surface atoms and core atoms. For amorphous materials, we get glass transition temperature by following the same procedure. Figure 1.6 below shows the glass temperature determination of Ni nanoparticle.
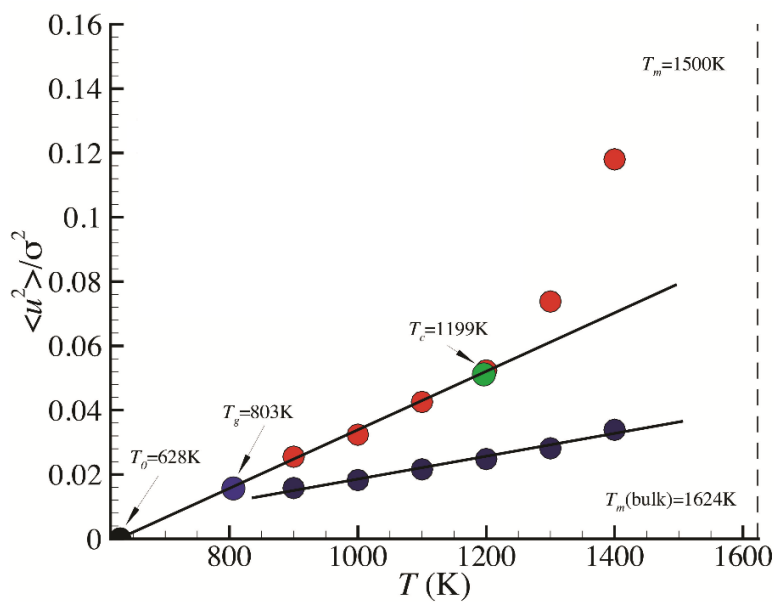
Figure 1.6: Glass transition temperature of Ni NP. Red dots represent normalized DWF of interfacial part and dark blue dots represents normalized DWF of the core. Extrapolated fits of interface and interior of normalized DWF coincide near Tammann Temperature. [29]

A list of Tammann temperatures of different materials as we as their melting temperatures are listed below. [31]

Compound	Melting Temperature, T_m (K)	Tammann Temperature, T_{TA} (K)
Pt	2028	1014
PtO	823	412
PtO_2	723	362
$PtCl_2$	854	427
$PtCl_4$	643	322
Pd	1828	914
PdO	1023	512
Rh	2258	1129

Rh$_2$O$_3$	1373	687
Ru	2723	1362
Fe	1808	904
Co	1753	877
Ni	1725	863
NiO	2228	1114
NiCl$_2$	1281	641
Ni(CO)$_4$	254	127
NiS	1249	625
Ag	1233	617
Au	1336	668
Cu	1356	678
CuO	1599	800
Cu$_2$O	1508	754
CuCl$_2$	893	447
Cu$_2$Cl$_2$	703	352
Mo	2883	1442
MoO$_3$	1068	534
MoS$_2$	1458	729
Zn	693	347
ZnO	2248	1124
SiO$_2$ (Quartz)	1883	942

1.9 Objective of this study

The goals of this computational study are –

1. We will test localization model for free standing $Cu_{64}Zr_{36}$ metallic glass (MG) thin films (TF) with different thicknesses ranging from 10Å to 60Å to confirm if it can predict slow dynamics α-relaxation time (τ_α) and diffusivity (D) from fast dynamics Debye-Waller Factor (DWF). We are more interested in interfacial dynamics of $Cu_{64}Zr_{36}$ MG TF, and therefore, we will test localization model for overall (whole) MG TF, interfacial region of MG TF where particles have enhanced mobility, and core (inside), if there is any, of MG TF which has dynamics similar to bulk metallic glass (BMG).

2. Interfacial dynamics of crystalline metals are similar to the dynamics of glass-forming materials because of highly anharmonic interparticle interactions. Therefore, in addition to metallic glass thin films, we will also test the same model for interfacial region of 60Å crystalline Cu thin films with different crystallographic orientation; (100), (110) and (111) on free surface. We will test localization model only in the interfacial region of crystalline Cu thin films.

3. Moreover, we will verify if Tammann temperature can be determined from the intersection of extrapolated profiles of DWF of core or bulk and interface profiles for both $Cu_{64}Zr_{36}$ metallic glass thin films and crystalline Cu thin films.

4. We will continue testing localization model for nanostructure with different geometry. After testing this model for flat interface of thin films, we will test the same for $Cu_{64}Zr_{36}$ metallic glass nanoparticles (MG NP) and crystalline Cu nanoparticles with different diameters ranging

from 20Å to 60Å. Similar to thin films, we are only going to study interfacial dynamics of crystalline Cu NP and both interface as well as the overall of $Cu_{64}Zr_{36}$ MG NP.

5.   Estimation of Tammann temperature from DWF of interface and core (bulk) of nanoparticles (both crystalline and metallic glass) will be carried out.

6.   Nanoparticles (NP) are widely used as catalysts in industrial applications, but unfortunately, the science behind enhanced reaction speed in the presence of nanoparticles is still not clearly known. Also, nanoparticles are usually dispersed on an interactive substrate to use NPs as catalysts. So, our next goal will be understanding the interfacial dynamics of supported NPs. We will study interfacial dynamics of crystalline Cu nanoparticle supported on interacting graphene (C) substrate. We will study effects of substrate on dynamics of overall NP, free interface, and nanoparticle-substrate interface.

7.   One of the biggest challenges of studying dynamics of crystalline Cu NP supported on graphene (C) is the interaction strength between Cu atoms and C atoms. To understand the effects of graphene (C) substrate on Cu atoms of nanoparticle, we will study the dynamics with varying strengths of Cu-C interactions and compare the results with dynamics of free-standing Cu NP.

8.   We will test localization model on free surface of Cu NP (the surface of the NP exposed to the vacuum) and Cu-C interface (NP surface touching the graphene substate).

9.   Due to the interaction between Cu and C atoms, dynamics of Cu atoms will be affected. As a result, overall melting temperature and Tammann temperature of nanoparticles can be changed. We will determine melting and Tammann temperatures of free-standing crystalline Cu NP and supported crystalline Cu NP with different Cu-C interaction strengths.

Chapter 2: Methodology

2.1 Atomistic simulation

Gaining in depth knowledge about nano-scale phenomena of materials by experimental study is still too difficult even with help of state-of-art technology. Preparing proper samples, making suitable environment for experiments, and conducting experiments can be extremely difficult if not impossible. We are primarily interested in studying interfacial dynamics of free-standing thin films of very small thicknesses, free standing nanoparticles of very small diameters and supported nanoparticle on interacting substrate. Preparing samples and conducting experiment on free standing thin film or nanoparticle in perfect vacuum is utterly impossible. Moreover, experiments possible to conduct using available technology can be very expensive and time consuming. Before moving into real experiments, numerical studies are very helpful to understand nano-scale phenomena of materials.

Most accurate numerical results can be obtained from quantum mechanics calculations by solving Schrödinger's equation of a system. Using currently available computational capability, we can only perform quantum mechanics calculation of very simple system of hundreds of atoms for hundreds of picoseconds. For our current computational study, therefore, we use Molecular Dynamics (MD) atomistic simulation which simulates, using a suitable potential, motion of atoms without separately considering electrons according to Newton's law ($F = ma$). Molecular dynamics simulation allows us to simulate relatively large system of up to millions of atoms for nanosecond timescale. Furthermore, well studied potentials are available for the systems of our interest.

2.2 Molecular Dynamics (MD) Simulation

Molecular dynamics is a computer simulation that determines positions of atoms and molecules over time. First, positions and velocities of all atoms are set, and accelerations of all individual atoms are set to zero. Meaningful interatomic potentials are employed and atoms are allowed to interact for a fixed short period of time to calculate forces acting on each atom. Newton's equations of motion are numerically solved to determine the trajectories of atoms. Pressure (P) and temperature (T) are controlled using appropriate methods at this stage to determine new positions of atoms. New forces at new positions of atoms are calculated again and the process keeps repeating.

Set initial position $(r_0)_i$ and velocity $(v_0)_i$ of atom i.
Set acceleration $(a_0)_i$ equal zero.
Choose a short timestep Δt.

Calculate force $(F)_i$ acting on atoms based on potential.

Apply pressure (P), temperature (T) and boundary condition.

Determine new position $(r_t)_i$ and velocity $(v_t)_i$ after Δt.

Output for analyzing physical quantities.
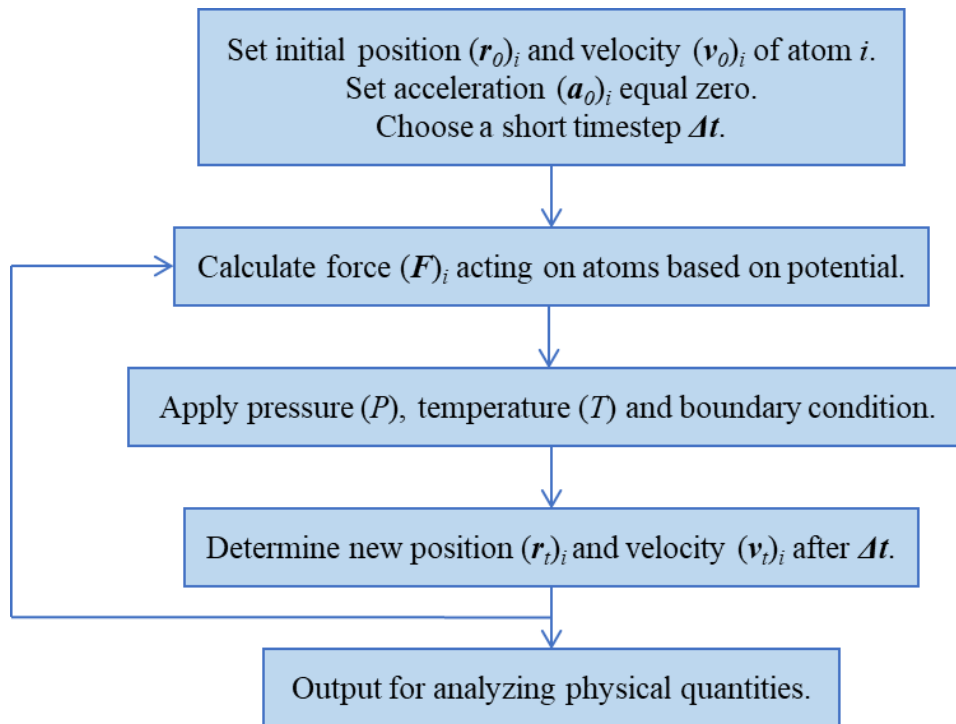
Figure 2.1: Flow chart of molecular dynamics simulation.

We ran all our simulations using Large-scale Atomic/Molecular Massively Parallel Simulator (LAMMPS), which is an open-source molecular dynamics simulation software developed in Sandia National Laboratory of USA. [32]

Advantages of molecular dynamics:

- Molecular dynamics gives positions and potential energies of atoms over time. Properties like diffusivity, strain, relaxation times, etc. can be calculated from the trajectories of atoms.

- It can be used for both equilibrium and non-equilibrium states of systems by defining appropriate initial conditions.

- Computationally less expensive than quantum method.

- Easier to use for large systems.

Disadvantages of molecular dynamics:

- Enough empirical data must be available to develop force fields to run molecular dynamics.

- Appropriate force field has to be known to get meaningful results from molecular dynamics simulations.

- MD simulation is not useful for the chemical process that doesn't follow Newton's law of motions.

2.3 Ensemble

Molecular dynamics simulation uses the concept of ensembles of statistical mechanics. In statistical thermodynamics, individual particles can be considered as system which can be

characterized by their states (position, r_i and momenta, p_i). A collection of systems is considered as an assembly and a combination of many assemblies are called ensemble. Macroscopic properties of like pressure, volume, etc. is obtained by averaging the microscopic properties of systems. Thus, macroscopic properties are ensemble average obtained from microscopic properties of systems.

Ergodicity: Ensemble average is difficult and utterly impractical to measure if the number of systems is very large ($N > 10^3$). Instead of taking ensemble average of a large number of systems, it is often easier to average long trajectory of a single system. If trajectory is long enough, we can assume that a single system goes through all possible states in phase space. Ergodicity means the long time average of a single system is equivalent to the ensemble average and if that is true for a system, the system is called ergodic system.

There are several types of ensembles depending on the fixed state variables – number of particles (N), volume (V), pressure (P), chemical potential (μ) and temperature (T).

Microcanonical (NVE) ensemble: Number of particles, volume and energy of individual assemblies are conserved in microcanonical ensembles. To keep energy conserved, the system must be isolated or closed. So, individual assemblies are separated by insulated, impermeable and rigid walls.

Canonical (NVT) ensemble: Canonical ensemble has same number of particles, constant volume and constant temperature of assemblies. Energies can be exchanged between assemblies to keep temperature of assemblies fixed. Systems are closed but heat can be exchanged from a heat bath in NVT ensemble. Individual assemblies are separated by conducting, impermeable and rigid walls.

Isothermal-isobaric (NPT) ensemble: Volume can be changed to keep pressure same in isothermal-isobaric ensemble. Temperature and number of particles are also kept same for NPT ensemble.

Grand canonical (μVT) ensemble: Systems are separated but conducting and permeable walls. Therefore, assemblies can exchange heat and particles to conserve temperature and chemical potential.

2.4 Interatomic Potential

Interatomic potential is the mathematical function that describes the potential energy of interacting atoms in given positions. We used following types of interatomic potentials in our study –

- Crystalline Cu atoms – EAM potential.

- $Cu_{64}Zr_{36}$ metallic glass – EAM potential.

- C atoms of graphene – AIREBO potential.

- C atoms of graphene and Cu atoms of Cu NP – LJ potential.

2.4.1 Pair potential

When potential energies are calculated between every two atoms of the system, the interatomic potential is called pair potential. The simplest form of pair potential is extensively studied and widely used Lennard-Jones Potential (LJ potential or 12-6 potential) [33–35]. In Lennard-Jones potential, attractive and repulsive forces of two atoms are calculated where atoms are

considered to be soft sphere and electronically neutral. Lennard-Jones potential is described by the following relation,

$$V_{LJ}(r) = 4\varepsilon \left[\left(\frac{\sigma}{r}\right)^{12} - \left(\frac{\sigma}{r}\right)^{6} \right] \qquad (2.1)$$

Figure 2.2 describes the basics of Lennard-Jones potential, where attractive and repulsive forces are shown by green and blue lines respectively. The resultant potential energy is shown by red curve. The repulsive part of the LJ potential is $4\varepsilon \left(\frac{\sigma}{r}\right)^{12}$ and the attractive part of the LJ potential is $-4\varepsilon \left(\frac{\sigma}{r}\right)^{6}$. The attractive part of LJ potential describes the long-range dispersion force.
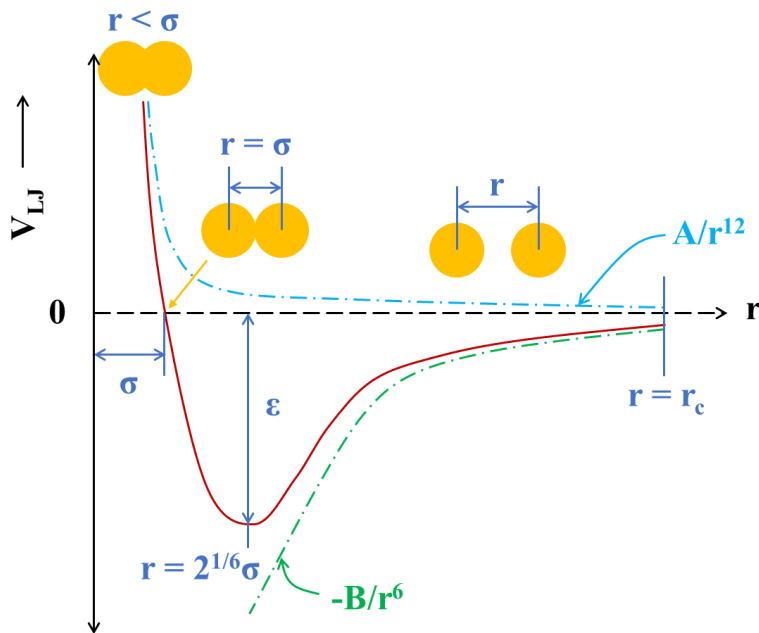
Figure 2.2: Potential energy against distance of between two atoms according to Lennard-Jones potential.

On the other hand, the repulsion part is based on Pauli exclusion principle and as a result, energy increases abruptly when electron cloud of two atoms start to overlap. At equilibrium

distance ($r = 2^{1/6}\sigma$) between two atoms, the potential is ε which is the lowest value of the potential. Resultant potential is zero at when two atoms are $r = \sigma$ apart. Atoms strongly repel each other when the distance between them is less than ε. We ignore potential energy if the distance between two atoms is greater than the cut-off distance, r_c. The force acting on atom can be obtained from the gradient of LJ potential;

$$F = -\nabla V_{LJ} \tag{2.2}$$

2.4.2 EAM potential

LJ potential is good for noble gases and very simple interactions between atoms, but not suitable for pure metals and metal alloys because metal atoms have inner cores and delocalized valence electrons. One of the most efficient potential metals is Embedded atom method or Embedded atom model (EAM) potential where atoms are considered to be immersed or embedded in the electron clouds and all atoms have an embedding energy [36,37]. In EAM potential, we consider interaction between two atoms as well as the interaction of an atom with its surrounding electron cloud. So,

$$E_{EAM} = \frac{1}{2}\sum_{i,j} \varphi_{ij}(r_{ij}) + \sum_{i} F_i(\rho_i) \tag{2.3}$$

$$\text{where, } \rho_i = \sum_{j\neq i} \rho(r_{ij}) \tag{2.4}$$

The first part of above equation is energy due to pair-wise interactions and second part is embedding energy, which is a function of electron density. There are three functions in to solve to get EAM potential – (1) Pair-potential function $\varphi(r)$, (2) Electron density function, $\rho(r)$ and (3) Embedding energy function $F(\rho)$.

2.4.3 AIREBO Potential

Adaptive Intermolecular Reactive Empirical Bond Order (AIREBO) potential is developed for carbon and hydrogen atoms, which computes energy by adding pair-wise potentials taking the sum of LJ-potential, Reactive Empirical Bond Order (REBO) interactions of covalent bonding, and torsion interactions. [38] AIREBO potential function is shown below –

$$E_{AIREBO} = \frac{1}{2} \sum_i \sum_{j \neq i} \left[E_{ij}^{REBO} + E_{ij}^{LJ} + \sum_{k \neq i,j} \sum_{l \neq i,j,k} E_{kijl}^{TORSION} \right]$$

(2.5)

The REBO part of the equation describe the C-C, C-H and H-H interactions in the short range, $r < 2$Å and LJ potential part describes the interactions in the long range, 3Å $< r < r_c$. The torsion part of AIREBO potential describes dihedral angle preferences in hydrocarbon.

2.5 Boundary Condition

In the present study, we are only using periodic boundary condition to all three dimensions for all simulations. So, we are not discussing about any non-periodic boundary conditions here. When we apply periodic boundary condition in all three directions, particles of a single simulation box will be interacting with particles of surrounded 26 exact same simulation boxes. An atom of one simulation cell can interact with all atoms close to it regardless which simulation cell they are located in. In the Figure 2.3, we see a representative simulation cells setup in two-dimensional diagram. The red atom in the middle simulation cell is interacting with three green atoms where only one atom is located in the same simulation cell but two other atoms are in neighboring cells. One of the very important things to keep in mind that the simulation box size has to be large enough

to make sure that no atom is interacting with itself. Suppose that the simulation cell is so small that the red atom of any neighboring cell falls within the dashed red circle. In that case, one red atom is interacting with another red atom of another cell, which means red atom is interacting with itself. In periodic boundary condition, atom can cross one side of the boundary and enter from the opposite side of the boundary. We need keep this fact in mind during analyzing data to get any dynamic properties like DWF, mean square displacement, etc.
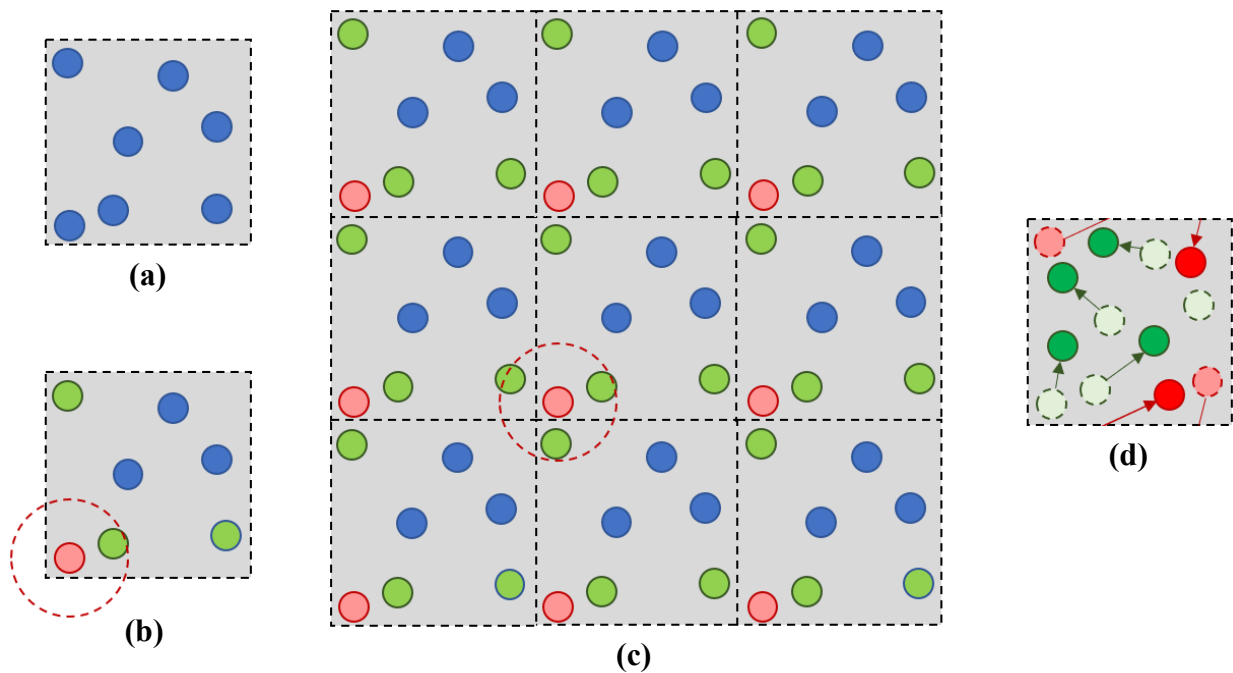
Figure 2.3: Periodic boundary condition. (a) Schematic 2D diagram of one simulation cell with periodic boundary conditions. (b) The red atom can interact with atoms located within the dashed red circle. Three green atoms are interacting with the red atom. (c) One simulation cell is surrounded by 26 exact same cells. 2D representative schematic diameter of one simulation surrounded by other simulation cells. Red atom in the middle simulation cell is interacting 3 green atoms located within the dashed red circle. (d) A simulation cell with periodic boundary condition where positions of six atoms are shown in two timesteps. Circles with dashed border and light fill color represent initial positions and circles with solid borders and darker fill color represent final positions of atoms. Two red atoms crossed the boundary; left from one side and entered from other side of the simulation cell.

2.6 Verlet Algorithm

To solve the equation of motions, the most commonly used algorithm is Velocity Verlet algorithm. First, Verlet algorithm is discussed here [39]. Suppose that $r_i(t)$ and $v_i(t)$ represent position and velocity of particle at time t. $(t + \Delta t)$ and $(t - \Delta t)$ are two time after and before time t, separated by very small increment of time, Δt. Positions at time $(t + \Delta t)$ and $(t - \Delta t)$ are $r_i(t + \Delta t)$ and $r_i(t - \Delta t)$ respectively. By Taylor series expansion and ignoring higher order terms, we get,

$$r_i(t + \Delta t) = r_i(t) + v_i(t)(\Delta t) + \frac{1}{2!}a_i(t)(\Delta t)^2 \tag{2.6}$$

$$r_i(t - \Delta t) = r_i(t) - v_i(t)(\Delta t) + \frac{1}{2!}a_i(t)(\Delta t)^2 \tag{2.7}$$

Subtraction of these two equations give us,

$$v_i(t)(\Delta t) = \frac{r_i(t + \Delta t) - r_i(t - \Delta t)}{2(\Delta t)} \tag{2.8}$$

Adding those two equations, we get,

$$r_i(t + \Delta t) = 2r_i(t) + a_i(t)(\Delta t)^2 - r_i(t - \Delta t) \tag{2.9}$$

Two equations above are Verlet algorithm. We need to know positions of particles before and after small increment of time to use Verlet algorithm, which is the main disadvantage of this algorithm. To avoid this issue, we can use velocity-Verlet algorithm, where the first equation will be the same but acceleration is written in terms of force and the velocity is also defined by the force.

$$r_i(t + \Delta t) = r_i(t) + v_i(t)(\Delta t) + \frac{1}{2m}F_i(t)(\Delta t)^2 \tag{2.10}$$

$$v_i(t + \Delta t) = v_i(t) + \frac{\Delta t}{2}\left(\frac{F_i(t) + F_i(t + \Delta t)}{m}\right) \tag{2.11}$$

2.7 Temperature and Pressure Control

Standard molecular dynamics simulation is microcanonical (NVE) ensemble where total energy is conserved. However, energy changes during numerical integration because of rounding and ignoring higher order terms. Consequently, pressure and temperature change over time. But it is necessary to keep pressure and temperature constant for meaningful simulation. There are several useful methods to keep temperature of simulation fixed. In this study, we utilized the Nosé-Hoover thermostat method where it is assumed that the system is coupled with a heat reservoir [40,41]. The system can exchange heat with connected thermostat or heat bath and, hence, the combined energy of system and reservoir stays constant even though energy of the system fluctuates.

The Hamiltonian of a system is the summation of kinetic and potential energies of all particles as shown below.

$$H = \sum_i \frac{p_i^2}{2m} + U(r^N) \tag{2.12}$$

Nosé-Hoover thermostat method introduces a new degree of freedom, s, that represent the heat reservoir. It also introduces a friction force, $\zeta(t)$ and the mass of imaginary heat reservoir is Q. $\zeta(t) = d(\ln s)/dt$ and $d\zeta(t)/dt = 0$ at steady-state. The modified Hamiltonian of the system combined with reservoir is –

$$H = \sum_i \frac{\boldsymbol{p}_i^2}{2m} + U(r^N) + \frac{Q}{2}\zeta^2 + 3Nk_BT \ln s \qquad (2.13)$$

According to this modified Hamiltonian, equations of motion have to be modified.

Similar to temperature control, pressure control of simulation is also important to run a meaningful simulation. Therefore, pressure can be controlled by changing the volume. Parrinello-Rahman barostat is based on NPT ensemble, where both volume and shape are allowed to change to maintain constant pressure [42].

2.8 Cu$_{64}$Zr$_{36}$ Metallic Glass and Crystalline Cu thin films

We start with testing LM at the free interfacial region of free-standing (FS) Cu$_{64}$Zr$_{36}$ Metallic Glass (MG) thin films (TF) with different thicknesses as well as overall metallic glass thin films (MGTF) [7]. The static properties including coordination number, interface and core compositions, potential energy distribution, etc. and some dynamic properties including mean square displacement of Cu$_{64}$Zr$_{36}$ Metallic Glass thin films with different thicknesses, where the conclusion was the properties of thin film affected significantly by its thickness [30]. Thickness and composition effects on mechanical properties of metallic glass thin films have also reported before [43–45]. Significant Cu segregation near surface has been also reported in the study mentioned above [30], which implies that the composition, also properties as a result, on free interface can significantly differ from the bulk part of glass forming alloys. Especially, core and free interface compositions can be largely different for MG thin films and this difference becomes more prominent with decreasing the thickness of the MG films. For example, if we cut a thin film with significantly low thickness from bulk Cu$_{64}$Zr$_{36}$ metallic glass (BMG), the surface Cu content will be more than 64%

and core or inside Cu content will be less than 64%. As an obvious outcome, properties of surface and core will be different. Moreover, the thickness of this affected interfacial region varies with composition and temperature, about which we will discuss later in this report. Therefore, the whole MG thin films with very small thickness can act like interface. Interfacial dynamics of crystalline metal thin films have been computationally studied a lot so far, however, further study on the interfacial dynamics on metallic glass thin films is needed [30,46–48]. Taking all these facts into consideration, we decided to study interfacial dynamics of free standing $Cu_{64}Zr_{36}$ metallic glass thin films of different thicknesses ranging from 10Å to 60Å and in addition, dynamics of the inside or core of MG and overall MG thin films and compare the dynamics of interface, core, overall MG thin films.

Along with $Cu_{64}Zr_{36}$ MG thin films, we tested LM for interfaces of Cu thin films because free interfacial regions of crystalline metals exhibit many significant properties similar to glass-forming liquids [49–52]. Needless to say, understanding interfacial dynamics of metallic materials as well as metallic glass alloys are important for many technological and industrial applications [46,53–58]. Interfacial dynamics of crystalline metallic thin films greatly influenced by their crystallographic orientation of the free surface [49,59–61] and hence, we choose three different crystallographic orientation as the free surface of crystallographic Cu thin films with almost same thickness (~60Å) – (100), (110) and (111).
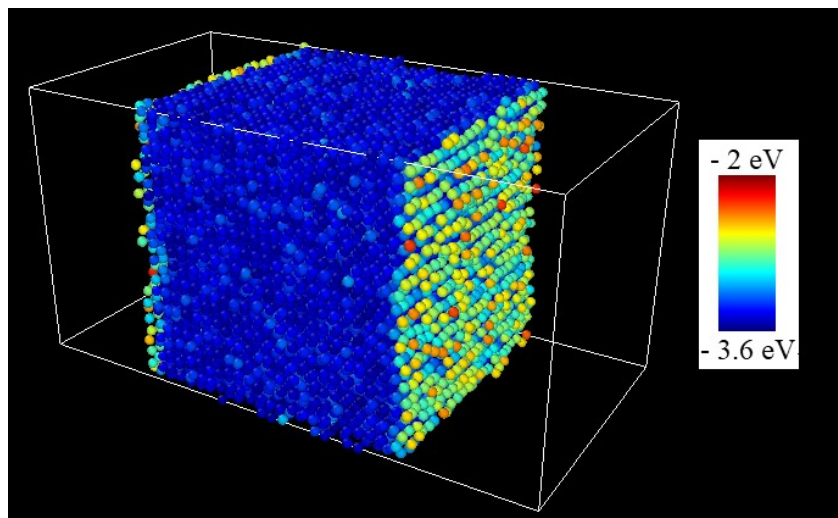
Figure 2.4: Free-standing crystalline Cu thin film with 60Å thickness and (110) crystallographic orientation of free surface at 1000K. The color bar represents the potential energy of Cu atoms at a snapshot.

2.9 $Cu_{64}Zr_{36}$ Metallic Glass and Crystalline Cu Nanoparticles

Nanoparticles are drawing attention of researchers for last few decades due to their many interesting properties. Along with much higher surface to volume ratio compared to bulk materials, anharmonic interaction and higher mobility near interface of nanoparticles results their wide range of scientific and technological application including, but not limited to, catalytic processes, electronics, drugs and medications, nanotechnology, and energy harvesting. Nanoparticles exhibits interesting and different characteristics like its tendency to coalesce, ability to migrate on surface and fluctuating shapes at temperature below melting temperature. Understanding interfacial dynamics of nanoparticles is hence important to understand for scientific research and development. Despite putting lots of efforts to understand interfacial dynamics of nanoparticles, further studies are needed to gain in depth knowledge on this topic, especially for metallic glass

nanoparticles [29,51,52,62]. Therefore, as a continuation of our study on interfacial dynamics of metallic glass and crystalline metallic thin films, we conduct the same study of LM description for free standing $Cu_{64}Zr_{36}$ metallic glass nanoparticles and crystalline Cu nanoparticles of different dimeters ranging from 20Å to 60Å. After conducting test of the localization model description and study interfacial dynamics on flat surface of thin films, we conduct the same study on nanostructure with different geometry, i.e., the curved surface of nanoparticles with different curvatures. Because of its curved surface, unlike free-standing Cu thin films, there is no fixed crystallographic orientation of free surface of free-standing crystalline Cu nanoparticle.
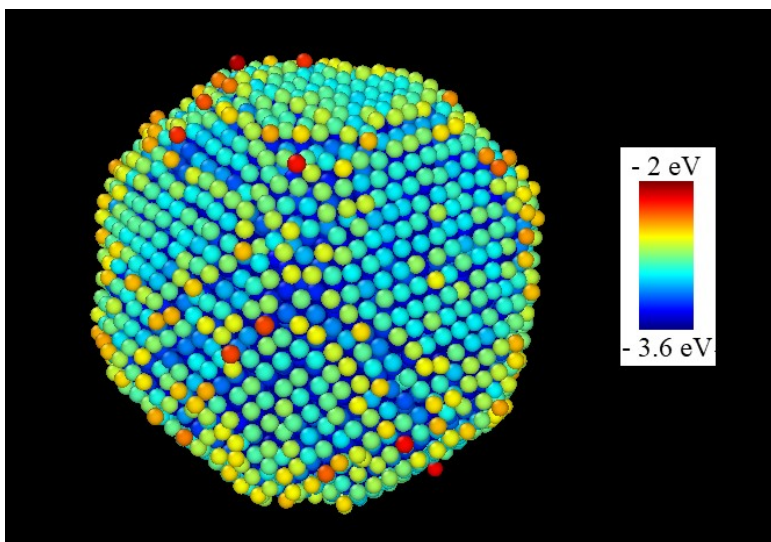
Figure 2.5: Free-standing crystalline Cu nanoparticle with 60Å diameter 1000K. The color bar represents the potential energy of Cu atoms at a snapshot.

2.10 Cu Nanoparticles on interacting supporting substrate

Nanoparticles are dispersed on solid substrates to use them as catalysts because substrate optimize chemical reactivity and prevent nanoparticles from coalesce. In addition to the size of

nanoparticles, substrate also influence the stability and catalytic reactivity of nanoparticles. To understand underlying physics of nanoparticles as catalysts, it is important to know how nanoparticles interact with the solid substrate and how interfacial dynamics of nanoparticles are influenced by the interactive supporting substrate. As a further continuation of testing localization model description, we intended to test the model on the free surface of nanoparticles and the area where nanoparticle and its solid supporting substrate meet. Consequently, we started with a Cu nanoparticle with 10000 atoms and free-standing diameter roughly 64Å and placed that on a graphene (C) substrate. We varied the interaction strength between Cu atoms of nanoparticle and C atoms of graphene substrate and compared the results with a free-standing Cu nanoparticle of same number of atoms. Note that, with increasing interaction between Cu and C atoms, the shape of nanoparticle keeps changing from nearly perfect sphere to a near hemisphere. In addition to the core or interior and free surface of the nanoparticle, we also study the dynamics of the Cu-C interface where Cu atoms are directly influenced by the interaction with C atoms of the substrate.
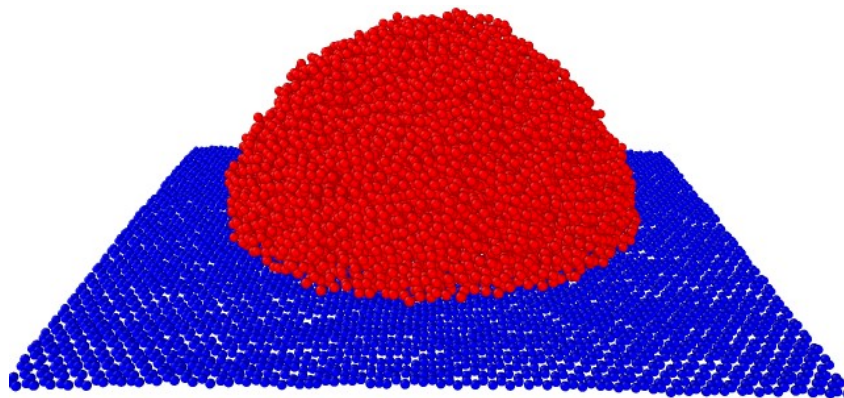
Figure 2.6: Crystalline Cu NP on the interactive supportive graphene (C) substrate at 1250K. The Cu nanoparticle shown above had a diameter of 60Å at 300K.

2.11 Different regions of FS TF, FS NP and supported NP

Please note that, by the both words "*surface*" and "*interface*" in **chapter 3 and 4**, we refer the parts of thin films and nanoparticles which are exposed to the vacuum. The green parts, denoted by "*S*", of free-standing thin film and free-standing nanoparticle shown in the schematic diagram in Figure 2.7 is the surface or interface, which means these parts are exposed to the vacuum.

On the other hand, for Nanoparticle on graphene in **chapter 5**, we only use the word "*surface*" to refer free surface exposed to the vacuum and "*Cu-C interface*" refers to the Cu atoms near the substrate. Free surface exposed to the vacuum is shown in green in the Figure 2.7 which is denoted by "*S*" and Cu-C interface, shown in yellow in the Figure 2.7, is denoted by "*Cu-C-int*" of "*int*".
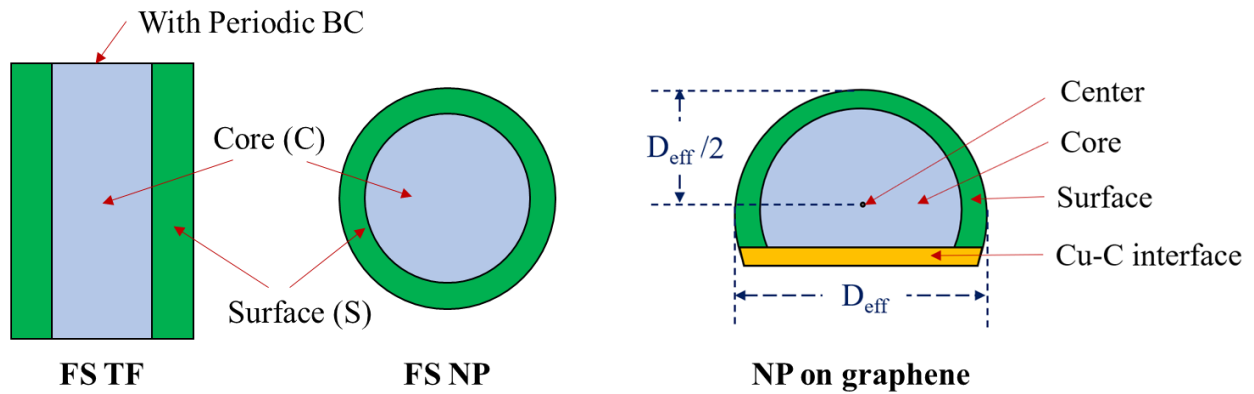
Figure 2.7 Different regions of free-standing thin films and nanoparticles, and nanoparticle supported on substrate.

Chapter 3: Localization model description of the interfacial dynamics of crystalline Cu and Cu$_{64}$Zr$_{36}$ metallic glass films

Recent studies of structural relaxation in Cu–Zr metallic glass materials having a range of compositions and over a wide range of temperatures and in crystalline UO$_2$ under superionic conditions have indicated that the localization model (LM) can predict the structural relaxation time τ_α of these materials from the intermediate scattering function without any free parameters from the particle mean square displacement $\langle r^2 \rangle$ at a caging time on the order of ps, i.e., the "Debye–Waller factor" (DWF). In the present work, we test whether this remarkable relation between the "fast" picosecond dynamics and the rate of structural relaxation $\tau\alpha$ in these model amorphous and crystalline materials can be extended to the prediction of the local interfacial dynamics of model amorphous and crystalline films. Specifically, we simulate the freestanding amorphous Cu$_{64}$Zr$_{36}$ and crystalline Cu films and find that the LM provides an excellent parameter-free prediction for $\tau\alpha$ of the interfacial region. We also show that the Tammann temperature, defining the initial formation of a mobile interfacial layer, can be estimated precisely for both crystalline and glass-forming solid materials from the condition that the DWFs of the interfacial region and the material interior coincide.

3.1 Introduction

There has long been interest in the mean square atomic displacement $\langle r^2 \rangle$ in crystals relative to the average interparticle distance in relation to the phenomenological Lindemann criterion of melting, defined by this ratio achieving a critical value at which the crystal becomes unstable [1,63–

[68]. More recently, however, it has become appreciated that $\langle r^2 \rangle$ at a characteristic caging time t_{cage} on the order of a ps $[\langle r^2(t_{cage}) \rangle \equiv \langle u^2 \rangle]$ also has significance in relation to understanding the rate of diffusion and structural relaxation time τ_α in both model glass-forming metallic ($Cu_{64}Zr_{36}$) and polymeric materials, [4,18,26] as well as inorganic crystalline (crystalline UO_2) materials [9]. In particular, simulation observations have confirmed the localization model (LM) prediction [8,9] that τ_α for both these materials can be quantitatively described without free parameters over a broad temperature range by the remarkably simple relation.

$$\tau_\alpha(T) = \tau_\alpha(T_A)exp\big[\{\langle u^2(T_A) \rangle / \langle u^2(T) \rangle\}^{3/2} - 1\big] \tag{3.1}$$

where $\langle u^2 \rangle$ is the Debye–Waller factor (DWF) and T_A is the onset temperature for caged particle dynamics, below which τ_α also tends to show a non-Arrhenius T dependence. [8,18,25,28]

The history and ideas behind the LM have been reviewed by Douglas et al. [8] in the context of its quantitative application to Cu–Zr metallic glasses having a range of compositions and, here, we only sketch some essential features of this model. In brief, the LM emphasizes $\langle u^2 \rangle^{3/2}$ as a dynamical measure of free volume that accounts for the effect of thermal energy (inertial dynamics) on the volume accessible to particles in a "cage" defined dynamically through multiple collisions with surrounding particles, and this measure of the extent of particle localization in the fluid is also understood at the same time to describe the emergent rigidity of the material accompanying progressive particle localization upon cooling [18]. This dynamical free volume interpretation of $\langle u^2 \rangle^{3/2}$ was originally investigated computationally by Starr et al., [24] where its geometrical "rattle free volume" interpretation was confirmed and where the LM expression between $\tau_\alpha(T)$ and $\langle u^2 \rangle^{3/2}$ was first recognized as providing a potentially quantitative description of $\tau_\alpha(T)$ in the case of a coarse grained polymer melt. Although this was the first simulation study of the relation between $\tau_\alpha(T)$ and $\langle u^2 \rangle$, there had been earlier experimental and modeling studies

suggesting a relation of this kind might exist (see Ref. [8] for a discussion of earlier contributions to the LM that provided an important context for its later development). In later work, Simmons et al.[25] provided a heuristic rationalization of the LM, and it was realized in the work of Betancourt et al.10 that the free parameters that limited the predictive nature of the original version of the LM could be completely eliminated by using T_A as a reference temperature, this reference condition being natural because T_A defines the T at which the cage first appears so that $\langle u^2(T_A) \rangle^{1/2}$ is the maximum cage size. The first quantitative test of the LM without any free parameters was made in the case of Cu–Zr metallic glasses [8], this case being favorable because atomic glass forming liquids do not exhibit the anisotropic caging [25] found in many molecular liquids since the atomic potentials of metallic atoms are spherically symmetric. This favorable situation also applies to the case of superionic crystalline UO_2,[9] and the successful application of the LM to this system without free parameters is notable because the LM had never been applied before to a crystalline material, albeit a crystal exhibiting highly anharmonic interparticle interactions as in the case of cooled liquids. Recently, Hung et al. [69] have investigated the LM in comparison to 51 glass-forming liquids including polymeric, small molecule organic, and metallic glass-forming materials, where the exponent 3 in Eq. (3.1) was taken to an adjustable parameter, based on arguments relating this exponent to anisotropy in $\langle u^2 \rangle$ in earlier work,[25] and in this survey article, the LM was found to consistently perform rather well. Further tests of the LM for different types of glass-forming liquids are ongoing (see the Conclusion).

As with all existing models of the dynamics of glass-forming liquids, and crystalline materials for T approaching their melting temperature T_m from below, the LM is based on assumptions that cannot be rigorously justified and the interest in this model derives from its general philosophical perspective of relating a measure of particle localization that can be readily

determined from measurement over a wide T range to the material structural relaxation time and from the apparent empirical success of this interrelationship. The rather dramatic success of the LM for the cases considered so far, and the similar in spirit relation between $\tau_\alpha(T)$ and $\langle u^2 \rangle$ developed by Ottochian and Leporini [26] to describe relaxation in a diverse range of materials, suggests to us that we should look for a more fundamental basis of the LM, and we discuss our admittedly speculative ideas on this subject in the Conclusion.

The application of the LM to predict the diffusion coefficients requires a relation between D and τ_α. In the case of crystalline UO_2, the diffusion coefficient D_O of the O atoms can be simply described to a good approximation by an inverse scaling relation, $D_O/k_B T \sim 1/\tau_\alpha$, [9] consistent with the Stokes–Einstein relation. In contrast, in glass-forming liquids, atomic and molecular diffusion coefficients normally obey a "fractional Stokes–Einstein" (FSE) relation [19],

$$D/T \sim (\tau_\alpha)^{1-\zeta} \tag{3.2}$$

where ζ is a "decoupling exponent" quantifying the degree of deviation from the Stokes–Einstein relation [9]. For the superionic UO_2 material, it was found that $\zeta \approx 0$ to within numerical uncertainty, which is a material notably free of dynamical heterogeneities involving particles exhibiting locally preferred packing, as found in metallic glass and other glass-forming materials. This finding accords to the hydrodynamic "obstruction model," [19] which attributes the decoupling phenomenon to the presence of finite clusters of immobile particles that persist to times long enough for steady state diffusion to become established. In particular, the momentum diffusion coefficient (viscosity) and mass diffusion coefficient of the solvent molecules are altered differently by the presence of heterogeneities, as in the hydrodynamics of particle suspensions and other heterogeneous fluids [28].

The extraordinary thing about Eq. (3.1) is that it implies a predictive link between the dynamics of the material on a nearly inertial dynamics timescale generally on the order of ps ("fast" dynamics) and the alpha relaxation time, which involves a timescale on the order of a minute near the glass transition temperature, T_g. It is also remarkable that the LM prediction involves no free parameters. A relation similar to Eq. (3.1), but with the exponent 3 replaced by a slightly altered phenomenological value, was also found to describe relaxation data in polymeric fluids [18]. This alteration of the LM is natural in polymer liquids since $\langle u^2 \rangle$ is defined in terms of the motion of generally asymmetric chain segments rather than spherically symmetric atoms, making localization of the segments by surrounding segments occur in a likewise anisotropic fashion. Simmons et al. heuristically introduced a model that attributed this variable exponent in the LM to variations in the particle shape in complex fluids such as polymers [25]. Here, we confine our attention, as in our previous studies of metallic glass [8] and UO_2 materials [9], to materials composed of atomic metal and inorganic ionic species, respectively, where the complication of anisotropic particle shape does not arise so that we may confidently fix the LM exponent to equal 3. From Eqs. (3.1) and (3.2), we may deduce a localization model prediction for the translational diffusion coefficient,

$$ln[\{D(T)/T\}/\{D(T_A)/T_A\}] = (1 - \zeta)\left[\{\langle u^2(T_A)\rangle/\langle u^2(T)\rangle\}^{3/2} - 1\right] \qquad (3.3)$$

introduced by us in a previous paper investigating Cu–Zr metallic glasses [8]. Given the previous surprising success of the LM in both bulk model crystalline and non-crystalline materials, the present work explores whether the LM can be extended to describe the gradient in mobility and relaxation times over a wide range of T near the free interface or surface of both model metallic glass ($Cu_{64}Zr_{36}$) films and crystalline Cu films. Previous preliminary work found that the gradient of the mobility near the free interface of supported glass-forming polymer could be qualitatively

understood from an extension of Eq. (3.1) from the bulk to interfacial region of polymer nanoparticles in a polymer matrix [70]. Becchi et al.[71] first examined whether a quantitative relation exists between τ_α and $\langle u^2 \rangle$ on a layer by-layer basis for substrate-supported unentangled glass-forming polymer films. They found a good reduction in the relaxation time as a function of depth $\tau_\alpha(z)$ in terms of $\langle u^2 \rangle$, except near the immediate vicinity of the solid substrate when the polymer–substrate interaction is highly attractive. More recent work by Zhang et al. [72] has shown that this near substrate region for polymer films on substrates having highly attractive interactions has a tendency to become trapped in a non-equilibrium state so that the difficulties in relating τ_α and $\langle u^2 \rangle$ in this part of the film are understandable [72]. We take these results to be encouraging regarding the applicability of the LM to describe the interfacial dynamics of both $Cu_{64}Zr_{36}$ metallic glass films and crystalline Cu films. Notably, our study below will be limited to "free-standing" films to avoid the issue of non-equilibrium effects that can arise near highly attractive solid substrates.

Our simulations for model glass-forming and crystalline materials indicate that Eqs. (3.1) and (3.3) quantitatively describe the gradient in the interfacial relaxation time and average atomic mobility, respectively, to an excellent approximation for all T investigated so that the LM is again confirmed for this extended class of materials. A novel aspect of our work is that the interfacial mobility gradients in crystalline and metallic glass materials are treated in a unified fashion. No previous studies examining the relationship between τ_α and $\langle u^2 \rangle$ in the interfacial dynamics of crystalline materials have been made before, although there have been numerous simulation and experimental studies of $\langle u^2 \rangle$ of crystalline metals [59,60,73] and the diffusion coefficient D of atomic species in the interfacial layer of crystalline films [49,74–76]. Below, we focus on crystalline Cu and we acknowledge previous studies that have focused on $\langle u^2 \rangle$ [77,78] and the interfacial D for Cu [75,79,80]. We also show below that the onset temperature for the formation of an interfacial layer of enhanced

mobility, the Tammann temperature, can be estimated in a unified way for both crystalline and glass-forming materials.

Apart from its academic interest, the interfacial dynamics of metallic materials is crucial for understanding many basic technological physical processes related to catalysis, tribology, corrosion, etching, fracture mechanics, welding, thin film growth, etc. [46,53] Interfacial dynamics is also of fundamental interest in small molecule and polymer solid materials in the context of a host of applications [54,55]. Apart from the usual applications described in these works, we mention observations of extremely large interfacial mobilities in connection with the development of new materials for fuel cell, battery, and sensor applications; [56,57] the cold joining of metallic glass materials by enhancing interfacial mobility with ultrasound; [58] and the exploitation of the high interfacial mobility in the casting of highly stable glassy films by vapor deposition [81]. This is the tip of the application iceberg so to speak, and we mention these examples to help bring further potential applications of an enhanced understanding of interfacial mobility of crystalline and glass materials into view.

Just as the glass transition temperature T_g has numerous engineering applications for amorphous materials as indicating a condition at which appreciable molecular mobility first emerges upon heating glass materials, the Tammann temperature T_{TA} demarks the onset of appreciable molecular mobility and reactivity [82,83] in crystalline materials, and this characteristic temperature likewise has many numerous practical engineering applications in the thermal stability of explosives [84] and fine chemicals (e.g., pharmaceuticals, agrochemicals, dyes and pigments, fragrances, flavors, and diverse other specialty chemicals), [85] the reactivity and design of heterogeneous catalysts such as those used in catalytic converters, [86] the synthesis of nanotubes with metal nanoparticle catalysts, [87] and the stabilization of nanoparticles against sintering [31,88] and

powder sintering, [89] which is currently of great relevance to the emerging fields of additive manufacturing and 3D printing of metallic and polymer materials, respectively. T_{TA} also has fundamental geophysical significance. In particular, the presence of a mobile interfacial layer on ice has a profound on atmospheric chemistry occurring on the surfaces of ice nanoparticles in the atmosphere and in the dynamics of glaciers because of the polycrystalline nature of these materials [90]. We note that T_{TA} often follows the same approximation to the melting temperature $T_{TA} \approx (1/2 - 2/3) T_m$, depending on the class of material. [83] A similar correlation is observed for T_g of materials that crystallize, $T_g \approx (1/2 - 2/3) T_g$, [91,92] suggesting that these characteristic temperatures might be somehow related. We could go on at length about the importance of interfacial dynamics and the specific importance of T_{TA} on the properties of crystalline materials and on many specific industrial and biological processes contingent on enhanced interfacial dynamics near the boundaries of these materials. The practical scope of better understanding interfacial dynamics from a unified perspective is thus vast. We next turn to our task of investigating the interfacial dynamics of model glass-forming and crystalline materials.

Given the vast number of applications of crystalline and glass films, there have correspondingly been quite numerous simulation and measurement studies aimed at elucidating the interfacial dynamics of this broad class of materials. In the present work, we specialize our study to metallic films because the mean square atomic displacement of the atoms in these materials can be precisely determined and compared to the localization model (LM), which relates this quantity to the structural relaxation time. We also study thin crystalline and metallic films of varying orientations since film thickness has been observed to influence the strength, plasticity, ductility, and stability of this class of materials. [43–45,49,93–104] While there are quite numerous computational studies of the interfacial dynamics of metallic crystalline materials, there are

relatively few studies of the interfacial dynamics of metallic glass materials. [30,46–48] Our work is somewhat novel in that we compare the dynamics of crystalline and amorphous glass-forming films with a view toward obtaining a unified description of their dynamics. In particular, we start with testing the LM for $Cu_{64}Zr_{36}$ metallic glass thin films and crystalline Cu thin films having different orientations. Previous work has shown that the interfacial dynamics on interfaces of different crystallographic orientations can be greatly different, [49,59–61] so we investigate the (100), (110), and (111) free surface orientations of crystalline Cu films. The (110) surface is the most loose-packed of these surface layers and has the highest and dynamical interfacial activity, while the (111) surface is close-packed and has a relatively slow interfacial dynamics in the crystal state. [80]

3.2 Simulation methodology

Molecular dynamics (MD) simulation has been employed in the current test of the LM for $Cu_{64}Zr_{36}$ metallic glass thin films and the interfacial layer of crystalline copper thin films with different surface orientations. Our MD simulations employed the large-scale atomic/molecular massively parallel simulator (LAMMPS), developed in Sandia National Laboratories, [32] and a Mendelev form of embedded atom model (EAM) potential was used in interatomic interaction for both copper–zirconium alloy and crystalline copper. [105] Previous studies confirmed that this EAM potential provides good descriptions of equilibrium or static as well as dynamic properties of Cu–Zr alloys. [14,105,106] All simulation time steps were 1 fs, and the periodic boundary condition was applied in all three dimensions in this study. The pressure is controlled by the Parrinello–Rahman algorithm, [42] temperature is maintained by the Nose–Hoover thermostat method, and time

integration is performed on Nose–Hoover style non-Hamiltonian equations of motion during the simulation. [40,41]

3.2.1 Cu$_{64}$Zr$_{36}$ metallic glass films (MGFs)

We begin with a perfect copper FCC single crystal with an approximate simulation box size in X, Y, and Z directions of $6.4 \times 6.4 \times 6.4$ nm^3, respectively. Randomly selected 36% of the total 13600 copper atoms were replaced by zirconium atoms. First, this mixture was heated to 1500 K, which is well above the melting temperature of Cu$_{64}$Zr$_{36}$. The system was then kept at 1500 K and zero pressure using an isothermal–isobaric (NPT) ensemble for 2 ns to make sure that the mixture is homogeneous. Thin films of thicknesses of 60Å, 50Å, 40Å, 30Å, 20Å, 15Å, and 10Å were then cut from the bulk box, and two 30Å thick vacuum layers were added on both sides of the thin films.

In order to obtain equilibrium metallic glass film (MGF) structures, all systems are relaxed at 1500 K in the canonical ensemble (NVT) for 1 ns. There was significant Cu segregation on MGF surfaces as reported before. [43] After isothermal relaxation at 1500 K, MGF systems were quenched down to 300 K with 1×10^{12} K/s cooling rate. Restart files have been saved at every 25 K temperature decrement in order to study further isothermal relaxation. Isothermal relaxations have been carried out at every 50 K temperature reduction between 1500 K and 900 K in the NVT ensemble. Systems are relaxed for at least 4 ns and maximum of 30 ns at a given temperature.

3.2.2 Crystalline Cu films

Simulation cells with $\approx$6.4 nm length in all three directions were created using LAMMPS so that the X axis is perpendicular to the desired surface (100), (110), and (111) planes. The systems are then relaxed for 1 ns at 300 K in the NPT ensemble. After relaxation, two 30 Å vacuum layers are added on both sides along the X axis. Thus, all of the crystalline Cu films are $\approx$64 Å thick. All systems are again relaxed for 1 ns after adding vacuum layers followed by heating from 300 K to 1500 K in an NPT ensemble. Restart files are saved at every 10 K temperature increment for further isothermal relaxation. Isothermal relaxation of the crystalline Cu thin films has been carried out near melting temperature for at least 8 ns and up to 20 ns. Below, $Cu_{64}Zr_{36}$ metallic glass films with a thickness of 60 Å are referred to as MGF60A, crystalline copper films with (110) surface configurations will be referred to as Cu110F, etc. MGF60A-O, MGF60A-S, and MGF60A-C are, respectively, overall, two interfacial regions and the core or interior part of the MGF60A material.

3.3 Results and Discussions

3.3.1 Diffusivity (D) and Debye–Waller factor (DWF) $\langle u^2 \rangle$

Diffusion coefficient estimates are obtained in a standard fashion from the slope of the mean square displacement (MSD) after long times (t). More specifically, diffusivity is defined by the equation $D = \langle \frac{1}{N} \sum_{n=1}^{N} \{(x_i - x_0)^2 + (y_i - y_0)^2 + (z_i - z_0)^2\}\rangle / 6t$, where ($x_0$, y_0, z_0) and (x_i, y_i, z_i) are the particle's initial and final positions after time t, respectively, and N is the number of

atoms. The particle motion is nearly ballistic for a very short period that is typically less than 100 fs. After this transient inertial dynamics regime, particles become caged for a timescale defining the structural relaxation time, after which particle motion can be described as being diffusive. The average square displacement $\langle r^2 \rangle$ of particles after a characteristic caging time t0 is known as the Debye–Waller factor, $\langle u^2 \rangle$. In metallic glasses, the DWF is the displacement of any atom caged by its surrounding atoms. Following previous work, [8] we define the DWF by the condition $\langle u^2 \rangle = \langle u^2(\tau_\beta) \rangle$, where the "caging time," or more specifically the "fast beta relaxation time" τ_β [107] describing the initial decay of the intermediate scattering function, is taken to equal $\tau_\beta \approx 2$ ps.

Our investigation of the interfacial mobility gradient in thin metallic glass and crystalline films is complicated by the anisotropy in $\langle u^2 \rangle$ in the directions parallel and perpendicular to the interface of the film, and this anisotropy is mirrored by the anisotropy in the segmental relaxation time, τ_α. The anisotropy in $\langle u^2 \rangle$ has been studied for many years, starting from idealized lattice dynamics calculations assuming perfectly harmonic interatomic interactions [108,109] to perturbative and effective medium model and molecular dynamics simulation based optimized embedded atom potentials accounting for anharmonic interatomic interaction effects, which are prevalent above T_{TA}. [59–61,77,78,110,111] Notably, the significant importance of anharmonic interatomic interactions at crystalline metal surfaces was first made in a pioneering study by MacRae and Germer, [112] and this scientific topic has remained highly active until the present day. We show some representative results for in-plane and normal-to plane estimates of $\langle u^2 \rangle$ for the (110) surface of Cu in Figure S5 of the Appendix A (supplementary material) where the out-of-plane component is significantly larger than the in-plane component of $\langle u^2 \rangle$, an observation that has been noted in earlier studies of the (110) surface of crystalline Cu. However, this result is not general, and it has been established that the in-plane component is larger than the out-of-plane components of $\langle u^2 \rangle$ for the (001) surface

of Cu, [113–115] while the in plane and normal-to-plane components of $\langle u^2 \rangle$ for the same

crystallographic Ni are nearly the same in crystalline Ni. [116] The anisotropy in $\langle u^2 \rangle$ is evidently

highly dependent on the chemistry and the surface type. This source of variability of $\langle u^2 \rangle$ and

overall molecular mobility with crystallographic orientation and chemistry is probably a

consequence of residual stresses acting at the surfaces, the surface stress being positive for the

(110) surface and negative for the (001) surface, which vary strongly with the surface. [117] Bi is an

interesting element as the interfacial dynamics on all of the crystallographic surface is largely

equivalent. [118] We illustrate the magnitude of these residual stresses in the supplementary material

in the case of the corresponding crystallographic surfaces of Ni, which is a metal of rather similar

nature to Cu. The electronic degrees of freedom can influence these surface stresses, and in some

cases, they can become large enough to cause reconstruction of the crystal surface to a packing

geometry incompatible with the symmetry of the crystal interior. [119,120] Embedded atom potentials

are imperfect in emulating the many-body interactions associated with the electronic degrees of

freedom, so we may expect the variability of the interfacial dynamics to vary with the

intermolecular potentials used to model even nominally the same atomic or molecular species.

Similar effects can apparently be operative in the interfacial region of relatively heavy metals such

as Au and Pt and other liquids (e.g., alkanes [121]) where the interfacial region can pre-order into a

state that resembles the interfacial dynamics of a heated crystal, [122] a phenomenon that can be

expected to greatly influence crystal nucleation upon cooling as the mobile interfacial layer in

crystalline materials normally serves to enhance melting by heterogeneous nucleation. Finally, we

mention that anisotropic intermolecular interactions in polymer and other molecular liquids

naturally lead to local anisotropies in $\langle u^2 \rangle$ in both the bulk liquid and crystalline states, and this

anisotropy can be expected to be also a feature in the interfacial dynamics of this broad class of

materials. Again, we are reminded of Pauli's quip about surfaces—"God made the bulk; surfaces were invented by the devil." [123]

In the current study, we only consider $\langle u^2 \rangle$ averaged over all directions in relation to the correspondingly averaged relaxation time, τ_α. This choice is motivated by the fact that measurement cannot resolve this anisotropy in $\langle u^2 \rangle$ and τ_α as a function of depth. The inherently thin nature of the interfacial zone, its thickness being normally less than a couple of nm as we shall see below, means that the material is quasi-two dimensional from the standpoint of large range diffusion. (The component of D normal to the film direction cannot even be generally defined because the film is too thin for asymptotic diffusion to establish itself.) On the other hand, the film has a finite T-dependent thickness so that interfacial zone is strictly not two dimensional either. Accordingly, since diffusion occurs as a three-dimensional atomic displacement process, and diffusion coefficient only strictly exists in the thermodynamic limit in higher than two-dimensions, we define D using the standard three-dimensional expression for this quantity. In addition to our comparison of average $\tau_\alpha(z)$ and $D(z)$ on a layer-by-layer basis in the metallic glass and crystalline films, we also consider $\tau_\alpha(z)$ and $D(z)$ averaged over the entire interfacial layer since these averaged quantities are normally measured.

We note that while D in the direction normal to the substrate cannot be unambiguously defined for the interfacial region, it is possible to quantify the rate at which atoms transition between atomic layers in this region, providing a measure of "transverse mobility." This analysis has been performed before for the (110) interfacial region of crystalline Cu for T greater than T_{TA} by Papageorgiou and Evangelakis[31] and indicates that the activation energy for transitions between the layers varies strongly with depth from the surface where the activation entropy varies in a proportionate way to the activation energy. In our previous work, we found that this same type

of "entropy–enthalpy compensation" (EEC) relation also describes D in the interfacial regions corresponding to the different crystallographic surfaces in the case of Ni. [49] EEC has the effect of greatly increasing the prefactor in the Arrhenius relation for the interlayer transport, making interlayer transport much more probable than one would expect from the high activation energy for the interlayer transition events. In recent detailed calculations of strain-assisted surface-nucleated dislocation formation in crystalline metallic materials by Ryu et al., it was found that the prefactor can be altered by a stress induced change in the activation entropy effects by a factor as large as 20 orders of magnitude, [124,125] and even larger changes in the prefactor have been observed in D of metal alloys [126] (see Fig. 13 of Ref. [126] for a dramatic illustration of this effect). A full understanding of this problem from first principles is a fundamental unsolved problem in the physics of condensed matter having manifold practical applications, and in particular, we can expect this phenomenon to be of great significance in relation to understanding the catalysis of proteins and inorganic catalysts. [13]

Significant theoretical efforts have been made to understand this EEC effect in the interfacial dynamics of crystalline materials within the context of transition state theory, [127–129] where it was found to be associated with the highly anharmonic interatomic interactions in the interfacial layer where it was further argued to be related to the interaction of abstract collective excitations in the layer. Consistent with this physical view of the interfacial zone of crystals for T above T_{TA}, we have observed that the atomic diffusion in the interfacial layers of both crystalline Ni and TIP/4P ice is dominated by string-like atomic exchange motion involving many atoms, as observed also in simulations of glass-forming liquids. [13,130] This is a concrete manifestation of the anharmonic interatomic interactions in the interfacial layer. Evidence for the highly anharmonic nature of the interatomic interactions in the interfacial zone of crystals was discussed by Häkkinen

and Manninen, [78] Allen et al., [59–61] Dürr et al., [111] Molenbroek and Frenken, [131] and many other works, emphasizing different manifestations of this anharmonicity-nonlinear growth of $\langle u^2 \rangle$ with T, "anomalously" strong temperature dependence of the thermal expansion coefficient [116,132] and isothermal compressibility, [133] and a wide range of anomalous scattering observations from the crystal surfaces. [134] Calculations have repeatedly shown the complete inability of models that assume harmonic interactions to account for a wide range of interfacial phenomena of crystalline materials at elevated temperatures, i.e., $T > T_{TA}$. From the discussion above, it is apparent that the dynamics of the interfacial region of crystalline materials is likewise dominated by anharmonic interatomic interactions, and their dynamics is perhaps even more complicated than that of glass-forming liquids, each surface exhibiting its own distinct dynamics. In our discussion below, we seek to avoid this complexity as much as possible and focus on the enhanced interfacial mobility common to both films of crystalline and glass-forming materials.

3.3.2 Interfacial layer thickness of thin films

The highly anharmonic motions of particles in the interfacial region of both crystalline and metallic glass materials lead to the onset of mobility near the free boundary of these materials at T far below T_m and T_g. The idea of a "liquid-like" layer in the interfacial region of crystals was first introduced by Faraday, [135] based on experiments on the cohesion of ice particles in snow balls and observations on the friction of ice, and it was later appreciated that the presence of such a layer was of fundamental significance in relation to crystal melting since this layer would heterogeneously nucleate the melting of crystals. [63,136,137] Measurements and simulations indicate that this layer is "liquid-like" in the sense that the atoms or molecules have a relatively high

mobility, but at the same time, high resolution measurements and molecular dynamics simulations of the crystalline Cu, the material whose interfacial dynamics has been studied most prevalently, indicate that the atoms in the interfacial region retain a significant degree of their ordering, so the term "liquid" does not exactly fit the physical situation. [131,134,138] Although the interfacial region of crystals above T_{TA} has often been termed "quasiliquid," we think that it is physically more accurate to describe this layer as being a mobile crystalline region, similar in physical character to superionic crystalline materials—crystalline materials having liquid-like particle mobilities by virtue of the highly anharmonic interatomic interactions in these materials. [28] The formation of a mobile interfacial layer at equilibrium is also sometimes referred to as "premelting," again, suggesting the existence of some sort of "liquid-like" layer and a corresponding phase transition giving rise to such a surface state. We again emphasize that there is no evidence for such a transition in the interfacial region of crystalline Cu above T_{TA}, [131,134,138] and the high interfacial mobility in this material appears to arise simply from the anharmonic nature of interatomic interactions.

Even though the interfacial dynamics of both crystalline and glass-forming materials are similar in many ways, it should be emphasized that they have distinguishing characteristics so that it is incorrect to conclude that the interfacial layer is "equivalent" to a glass-forming liquid. [76,139] On the other hand, both crystalline and glass materials exhibit an interfacial layer of enhanced mobility whose thickness depends on T and in which there is generally a large mobility gradient transverse to the surface so that stressing this common relationship seems justified. We next consider the thickness and the mobility in these interfacial layers based on a unified treatment emphasizing the predicted LM relationship between $\langle u^2 \rangle$ and the average molecular mobility D and relaxation time τ_α.

As the first step of our analysis, we calculate $\langle u^2 \rangle$ at different thickness regions of thin films in order to determine the surface thickness where atoms have enhanced mobility. Atoms have $\langle u^2 \rangle$ values nearly equal to the bulk value in the core of thin films if the thin film thickness in not too small. The entire film behaves more like the interfacial region of the thinner films if the overall film thickness becomes less than about twice the interfacial layer thickness found for a thick film so that the interfacial layer thickness defines a characteristic film thickness below which large changes in the film dynamics occur.

Following a criterion defined in previous work, we first defined the surface region width λ by a practical cutoff criterion defined by the point at which $\langle u^2 \rangle$ deviates by 5% from its bulk-like value deep within the film and the outermost point of the film surface. [49,76] We find below that $\langle u^2 \rangle$ decreases exponentially along from the free surface to the film interior value $\langle u^2 \rangle_{core}$, as we observed in our previous studies of the crystallographic surfaces of Ni [49] and the 1120 or secondary prism face of ice. [76] This variation has also been observed in experimental studies on colloidal crystals. [140] Figure 3.1 shows $\langle u^2 \rangle$, or the "Debye–Waller Factor" (DWF), normalized by the average interatomic separation distance σ as a function of distance from the center of the free-standing film for MGF60A and Cu110F at different temperatures. We see that the disparity between $\langle u^2 \rangle$ at the surface of the crystal and $\langle u^2 \rangle_{core}$ progressively grows upon cooling, indicating increasing anharmonic interaction in the interfacial region.103 It is also qualitatively evident in Figure 3.1 that the interfacial mobility scale λ is T dependent in both the cases of metallic glass and crystalline films [76] and nanoparticles. [29,52]
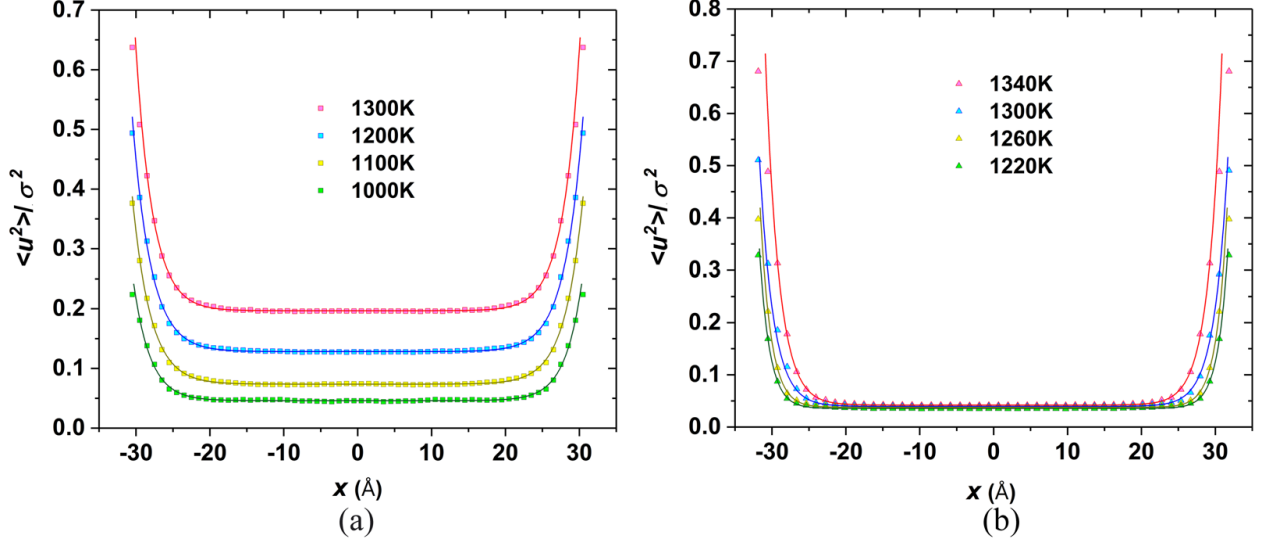
Figure 3.1: The gradient in $\langle u^2 \rangle$, normalized by σ^2, as a function of distance in Å from the center of the film in – (a) metallic glass with a thickness of ≈ 60 Å (MGF60A) and (b) the crystalline Cu film with a free interface having a (110) orientation (Cu110F) with a thickness of ≈ 64 Å at different temperatures T. All solid lines are curves fitted using Eq. (4) that provides an alternative estimate of the average interfacial width, i.e., ξ in Eq. (4). A comparison of the cutoff defined interfacial width λ and ξ is given in the supplementary material. We also illustrate the gradient in $\langle u^2 \rangle$, normalized by σ^2, as a function of distance in Å from the center of the film shown for a common temperature of 1300 K for the metallic glass with a thickness of ≈ 60 Å (MGF60A) and for crystalline Cu with a free interface having (100), (110), and (111) orientations (Cu100F, Cu110, and Cu111F) with a thickness of ≈ 64 Å in Figure S2 of the Appendix A (supplementary material).

The variation of $\langle u^2 \rangle$ as a function of distance from the film center shown in Figure 3.1 allows for the determination of the interfacial mobility scale as a function of T, based on the criterion described above. (Below, we establish a quantitative link between the atomic diffusion coefficient D and the structural relaxation time τ_α to $\langle u^2 \rangle$ that justifies our use of $\langle u^2 \rangle$ to define an interfacial mobility scale.)

Figure 3.2 (a) shows λ of "free-standing" Cu having different crystallographic orientations in comparison to λ free-standing MGFs. In order to determine the interfacial mobility scale λ, we fitted the $\langle u^2 \rangle$ curve plotted against the thickness (x) of the films to an exponential function,[26] which has the following relation:

$$\langle u^2 \rangle = \langle u^2 \rangle_{core}[1 + \delta u \, exp(-x/\xi)] \tag{3.4}$$

$$\delta u \equiv [\langle u^2(x=0) \rangle - \langle u^2 \rangle_{core}]/\langle u^2 \rangle_{core}$$

where $\langle u^2 \rangle_{core}$ is the DWF of the core, which obeys the approximation $\langle u^2 \rangle_{core} \approx \langle u^2 \rangle_{bulk}$ for the film thickness range we study. The fitting function may be inferred from a general treatment of the interfacial dynamics of crystals by Feuchtwang,[141] who found that "displacements decrease essentially exponentially with the distance from the free boundary," in accord qualitatively with molecular dynamics simulations.[59,60,108,141,142] This exponential variation of the interfacial width has been observed to describe the gradient in $\langle u^2 \rangle$ in the interfacial dynamics of colloidal crystals,[140] but this work offered no theoretical rationale for this relation. As an aside, we note that a popular phenomenological approximation [143–145] for the relaxation time τ_α gradient in glass-forming liquids can be derived from Eq. (3.4) and LM [see Eq. (3.3)] if δu in Eq. (3.4) is taken to be a small perturbative parameter, leading to the relation $ln[\tau_\alpha(x,T)/\tau_\alpha(core)] = A exp[-x/\xi_s]$, where A is a constant, and ξ_s in Eq. (3.4) formally describes the length scale of the $\langle u^2 \rangle$ and τ_α gradients. Since $\langle u^2 \rangle$ generally scales linearly with T for harmonic interactions, δu also provides a quantitative measure of anharmonicity in the interatomic interactions. We show this quantity in Figure S10 of Appendix A for MGF60A and Cu110F.
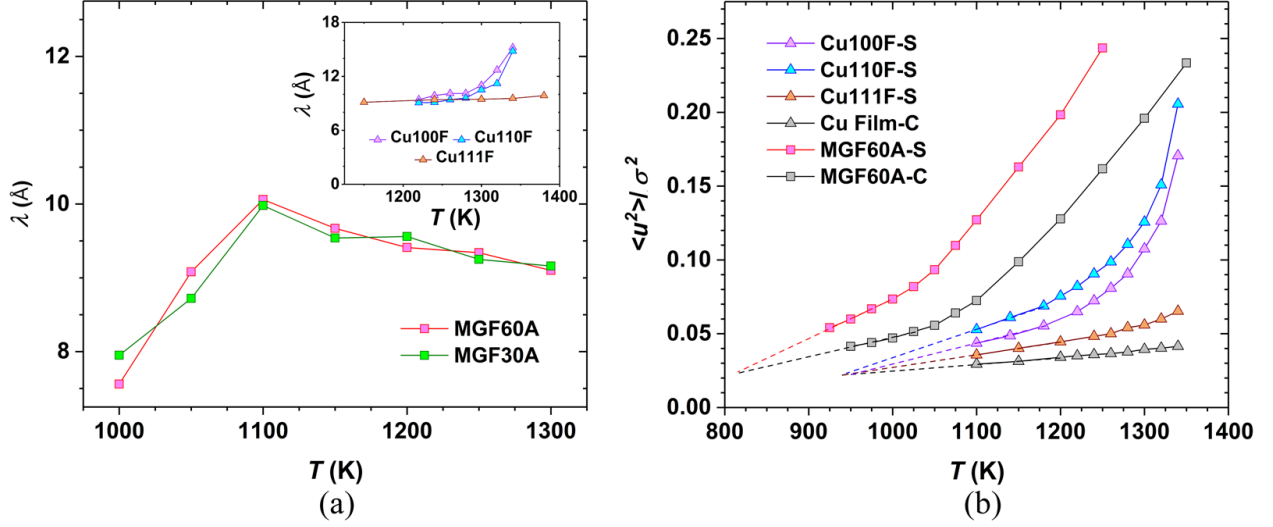
Figure 3.2: Surface thickness and Tammann temperature: (a) Interfacial mobility scale λ of metallic glass films with a thickness of $\approx 60\text{Å}$ and $\approx 30\text{Å}$ (MGF60A and MGF30A) at temperatures starting above the glass transition temperature T_g to the characteristic temperature T_A and (inset) interfacial mobility scale λ of Cu films with a thickness of $\approx 64\text{Å}$ having (100), (110), and (111) crystallographic orientations (Cu100F, Cu110F, and Cu111F) at temperatures approaching the melting temperature, T_m. (b) Estimation of the onset temperature of interfacial mobility or "Tammann temperature" in crystalline and metallic glass materials. This important characteristic temperature may be precisely estimated from the extrapolation of $\langle u^2 \rangle$ of the interfacial region and the core of the material to a low temperature at which these quantities coincide. Data points are only linearly fitted in the low temperature regime, where it shows a linear trend. The interfacial mobile region effectively ceases to exist at this intersection temperature. We find that $\langle u^2 \rangle$ of the interfacial mobile layers of crystalline Cu films having different crystallographic orientations (100), (110), and (111) all extrapolate to a common Tammann temperature near 930 K, satisfying the common phenomenology that the Tammann temperature is normally near (2/3) T_m. [83]

We find that Eq. (3.4) provides an excellent description of the gradient in the $\langle u^2 \rangle$ that we observe in both the crystalline and amorphous films, shown in Figure 3.1. The interfacial region width λ values were estimated for each type of film by $\langle u^2 \rangle$ by identifying the point at which $\langle u^2 \rangle$ deviates by 5% from its core value to the outermost surface of the films. Notably, the growth of λ

in the crystalline Cu films occurs upon heating in a fashion mirroring $\langle u^2 \rangle$, as we found before in our previous study of crystalline Ni [49,52] and ice, [76] but the T variation in the metallic glass film occurs non-monotonically over the T range studied, this interfacial scale developing a peak between T_A and T_g. This peaking of the interfacial scale accords qualitatively with a recent study of interfacial mobility scale in glass forming polymer films where a maximum in the mobility interface scale was observed, defined in this case by the structural relaxation time. [72] The present work is mainly confined to a lower temperature regime in which the metallic glass film has a "solid-like" character that is representative of real metallic glass materials.

We see in Figure 3.2(b) that the average $\langle u^2 \rangle$ in the interfacial region increases progressively with T in both the metallic glass and crystalline Cu films, but the rate of increase in $\langle u^2 \rangle$ with T in the crystalline film becomes particularly sharp when T approaches the melting temperature, T_m. In each type of film, $\langle u^2 \rangle$ is appreciably higher in the interfacial region in comparison to the film interior, a conclusion that is obvious from Figure 3.1. Figure 3.2(b) highlights the fact that the qualitative magnitude $\langle u^2 \rangle$ in the interfacial region depends significantly on crystallographic orientations of the crystalline Cu films with respect to the interface, an observation made by many previous researchers. [59–61] This sensitivity of the interfacial region for $T > T_{TA}$ in crystalline materials to the crystallographic orientation is a well-recognized phenomenon that we have discussed at length in connection with D in the interfacial dynamics of Ni.
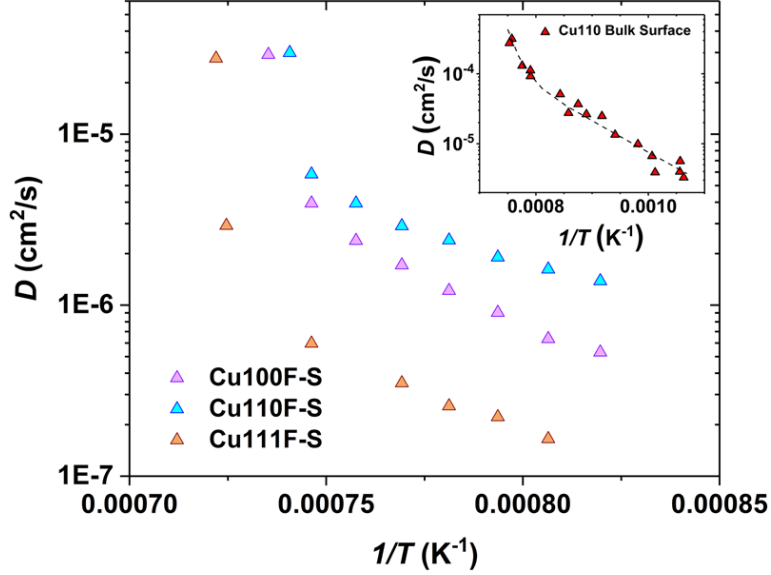
Figure 3.3: Diffusivity of crystalline Cu film: Arrhenius plot of the interfacial self-diffusion coefficients $D_{int}(T)$ vs $1/T$ crystalline Cu film for the (100), (110), and (111) crystallographic surface orientations of Cu films having a thickness of $\approx 64\text{Å}$ (Cu100F-S, Cu110F-S, and Cu111F-S) for a T range below the equilibrium melting temperature, $T_m = 1356$ K. [146] The inset shows the experimental data for surface self-diffusion for the (110) surface of Cu under an oxygen pressure of $\approx (10^{-8}$ to $10^{-6})$ Torr. These experimental data have been extracted from Bonzel's classic work (see Fig. 3 of Ref. [75]).

3.3.3 Temperature dependence of the diffusion coefficient D in crystalline and amorphous materials

For completeness, we include Arrhenius plots of the Cu atom interfacial self-diffusion coefficient D in crystalline Cu films in Figure 3.3 where we see similar trends to those reported before for the Ni atom diffusivity in different crystallographic interfacial regions of crystalline Ni. [49] As a contrast, we also consider in Figure 3.4 the interfacial self-diffusion coefficient D of our metallic glass films having thicknesses of 60Å, 50Å, and 40Å (MGF60A-S, MGF50A-S, and MGF40A-S) and the averaged D over the entire films for thicknesses of 60Å, 50Å, 40Å, 30Å,

20Å, 15Å, and 10Å. We acknowledge a previous study of the gradient of D in free-standing $Ni_{0.5}Zr_{0.5}$ metallic glass films [47] that accords qualitatively with the present study, [48] and Ref. [46] provides complementary insights into other properties of amorphous free-standing metal films through molecular dynamics simulation.
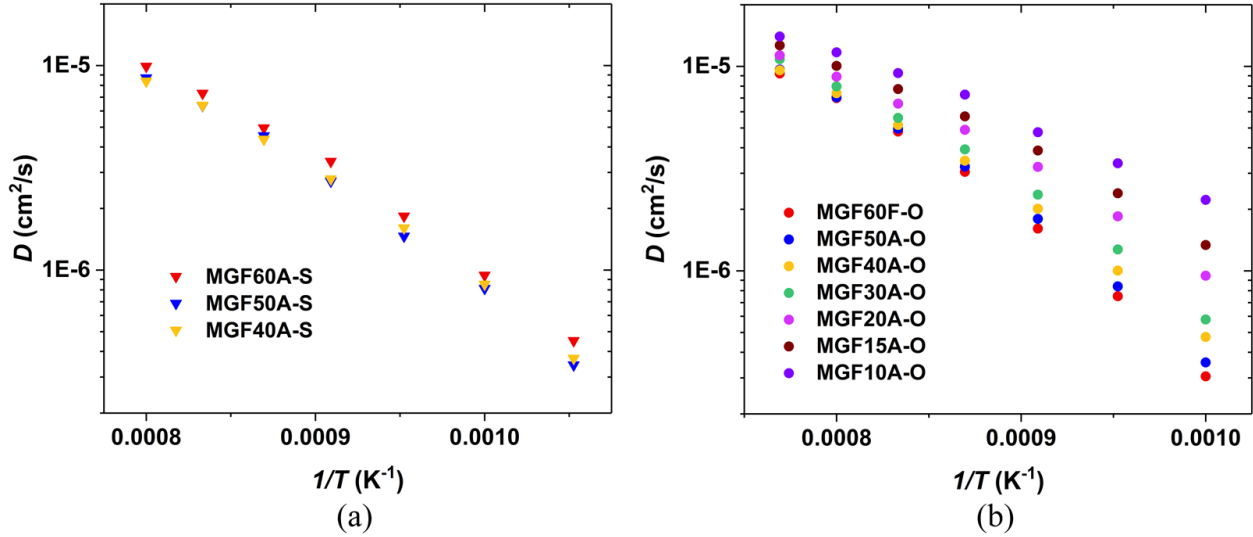
Figure 3.4: Diffusivity of $Cu_{64}Zr_{36}$ metallic glass films: Arrhenius plot of the self-diffusion coefficient D vs $1/T$ for metallic glass materials simulated in the present paper: **(a)** interfacial D for films having a range of thicknesses of 60Å, 50Å, and 40Å (MGF60A-S, MGF50A-S, and MGF40A-S) and **(b)** D averaged over the entire film for films with different thicknesses ranging from 10Å (MGF10A-O) to 60Å (MGF60A-O).

A direct comparison between the T dependence of D in the interfacial regions of crystalline and amorphous polymer films reveals a striking qualitative difference in these classes of materials, which extends more generally to observations of D in bulk crystalline and glass-forming materials. In particular, our representative examples show that Arrhenius curves for the interfacial D for crystalline materials exhibit a concave shape in which the apparent activation energy becomes higher at elevated temperatures, consistent with our previous simulation study of the interfacial

diffusivity of Ni, [49] as well as with experimental observations of D in the interfacial regions of Cu, Ni, Au, Ag, and Fe, [75,147,148] while Arrhenius curves for the interfacial D for glass-forming materials have a convex shape in which the apparent activation decreases upon heating and the prefactor in the Arrhenius relation often changes by many orders of magnitude, as observed previously in our simulations of crystalline Ni.[14] Many literature estimates of D for both crystalline and glass-forming materials, and for both interfacial and bulk D, show the same concave and convex patterns of dynamics. Even for materials such as Zr and U in their crystalline state, [149,150] they exhibit highly anharmonic dynamics that we found in UO_2 and the Arrhenius plots for these elements exhibit the same curvature as we found for UO_2.[9] Moreover, this contrary trend in the dependence of D, and the structural relaxation time τ_α, applies also to bulk crystalline [75,151] and amorphous [16,55,152] materials, with the exception of superionic crystalline materials, for which the Arrhenius curves and other aspects of the dynamics of these crystalline materials follow the pattern of relaxation found for glass-forming materials. [28]

Recently, there has been great interest [153–155] in understanding these apparently universal patterns of deviation from Arrhenius dynamics in condensed materials broadly and, in particular, the huge increases in the prefactors found in the rate of catalysis reactions mediated by enzymes [153] and crystalline nanoparticles, [156] whose dynamics follow the convex Arrhenius plot pattern of glass forming materials. Despite this contrary variation of the T dependence D in crystalline and glass-forming materials, we shall see below that that the LM provides a unified description of the interfacial D of representatives of both types of materials, just as previous simulations have shown accord with the LM for model bulk crystalline and amorphous materials. [8,9] Given the rather different interfacial dynamics normally found for crystalline and glass forming materials from an Arrhenius kinetic perspective, the application of the LM to materials from both the classes of

materials provides a rather stringent test of the general applicability of the LM to describe the interfacial dynamics of this broad class of "solid-like" materials.

3.3.4 Tammann temperature of crystalline and glass-forming materials

We should note that we are certainly not the first authors to note the existence of something like "premelting" in metallic glass forming materials. A previous MD simulation of nickel–zirconium metallic glass films having a wide range of compositions explicitly noted the occurrence of "surface melting" [46] in their materials. On the face of things, this is an odd statement if glass-formation is viewed to be a purely kinetic phenomenon, but the general idea that appreciable interfacial mobility in glasses emerges at some definite temperature seems to have merit and evident practical interest. Given that the development of interfacial mobility apparently occurs in both crystalline and amorphous materials, it would evidently be useful to quantify this mobility onset temperature precisely. We achieve this through a consideration of $\langle u^2 \rangle$ in the interfacial region in comparison to the interior of the material. In particular, we may estimate a common Tammann temperature for crystalline and glass materials by extrapolating our $\langle u^2 \rangle$ in the interfacial region and interior regions to a common low temperature at which $\langle u^2 \rangle$ for these two regions coincide. This extrapolation procedure should offer a unified method for estimating the Tammann temperature for all "solid" materials.

Before applying this procedure to our metallic glass-forming materials, however, we first test the applicability of this procedure for identifying T_{TA} in a previously well-studied model crystalline material. In Figure 3.2(b), we plot $\langle u^2 \rangle$ in the mobile interfacial regions of a crystalline film of thickness of $\approx$64 Å and having different crystallographic orientations of the crystal

boundary for generality, along with $\langle u^2 \rangle$ for the core of the crystalline. We find that all the curves

extrapolate to a common intersection temperature. In particular, these curves intersect near 930 K,

which is $\approx$ 2/3 times T_m of bulk crystalline Cu. [146] The Tammann temperature for crystalline

materials commonly follows this phenomenology, which we have discussed at length in our

previous work on the interfacial dynamics of crystalline Ni. [49] In previous studies, we also showed

that the intersection of $\langle u^2 \rangle$ for the interfacial mobile layer and the interior of the crystalline

material also occurs in Ni nanoparticles, [29] the grain boundaries of different types of crystalline

Ni, [157] and interfacial dynamics of ice [76] so that this method of estimating T_{TA} appears to have some

applicability to a wide range of materials. However, the significance of this intersection

temperature was not recognized in our former studies of the interfacial dynamics of crystalline

materials. [29,157] We remark that the onset of interfacial mobility is not signaled by any obvious

change in the static structure in the interfacial region of the crystalline material, such as density or

overall crystal structure. These changes only arise for T only a few degrees away from T_m. [158] We

emphasize that the onset of interfacial mobility in the interfacial region is a dynamical

phenomenon associated with the highly anharmonic interatomic interactions near the free

boundary, [59,60] rather than the result of any kind of surface phase transition. The dynamics in the

interfacial region of crystalline materials at equilibrium appears to be rather similar dynamically

to that of superheated [50] and superionic crystalline materials, [28] where interatomic interactions are

likewise highly anharmonic and atomic molecular mobility likewise can be very high, as in simple

liquids, despite the time averaged crystalline structure of the material.

Next, we formally extend our procedure of estimating the Tammann temperature to our

metallic glass materials. In Figure 3.2(b), we see that there is likewise a mobile interfacial layer of

enhanced $\langle u^2 \rangle$ in the metallic glass film that is rather similar in appearance to crystalline materials

and there is a separate interior region in which $\langle u^2 \rangle$ has a value comparable to that of the bulk material. [14] This is provided that the films are not so thin that separate interfacial and core regions cannot be clearly identified. In Figure 3.2(b), the film is chosen to be thick enough that separate film interior and interfacial regions exist. By extrapolating $\langle u^2 \rangle$ averaged over the interfacial region and the "core" of the film, we find that the curves intersect at a temperature near 810 K, which is comparable to (2/3) T_A, where $T_A \approx 1220$ K (while no melting temperature can be determined for our metallic glass, it has often been observed that T_A is close to T_m in systems that crystallize [159,160] so that T_A is a natural surrogate of T_m in glass-forming materials). [9] The same type of plot for MGF60A and MGF30A is given in Figure S4 of Appendix A (supplementary material) where in each case, the $\langle u^2 \rangle$ curves for the mobile interfacial region and film cores intersect near 810 K. We have also repeated the procedure just described for the other metallic glass materials and film thicknesses (MGF60A-O, MGF30A-O, MGF15A-O, MGF60A-S, and MGF60AC) and have likewise identified the T at which the interfacial and core $\langle u^2 \rangle$ curves intersect; see the supplementary material. The concept of the Tammann temperature as the onset temperature for appreciable interfacial mobility then seems to be well defined in both crystalline and glass-forming materials, and moreover, the estimation of the Tammann temperature as the point of extrapolated intersection of $\langle u^2 \rangle$ in the mobile interfacial and material interior regions provides a general means of estimating this characteristic temperature. This method of estimating the Tammann temperature should be useful in many applications in which interfacial mobility is important. [82,90]

3.3.5 Structural relaxation time, τ_α

Next, we determined τ_α from the self-intermediate scattering function (SISF) that can be obtained by performing Fourier transformation of the Van Hove correlation function. The equation $F_S(q,t) = \langle exp[-iq\{r_i(t) - r_0(t)\}]\rangle$ used for determining the SISF and F_s vs t curve is fitted using the equation $F_S(q,t) \propto exp[(t/\tau_\alpha)^{\beta_S}]$ to find τ_α. Figures 3.5(a) and 3.5(b) are self-intermediate scattering functions of, respectively, MGF60A and Cu110F-S at different temperatures. The Arrhenius and non-Arrhenius variation of the relaxation time, τ_α, in different T regimes MGF60A is illustrated in Figure S6 of the Appendix A (supplementary material). Qualitatively, there is no significant difference in the relaxation in our thin films from our previous studies of the dynamics of this metallic glass film in its bulk state, so our discussion here is brief. [8,14]
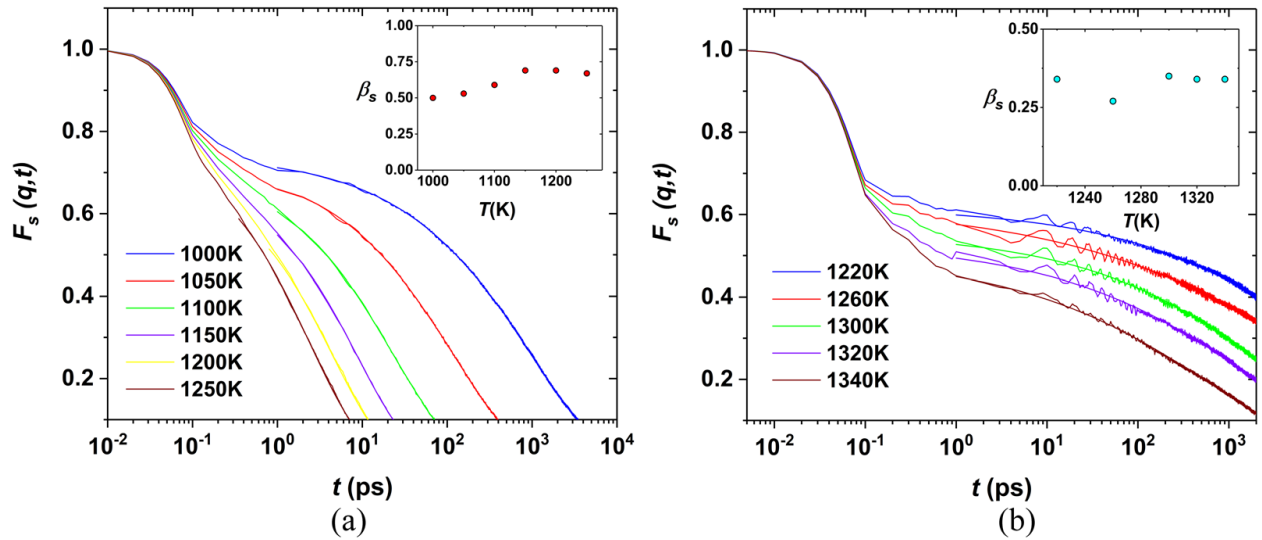
Figure 3.5: Self-intermediate scattering function of – (a) the metallic glass film with a thickness of ≈ 60Å (MGF60A-O) and (b) the interface layers of the crystalline Cu film with a thickness of ≈ 64Å having the (110) crystallographic orientation (Cu110F-S) at different temperatures. The inset of the figures shows the corresponding β_s values.

3.3.6 Localization model (LM) and decoupling exponent, ζ

Based on the LM, the α-relaxation time τ_α should follow Eq. (1) and atomic diffusivity is related to τ_α by Eq. (3). Both of the DWF $\langle u^2 \rangle$ at T_A, $\langle u^2(T_A) \rangle$, and τ_α at T_A, $\tau_\alpha(T_A)$, approach 2 ps for all metallic glass films.12 The obtained values of ζ are between 0.4 and 0.55 for all metallic glass systems, as reported previously. [14] The decoupling exponent ζ was taken to equal $\zeta_{100} = 0.58$, $\zeta_{110} = 0.64$, and $\zeta_{111} = 0.41$ for the interfaces of the crystalline Cu material (the subscripts represent the crystallographic orientation of the Cu film surface). The determination of T_A and ζ is discussed for representative cases in the supplementary material.
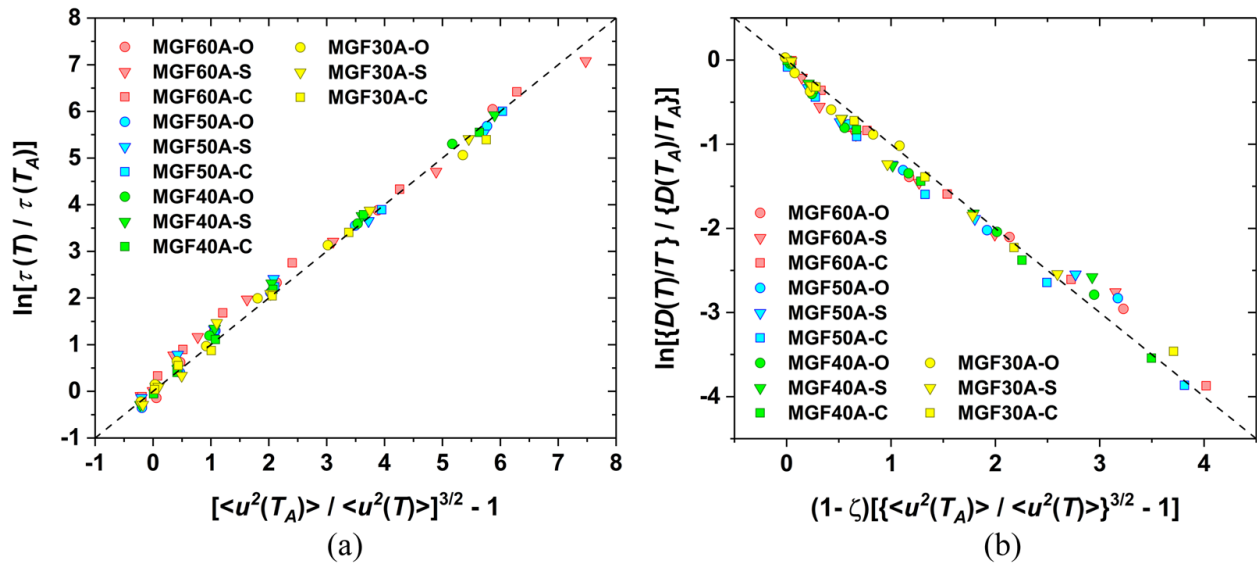
Figure 3.6: Test of localization model predictions for metallic glass films. LM prediction for the structural relaxation time τα in the film interfacial and core regions of metallic glass films and τ_α for the film as whole, designated by "O." (b) LM predictions for the diffusion coefficient D in the interfacial and core regions of metallic glass films and the average D for the film as whole.

We test the localization model (LM) predictions for D and τ_α in the interfacial and core regions of both crystalline and metallic glass films having a range of thicknesses of 60Å, 50Å, 40Å, and

30Å, as well as the overall average properties of the entire films, designated as "O." Surprisingly, the relationship between τ_α and $\langle u^2 \rangle$ for the film interfacial and interior regions and for the entire MGF material in Figure 3.6 is fit well by the LM predictions for all film thicknesses and T considered. In particular, Figures 3.6(a) and 3.6(b) show LM predictions for the interfacial and film interior regions and film properties averaged over the film for the MGF60A, MGF50A, MGF40A, and MGF30A metallic glass materials. MGFs having a thickness below 30Å do not have separate interior or "core" regions that can be clearly discriminated, and hence, we only investigated the relaxation of the entire MGF material for thicknesses below 30 Å.
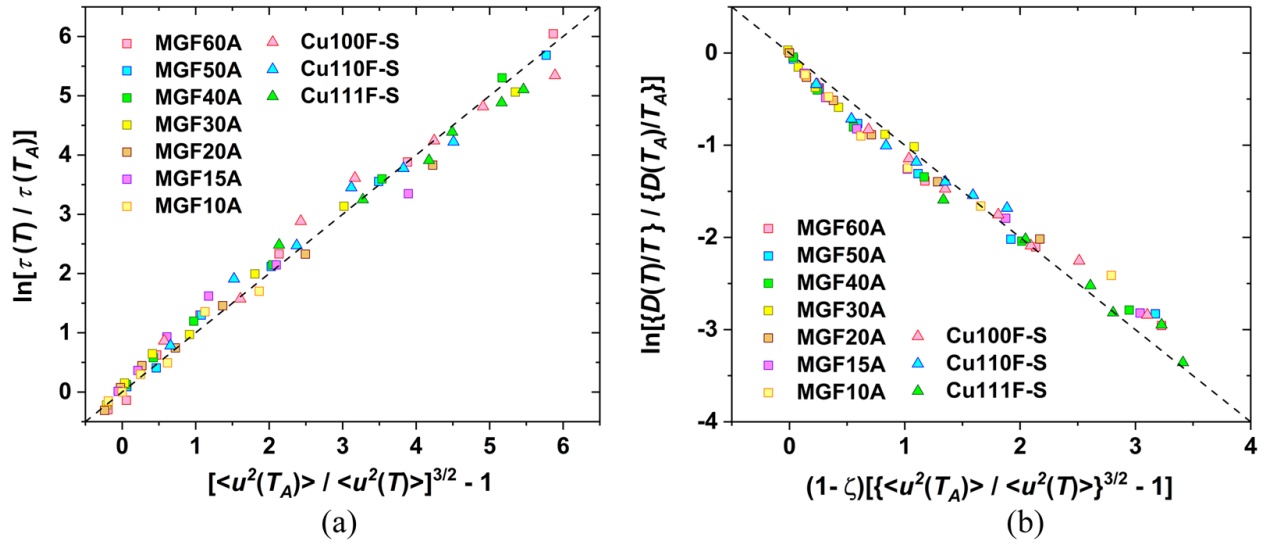
Figure 3.7: Test of localization model predictions for metal glass and crystalline Cu films having different thicknesses. (a) LM prediction for the structural relaxation time τ_α in the film interfacial and core regions of metallic glass and crystalline films having different thicknesses. (b) LM predictions for the diffusion coefficient D in the interfacial and core regions of metallic glass films and crystalline films having different thicknesses.

We next considered a comparison of D and τ_α between metallic glass and crystalline Cu films. In Figure 3.7(a), we test the LM relations for average D and τ_α for MGFs having a range of

thicknesses, and in Figure 3.7(b), we test the LM predictions for interfacial dynamics of crystalline Cu films having different crystallographic surface orientations and an overall film thickness of ≈64Å. The LM prediction seems to provide an excellent approximation of τ_α without free parameters for all cases shown in Figure 3.7(a) and D in Figure 3.7(b) where the additional information of the decoupling exponent ζ is required for each metallic glass material.

3.3.7 Discussions

As a promising working model of relaxation in condensed materials exhibiting highly anharmonic interparticle interactions, there are other important material systems that we plan to investigate based on this model because of their practical applications in areas of current technological interest. The introduction of additives to materials, by design or as a consequence of material processing methodology, can greatly alter the dynamics of the interfacial region and thus greatly alter the properties of both crystalline and glass forming materials. For example, the growth of carbon nanotubes from the surface of the commonly utilized Ni nanoparticles used in their synthesis can be greatly accelerated by adding some Au, Pt, and Pd atoms to the interfacial regions of the nanoparticles, [161,162] and crystalline Ni is known to be greatly embrittled by the segregation of sulfur to grain boundaries in this material. [163] To gain insight into these important processes, Zhang et al. investigated the interfacial dynamics of Ni nanoparticles with a variable concentration of Au, Pt, and Ag in the interfacial region for Ni nanoparticles in a size range representative of a value utilized in carbon nanotube growth and many other catalysis applications [29,51] and the interfacial dynamics of the (110) crystalline Ni [49] having a variable concentration of S in its interfacial region by molecular dynamics simulation. Zhang et al. found that these interfacial

species localize to the temperature-dependent interfacial region considered in the present paper and thereby profoundly altering the interfacial mobility, either speeding up or slowing down the interfacial mobility depending on the chemical nature of the "impurity" or its concentration in the interfacial region. This is a phenomenon of wide-ranging interest for developing materials of enhanced performance and for understanding material failure in diverse materials. In particular, we may expect the effect of interfacial additives to be of central significance to grain consolidation in connection with the rapidly developing fields of additive manufacturing and 3D printing of metallurgical and polymeric materials because of the critical importance of interfacial dynamics on particle consolidation in this broad class of materials. There are also obvious potential applications to the development of scratch resistant films; tuning the molecular permeability of films used for molecular separation processes; the development of materials of enhanced mechanical properties; and the enhanced preservation of protein drugs, food, and other biological materials, and many further applications. [164–167] With these diverse applications in view, it would be of obvious interest to investigate whether the localization model applies to the interfacial dynamics of crystalline and glass-forming materials having both metallic and polymeric compositions, with judiciously chosen additives of technological relevance, and whether this model can be used in a predictive mode to design new materials once the molecular parameters in this model are understood.

Our extensive analysis of the LM above naturally leads to the fundamental question: How can the long-time dynamics associated with structural relaxation and diffusion of so many different kinds of materials, even their local dynamics, be related to a fast dynamics material property such as $\langle u^2 \rangle$. Recall that relaxation times associated with condensed matter relaxation can be as long as minutes or even much longer for T below the glass transition temperature T_g where geological

timescales may be required to fully achieve relaxation, but $\langle u^2 \rangle$ is defined and measured on a timescale on the order of a ps, over which there is little time for diffusion or relaxation to occur. We find this type of relationship to be highly counter-intuitive, and De Michele et al. have likewise emphasized the generality and surprising nature of this type of $\tau - \langle u^2 \rangle$ relationship. [168] Notably, dynamical heterogeneity, cooperative motion, activation free energy parameters, and many other "details" describing the molecular and mesoscale properties of many condensed materials are not overtly required in the localization model relationship between τ and $\langle u^2 \rangle$. While this is a difficult question to convincingly answer based on a specific molecular model, we can suggest a possible dynamical system interpretation of this relationship that has sufficient generality to encompass our observations and that suggests new avenues for exploring the origin of this intriguing relationship between fast dynamics and long-time relaxation in diverse real materials. The coupling of the fast dynamics to the dynamics at vastly longer timescales occurs throughout the natural world, and Fujimoto and Kaneko [169] have discussed the general conditions under which this coupling occurs.

Recent studies of relaxation in model non-linear Hamiltonian dynamical systems such as the Fermi–Ulam–Pasta (FUP) β anharmonic spring model and the lattice ϕ^4 spin model in one dimension have indicated a nearly temperature independent fast relaxation process, followed by a secondary relaxation process that becomes progressively slower as the energy density ε of particles (energy per particle) in these lattices becomes reduced. [170,171] The slowing down of this second relaxation process, which is the analog of the alpha relaxation in our glass-forming materials and anharmonic crystals, is well described in these non-linear lattice models by a Nekhoroshev-like scaling relationship $\tau = \tau_o exp(\varepsilon_o/\varepsilon)^\gamma$, where γ is a system dependent constant.148 Above a critical energy density ε, or temperature because the kinetic energy of the particles grows with temperature, the relaxation time τ becomes approximately constant, $\tau = \tau_o$, corresponding to a

condition of strongly chaotic dynamics. [170,172] It has also been observed by Pettini and Landolfi, [170] and others, [173–175] that the maximum Lyapunov exponent λ_1 for these model non-linear dynamical systems scales as an apparent power law in ε in this weakly ergodic dynamics regime and that the relaxation functions in this regime exhibit a two-step decay as a function of time, the second relaxation step taking the form that can be fit by a stretched exponential function.[148] This leads us to consider an alternative form of the Nekhoroshev-like scaling relationship $\tau = \tau_o exp(\lambda_{1o}/\lambda_1)^\delta$, where δ and λ_{1o} are system dependent constants whose values we ignore for the moment. Instead, we focus on the interesting qualitative idea implied by this modified form of the Nekhoroshev relation, which is that the slowing down of the dynamics upon cooling condensed materials reflects the degree of chaoticity of the dynamical system "driving" the system to explore its complicated hierarchically structured phase space through the action of Arnold diffusion. [170,176,177] The onset condition for a temperature insensitive relaxation time at elevated temperatures corresponds to reaching a strong stochasticity threshold (SST), in which the system evolution becomes fully chaotic, defining a condition for "complex" or "correlated" dynamics upon lowering temperature below a critical value.[170] In the case of liquids at elevated temperatures, we recover the "simple" liquid regime in which the theory of Brownian motion applies. In particular, the collisions of surrounding molecules can under these conditions be described rather well by white noise fluctuations so that particle motion can be described as a simple random walk having completely uncorrelated steps. The material is thus "homogeneous" from a dynamical standpoint, and we identify this condition with $T = T_A$ in the present work. On the other hand, below the SST, the material can be expected to be "dynamically heterogeneous" in terms of the formation of chimeric coherent structures156 that exhibit enhanced high and low relative local mobility due to the development of spatial correlations in particle positions in both space and time. Such dynamic

coherent structures have been the focus of much recent research into glass-forming and other "complex" fluid and solid materials. [14,130] Evidently, all the complexity in the long-time evolution of these dynamical systems appears to be a "trickle-down" effect of the bare chaotic dynamics, a kind of "molecular predestination" enabling us to bypass a direct consideration of dynamic heterogeneity if we only want to estimate the structural relaxation time of the system.

All the material systems whose relaxation we have investigated so far on the basis of the localization model involve condensed matter, and thus strongly interacting, particle systems under conditions in which anharmonic interparticle interactions are highly prevalent, but also to conditions in which the material remains in thermal equilibrium. We observe that when the thermal energy reaches a critical value at which $\langle u^2 \rangle$ approaches $\langle u^2(T_A) \rangle$, then relaxation becomes relatively insensitive to T, [178] and moreover, the simulated properties of the fluid in this regime show little evidence of dynamic heterogeneity. For example, the Stokes–Einstein relation is recovered above T_A and exponential relaxation is often observed in this high temperature chaotic regime. Evidently, we must treat the high temperature material regime differently, but this high temperature regime is exactly the regime in which standard liquid dynamics models such as Einstein's Brownian motion model and Langevin models become applicable by virtue of the complete neglect of memory effects in the fluid dynamics. These findings broadly accord with the dynamical system interpretation of the localization model just described.

The localization model may also be rationalized based on the original Nekhoroshev-like scaling relationship $\tau = \tau_o exp(\varepsilon_o/\varepsilon)^\gamma$, which emphasizes the fundamental importance of the energy density ε on understanding the rate of relaxation in many-body dynamical systems. All recent numerical studies of the FUP and other model dynamical systems agree that ε is a fundamental state defining variable for dynamics and thermodynamics and that τ is a function of

ε. [171,174] In a thermodynamic system at equilibrium, we may expect the Maxwell–Boltzmann distribution to describe the kinetic energy distribution of the molecules so that the kinetic energy per particle should rise in proportion to thermal energy, i.e., $k_B T$. Moreover, the power-law effective repulsive potential interactions characteristic of many interacting molecules in the condensed state should lead by virtue of the virial theorem to a corresponding average potential energy that grows linearly with the pressure, [179] a measure of the material thermal energy, apart from temperature ranges near phase transitions that we exclude from our current discussion. At low temperatures, where molecules are localized in local potential minima, $\langle u^2 \rangle$ grows linearly with temperature, as in the case of crystalline materials, and this type of growth in $\langle u^2 \rangle$ remains roughly true even when the intermolecular interactions become anharmonic. It then seems reasonable to identify $\langle u^2 \rangle$ as a measure of the energy density of the material, and we again arrive at the localization model expression for τ with the power γ unspecified.

The energy density point of view of the localization model also gives insights into other phenomenological expressions for τ. For the reason just described, the growth of the energy density with increasing temperature naturally leads to an increase in the inherent structure energy due to the relation of this quantity of the average potential energy and configurational entropy S_c growing in parallel to the inherent structure energy. This motivates the modeling of relaxation time in materials by formally replacing by S_c, the basic assumption of the Adam–Gibbs model of the dynamics of glass-forming liquids, or alternatively by the average potential energy of the fluid. [180–183] Since various thermodynamic properties such as enthalpy, entropy, compressibility, [184,185] compressibility factor, [186] density, [187–190] and high frequency shear modulus [191] all depend on the energy density of the material, we can envision creating phenomenological models of structural relaxation based on observed relations between the relaxation time and these properties. This

would philosophically explain the success of such phenomenological models such as the entropy theory and free volume models of glass-formation in organizing observations of relaxation in diverse real materials as arising from a common relation of these thermodynamic properties to a central property, energy density. [182] We note finally in this connection that $\langle u^2 \rangle$ has been interpreted in a material context in terms of a dynamic measure of free volume [4,18] and its inverse may be interpreted as a measure of local material stiffness. [25,192] As discussed in the Introduction, these physical interpretations formed the basis of the original formulation of the LM.

Of course, temperature T is perhaps the most generally accessible thermodynamic parameter for materials at equilibrium, and given the nearly linear variation of the energy density with T, it is natural to consider a direct relation between relaxation time and T based on the Nekhoroshev relation. Since ergodic behavior only arises in FUP and other many-body dynamic systems beyond a critical value of the energy ε beyond which the dynamical system is non-integrable and because the energy density scales roughly linearly with temperature T, [193] it is natural to formally replace ε in Nekhoroshev's relation by reduced temperature, $\varepsilon \leftrightarrow (T - T_0)/T_0$, where T_0 corresponds to the temperature where the non-ergodic to ergodic transition occurs. We recognize that the resulting relation between τ and T is the Vogel–Fulcher Tammann (VFT) relation [22] if γ is taken to be unity. We also recognize from this formal argument that this scaling is consistent with the identification of ε with $\langle u^2 \rangle$ above since we have observed previously that $\langle u^2 \rangle$ scales with a power of $(T - T_0)/T_0$ over an appreciable T range above T_0 where the power in this relation is material dependent. [8,14,107] We may therefore get some qualitative insight into the phenomenological VFT relation for relaxation in glass-forming liquids from a dynamic systems perspective.

Above, we have argued that the Nekhoroshev relation is relevant to understanding material systems at equilibrium that are approaching an ergodic–non-ergodic transition in which the dynamics changes from "chaotic" to some sort of emergent "regular" type motion. Recently, there has been progress in understanding relaxation in materials approaching their critical point at which liquids transform into gases, a regime of strongly chaotic motion. [194] In particular, it has been shown that the relaxation time in this wide class of relatively "chaotic" materials varies inversely proportionally to the largest Lyapunov exponent, which, in turn, vanishes at the critical point. Correspondingly, the isothermal compressibility of materials diverges upon approaching their critical point so that this condition is essentially opposite to glass-forming liquids where the isothermal compressibility becomes extremely small, [195,196] the epitome of forming a "jammed" solid state. This dynamical system perspective has provided many new insights into the dynamics of near critical systems, and we hope that the same will ultimately be true for glass-forming materials and crystalline materials with highly anharmonic interactions.

We look forward to exploring the interrelation between these different dynamical and thermodynamic perspectives of the meaning of the Nekhoroshev relation and the localization model in the future. In short terms, it might also be interesting to directly test whether the localization model can quantitatively describe longtime relaxation in the Fermi–Ulam–Pasta β model or the one-dimensional ϕ^4 spin model, [197] given the success of this model to describe relaxation in model glass-forming liquids and crystalline materials.

3.4 Conclusion

A predictive relationship between mean square displacement on picosecond timescale and structural relaxation time, previously confirmed for both metallic glass and crystalline materials both computationally and experimentally, has been extended to the interfaces of model metallic crystalline and metallic glass materials. In particular, we find that the same relationship between $\langle u^2 \rangle$ and the long-time α-structural relaxation time τ_α, and τ_α and the diffusion coefficient D, holds in the interfacial region of the metallic glass and crystalline materials. Further research is needed to fully understand the relationship between τ_α and $\langle u^2 \rangle$, and the possible applicability of the localization model to the interfacial dynamics of nanoparticles having crystalline, polycrystalline, and glass-forming compositions and fiber, spherical, or other special geometries to confirm the predictive nature of the localization model to describe the relaxation time and mobility gradients in these other technologically important particle geometries.

Chapter 4: Localization model description of the interfacial dynamics of crystalline Cu and Cu$_{64}$Zr$_{36}$ metallic glass nanoparticles

Many of the special properties of nanoparticles (NPs) and nanomaterials broadly derive from the significant fraction of particles (atoms, molecules or segments of polymeric molecules) in the NP interfacial region in which the interparticle interactions are characteristically highly anharmonic in comparison to the bulk material. This leads to relatively large mean square particle displacements relative to the material interior, often resulting in a strong increase interfacial mobility and reactivity in both crystalline and glass NPs. The 'Debye–Waller factor', or the mean square particle displacement $\langle u^2 \rangle$ on a ps 'caging' timescale relative to the square of the average interparticle distance σ^2, provides an often experimentally accessible measure of the strength of this anharmonic interaction. The Localization Model (LM) of the dynamics of condensed materials relates this thermodynamic property to the structural relaxation time τ_α, determined from the intermediate scattering function, without any free parameters. Moreover, the LM allows for the prediction of the diffusion coefficient D when combined with the 'decoupling' or Fractional Stokes-Einstein relation linking τ_α to D. In the current study, we employed classical molecular dynamics simulation to investigate the structural relaxation and diffusion of model Cu$_{64}$Zr$_{36}$ metallic glass and Cu crystalline NPs with different sizes. As with previous studies validating the LM on model bulk and crystalline materials, and for the interfacial dynamics of thin crystalline and metallic glass films, we find the LM model also describes the interfacial dynamics of model crystalline metal (Cu) and metallic glass (Cu$_{64}$Zr$_{36}$) NPs to a good approximation, further confirming the generality of the model.

4.1 Introduction

It is difficult to overestimate the importance of the interfacial dynamics of nanoparticles (NPs) in science and technology. The inherently high relative mobility and the strong anharmonic interparticle interactions and associated cooperative motion in the interfacial region of NPs [29,51,52,62] and nanostructures and the interfaces of crystals [7] are implicated in a diverse range of applications and phenomena relating to basic catalysis processes such as carbon gasification, [198,199] catalytic converters [86], the growth of carbon nanotubes [87,162,200,201], etc. This phenomenon is also crucially important for the high propensity of NPs to coalesce [88,202–205], an effect highly detrimental in the context of the stability of metal NP catalysts, but highly beneficial in the creation of conducting films for flexible electronics through laser sintering and ink jet printing of the NPs to facilely create continuous films suitable for electronic devices [206–209], or other films with tailored optical properties or in the creation of new three-dimensional structures through controlled sintering, i.e., additive manufacturing, applications that we discussed in our previous work [7]. We also mention recent work that relates interfacial mobility to sliding friction in the context of ice [210]. Given the strong similarity between interfacial mobility gradient and collective motion observed in our simulations of the interfacial dynamics of ice [76] and crystalline Ni [49], we expect this type of relationship to be general and to have wide practical importance. We also mention recent studies emphasizing the importance of high interfacial mobility in interfacial crystallization, a phenomenon of great relevance to the stability of pharmaceuticals, the fabrication of ceramics and the mechanism of biomineralization [211–213].

Nanoparticles have also been observed to exhibit properties that seem rather strange for 'solid' particles. For example, NPs have been observed to change their shape at equilibrium or in

response to changes in environment even when the NPs are in their nominal 'solid' state below their melting temperature, T_m. [213–220] NPs have also been observed to spontaneously migrate on surfaces [221] through a process in which their shape fluctuations apparently play a role. We also mention the vast array of chemical reactions that occur in the mobile interfacial layers of crystalline metal nanoparticles and the wide range of geophysical phenomena that relate to the high interfacial mobility of ice particles. [76,90,222–225] Proteins and many other naturally occurring polymers can be viewed as 'organic nanoparticles' [226,227] and much of the complexity of living systems can be traced to reactive and responsive characteristics of this form of matter. It is then of obvious importance to develop a better theoretical understanding of the interfacial dynamics of NPs in order to exert a rational control on their properties for many applications, and also for appreciating the origin of the often high reactivity of NPs to develop strategies to mitigate their environmental impact when these particles are released into the environment.

The development of a theoretical framework encompassing this chemically diverse class of materials within a unified framework is evidently challenging. Recently, however, a general framework has been proposed for the dynamics of condensed materials at equilibrium broadly which has the requisite generality to approach this problem. The Localization Model (LM) [4,18,26] of the dynamics of condensed materials focuses in the mean square particle displacement $\langle u^2 \rangle$ on a well-defined timescale that is typically on the order of a ps in both molecular and atomic liquids and solids—the 'Debye–Waller factor' (DWF). It provides a measure of the strength of the inherent anharmonicity of the interparticle dynamics and the LM relates this quantity without free parameters to the structural relaxation time $\tau\alpha$, which can be as long as minutes at the glass transition of glass-forming liquids. Note that $\tau\alpha$ at glass transition temperature T_g is on the order of 10^{15} times larger than the timescale on which the DWF is determined. This model also allows

for the prediction of diffusion coefficients, provided that the 'decoupling' or 'Fractional Stokes-Einstein relation' (FSE) relating D and τα is specified. In previous works, we have validated this model on Cu-Zr metallic glasses having a wide range of compositions [8], superionic crystalline UO_2 [9] and quite recently tested the capacity of the LM to describe the interfacial dynamics of thin crystalline (Cu) and metallic glass (Cu-Zr) films [7] and the LM model in each case was confirmed to a good degree of approximation. A variant of the LM was also confirmed earlier for bulk, polymer film and polymer nanocomposite materials. [18] A recent simulation study of extended simple point charge model (SPC/E) water showed that LM could be employed to describe the structural relaxation time of water with characteristic temperature TA taken in this work as an adjustable parameter [228]. The present work is another contribution seeking to determine the limitations of the LM. In particular, we consider the applicability of the LM to describe the interfacial dynamics of crystalline (Cu) and metallic glass (Cu-Zr) metallic glass NPs, where our analysis closely follows our former analysis of thin metallic crystalline and metallic materials of the same chemical composition. In short, the LM again performs very well in predicting the relation between $\langle u^2 \rangle$ and τ_α without free parameters in all the NP systems investigated and we were also able to estimate D through a system dependent decoupling relation. In our previous work, [7] we give a heuristic interpretation of the apparently very general LM relation connecting the fast (inertial) dynamics to the long-time dynamics of condensed materials. We define interfacial 'mobility' of NPs in terms of the relaxation time τα, defined from the decay of the intermediate scattering function, or particle diffusion coefficient of the particles in the interfacial region. The Localization Model predicts that τα, which can be as large as minutes for temperatures near T_g, and even much larger below T_g, is generally related to the mean square atomic displacement $\langle r^2 \rangle$ at a characteristic caging time tcage on the order of a ps, $[\langle r^2(t_{cage}) \rangle \equiv \langle u^2 \rangle]$,

$$\tau_\alpha(T) = \tau_\alpha(T_A)exp\left[\{\langle u^2(T_A)\rangle/\langle u^2(T)\rangle\}^{3/2} - 1\right] \qquad (4.1)$$

where $\langle u^2\rangle$ is the DWF and TA is the characteristic temperature above which τα shows Arrhenius temperature dependence. [8,18,25] We determined the onset temperature T_A in the glass-forming liquids following the same procedure described in our previous work for Cu-Zr metallic glass systems. [14] Relaxation is Arrhenius above T_A and non-Arrhenius below T_A. According to the entropy theory of glass-formation activation enthalpy, the activation enthalpy ΔH_a (T) for the structural relaxation time τα follows a universal quadratic temperature relation, ΔH_a $(T)/\Delta H_a(T_A)\approx$ $1 + C(T/T_A - 1)^2$, predicted by the generalized entropy theory of glass-formation [1] in the T range near the onset temperature for non-Arrhenius dynamics. We have found that this relation describes the T dependence of ΔH_a (T) in a wide range of metallurgical materials. [7,14,157] and this form has also compared favorably to polymeric glass-forming materials. [229] We note that the equivalent of this expression has also been advocated for the viscosity of metallic glass materials over a large T range below T_A by Egami and coworkers, [230] where this form is referred to as the Modified Parabolic or BENK model. The work of Egami and coworkers is also notable for its strong emphasis of the physical importance of the inset temperature of non-Arrhenius dynamics, T_A.

The diffusion coefficient D can also be predicted from the LM when Eq. (4.1) is confined with the 'decoupling' or 'fractional Stokes–Einstein' relation, [19] $D/T \sim (\tau_\alpha)^{1-\zeta}$, where ζ is the so-called decoupling exponent,

$$ln[\{D(T)/T\}/\{D(T_A)/T_A\}] = (1 - \zeta)\left[\{\langle u^2(T_A)\rangle/\langle u^2(T)\rangle\}^{3/2} - 1\right] \qquad (4.2)$$

Initial work studying the LM emphasized glass-forming bulk materials such as polymer melts [18] and metallic glasses [8], but it was later found that the model also applied remarkably well to superionic UO_2, a crystalline material with highly anharmonic interactions. [9] The surprising success of the LM led us to recently test the capacity of the LM to describe the local interfacial

dynamics of model thin crystalline (Cu) and metallic glass (Cu-Zr) films where again the LM performed remarkably well. It is a natural next step to extend our analysis to the technologically important case of crystalline and metallic glass NPs having the same chemical composition as in our former thin film studies.

Our extension of the LM model to describe the interfacial dynamics of crystals is complicated by the anisotropy of $\langle u^2 \rangle$, D and τ_α, a complication that also exists even in bulk crystals. We investigated this anisotropy in our previous work and focused on these properties averaged over all lattice directions since the components of these properties are not generally measurable. We also discussed the interfacial dynamics of three different interfaces corresponding to distinct crystallographic orientations (100), (110), and (111) of crystalline Cu. The LM model worked on each interface having a different orientation. [7] Difficulties associated with accounting for local crystallographic orientations do not exist in NPs composed of glass-forming materials.

Crystalline NPs have their own complications, however. The surface of the crystalline NP surface does not present a surface having a single crystallographic orientation, but at temperatures much lower than Tm are composed of multiple interfacial regions having different crystallographic orientation that are in competition for directing the organization and dynamics of particles on the NP surface. The particles in this interfacial region can clearly be frustrated in their interactions, making these systems more akin to grain boundary regions separating crystalline grains in polycrystalline materials where the frustration in interactions between the particles arises from the having different orientation of the grains relative to each other. [157] When NPs become sufficiently large, however, these crystallographic faces should start to decouple from each other so that each interface begins to exhibit the dynamics similar to a macroscopic crystal where each 'facet' of the particle surface has its own, and often rather distinct interfacial energy and dynamics. In previous

work, we have studied Ni NPs in the small nanoparticle limit when the radius of the NPs truly has a radius near 1 nm [62] and the opposite limit of an infinite sized particle, corresponding to the various crystallographic interfaces macroscopic crystalline Ni. [49] Simulations aimed at identifying of the 'critical' particle size' at which NPs start to resemble macroscopic crystals have not yet been performed, but measurements on Cu NPs in a silica matrix indicate that the NPs start exhibiting sharp first-order melting transitions similar to the melting of bulk crystals only when the NP size is greater than 20 nm [231] and we may expect the cross-over size to be in this range or somewhat larger in 'free' NPs that are not embedded in a matrix. Measurements on the binding of common blood proteins (albumin, fibrinogen, γ-globulin, histone, insulin) on water soluble Au NPs in solutions plasma approximating physiological concentrations indicate a general progressive increase in protein binding energy with increasing NP size up to a critical size near 50 nm, at which point the bound protein layer becomes similar to the bulk Au material. We think this somewhat complicated measurement provides a good indicator of the typical scale at which NPs acquire the physical characteristics of a bulk material, a phenomenon of direct significance for understanding the chemical activity and probably the toxicity of nanomaterials. These observations also have a bearing on the functioning of organic nanoparticles such as proteins. Future studies should resolve the nature of this crossover that qualitatively should influence the interfacial dynamics of NPs.

It should then come as no surprise that the interfacial dynamics of true NPs having a radius comparable to 1 nm is often more like glass-forming liquids than the dynamics of macroscopic crystalline materials. Since varying the NP size changes the degree of interfacial curvature, changing the NP size in this small regime alters the 'fragility' of the interfacial dynamics of crystalline NP interfacial layer. [29] We should note beforehand that the term 'fragility' refers to mathematical measures of the deviation from an Arrhenius dependence of the structural relaxation

time, shear viscosity and mass diffusivity of liquid materials cooled to low temperatures and this term has been used to a lesser extent in the description of highly anharmonic crystalline materials in which high non-Arrhenius diffusion and relaxation often highly prevalent. [28,29,49–51,157,232,233] Materials for which this deviation from Arrhenius behavior is said to be 'fragile', while those for which the deviation is relatively weak are termed 'strong', regardless of the physical origin of this phenomenology so that care should be taken in physically interpreting this term. In practical applications, 'fragile' materials often have a much stronger temperature dependence than 'strong' glass-formers and the terms 'short' and 'long' have often been applied to these materials, respectively, corresponding to the amount of working time that such materials allow in processing before they vitrify. The term 'fragility' is clearly a term of engineering significance than a fundamental property of glass-forming liquids. Xu et al. [234–236] have recently discussed the physical significance of fragility in the context of model polymeric glass-forming liquids where it is clarified that this quantity relates to a convolution of effects related to the extent of collective particle motion and the strength of interparticle cohesive interactions, which is not a property specifically related to glass-formation.

Our finding of a change in fragility upon varying NP size, which we observed and discussed in past studies of the interfacial dynamics of crystalline Ni NPs [29,51] is reminiscent also of previous simulation observations on fluids embedded in abstract curved ('hyperbolic') spaces. [236,237] Simply changing the size of the NP or other particle, such as an oil droplet with NPs segregated to its surface as in Pickering emulsions [238–241], would seem to offer an easier way to create glass-forming materials spaces of variable curvature. Simple nanoimprinting polymer surfaces [242,243] or adding NPs to glass-forming liquids [244], where the mobile interfacial zone refers to the polymer interfacial region rather than the NP interfacial region of the metal NP, provides additional natural ways of

creating curved boundaries on a nanoscale that have application significance. We may also expect the NP and substrate mobility interfacial zones to couple as in the dynamics of water to suspended proteins and this important topic is not even under current discussion.

As in NP glass-forming materials, there is no clear rationale for identifying any definite orientation on the crystalline NP surface in order to define anisotropic components of $\langle u^2 \rangle$, D and $\tau\alpha$ as in thin films. Given these special features of NPs and their inherently different dynamics from macroscopic crystalline materials of the same chemical species, it is not obvious that the LM should apply to the description of crystalline NPs of truly nanoscale dimensions. These considerations motivated our investigation of whether the Localization Model [18,26] can describe the interfacial dynamics of crystalline Cu and $Cu_{64}Zr_{36}$ metallic glass NPs having different diameters.

Condensed materials characteristically exhibit enhanced molecular mobility at the onset of glass transition temperature T_g in the materials exhibiting a strong tendency towards glass-formation and at the onset of Tammann temperature T_{TA} [82,83] in crystalline materials. The Tammann temperature T_{TA} demarks the onset of appreciable molecular mobility and reactivity [82,83] in crystalline materials. These temperatures (T_g and T_{TA}) are tabulated extensively in material science, in view of the many applications in which these temperatures have a significant impact on intended material properties and we have discussed this characteristic temperature extensively in our previous paper on the interfacial dynamics of thin crystalline and glass-forming materials. [7] Interestingly, both of these characteristic temperatures are related to the melting temperature T_m of the material by a factor typically about 1/2 or 2/3 times Tm in glass-forming materials that can also crystallize. [91,92] Below, we show a new method of estimating these characteristic temperatures

defined by the intersection of $\langle u^2 \rangle$ of the interfacial layer NP with $\langle u^2 \rangle$ of the bulk-like interior of NP core.

Apart from enhanced anharmonic and collective [29] motion in the interfacial dynamics of NPs, the large surface to volume ratio of these NPs often leads to a significant drop in Tm and Tg in crystalline and amorphous solid NPs. This trend generally leads to enhanced anharmonic interactions because T_m, and thus T_{TA} of crystalline NPs drop as the NPs become smaller [29,245–249], more easily bringing NPs into their chemically reactive T regime at given temperature, $T_{TA}(d_{NP}) < T > T_m(d_{NP})$. Our investigation of size effects on the dynamics of NPs is motivated by this shifting of the characteristic temperatures with NP size, which should have many practical consequences.

4.2 Simulation methodology

Molecular Dynamics (MD) simulation has been used to study Localization Model for interfacial layers of crystalline Cu and $Cu_{64}Zr_{36}$ metallic glass NPs. Largescale atomic/molecular massively parallel simulator (LAMMPS), developed in Sandia National Laboratories [32] is utilized for our MD simulations. The embedded atom model (EAM) potential developed by Mendelev et al [105] was used for the interatomic interaction for $Cu_{64}Zr_{36}$ alloy and another EAM potential developed by Mishin et al [250] was used for crystalline Cu. Periodic boundary conditions were applied on all three directions in this study. The simulation timestep used for all simulations of this study was 1 femtosecond. The Parrinello-Rahman algorithm [42] was applied to maintain constant pressure, the Nose-Hoover thermostat method was employed to control temperature, and Nose-Hoover style non-Hamiltonian equations of motion were used to perform time integration during the simulation. [40,41]

Metallic glass was made following the same method we discussed in our earlier study. [7] We started with a perfect face-centered cubic (fcc) copper crystal of 13,600 atoms within a simulation box having the approximate dimensions, 64Å × 64Å × 64Å. We replaced 36% of randomly selected copper atoms from the box by zirconium atoms. This mixture of 64% Cu and 36% Zr atoms were heated to 1500 K and kept at this temperature and zero pressure for 2 ns using isothermal-isobaric (NPT) ensemble to ensure homogeneity of the mixture. Nanoparticles with 60Å, 50Å, 40Å, 30Å and 20Å diameters (d_{NP}) were cut from this bulk liquid and vacuum layers were added on all sides. In order to make sure an atom is not interacting with its own image when using periodic boundary conditions, large vacuum layers (at least 30Å) were added in all three directions. The numbers of atoms were 6650, 3825, 2000, 850 and 250 for NPs with $d_{NP} = 60$Å, 50Å, 40Å, 30Å and 20Å, respectively. To obtain the equilibrium structure of NPs, we relaxed all systems at 1500 K in canonical ensemble (NVT) for 1 ns. The NPs were rapidly cooled down to 300 K with 1×10^{12}K/s cooling rate. In order to run isothermal relaxation simulations, restart files were saved after every 25 K temperature reduction. Similar to the metallic glass NPs, we started with a perfect FCC copper crystal with the same size (64Å long in all three directions) in LAMMPS. The system was relaxed for 1 ns in NPT ensemble. Nanoparticles with $d_{NP} = 60$Å, 50Å, 40Å, 30Å and 20Å are cut from a perfect Cu crystal and vacuum layers were added on all sides. The numbers of atoms were 9315, 5413, 2753, 1163 and 350 for NPs with $d_{NP} = 60$Å, 50Å, 40Å, 30Å and 20Å, respectively. All NPs were relaxed for 1 ns followed by heating from 300 K to 1500 K in NVT ensemble. Restart files were saved during the heating of crystalline Cu NPs in every 25 K temperature increments. Isothermal relaxations have been conducted for all metallic glass and crystalline Cu NPs at every 50 K T changes in NVT ensemble for a minimum 3 ns up to a maximum 20 ns, depending on T and NP size. In all cases, the simulation was performed after an equilibration

time longer or at least as long as the structural relaxation time, estimated from the self-intermediate scattering function. Structural relaxation time and diffusivity estimates were extracted from the results of each of those isothermal relaxation simulation runs.

Before starting our analysis, we take a quick look at some snapshots showing representative atomic configurations of the NPs. Figure 4.1a–c shows $d_{NP} = 40$Å Cu NP over a range of T. Figure 4.1b shows the NP near its Tammann temperature T_{TA} (see text) where it is apparent that the facets of the zero T crystal are beginning to become 'washed out'. The crystalline NP at the relatively high $T = 1150$ K has a rounded shape similar to the metallic glass NP shown in Figure 4.1d–f at all temperatures. The melting temperature is normally significantly depressed from its bulk value when NPs are made small. We have examined this effect in some detail in the case of Ni NPs. We expect T_{TA} to maintain its relationship to Tm, i.e., $T_{TA} \approx (2/3)T_m$, which makes this temperature much lower in small NPs. This is important because the onset of the catalytic activity of metal has often been found to be correlated with T_{TA}, and we test this expectation below. The onset temperature for mobility in the metallic glass NPs also occurs near the glass transition temperature T_g, which as obeys the relationship, $T_g \approx (2/3)T_m$ where Tm is NP size dependent. It should also be noted that an fcc lattice structure is no longer an energetically stable structure when the diameter of NPs is smaller than 1 nm or N ≤ 200 atoms, instead low icosahedral or other non-crystallographic symmetry structures have often observed in numerous experimental and computational studies, [251–254] suggesting the potential energy in this type of particle packing is lower than the fcc packing of the bulk crystal. In addition, our previous study of dynamics of Ni NPs [62] shows that T_m oscillates for small diameter NPs or N < 300, revealing a 'magic number' phenomenon where the peaks in the T_m values normally occur close to the atomic number N values

(13, 55, 147, 309, ...) for which the NP form highly stable Mackay icosahedron structures or related structures having tetrahedral symmetry at low T. [255,256]

Below, $Cu_{64}Zr_{36}$ metallic glass NPs with $d_{NP} = 60Å$ will be referred as MG-d60A and crystalline Cu NPs with $d_{NP} = 60Å$ will be referred as Cu-d60A. The interfacial layer of MG-d60A is referred to as MG-d60A-S and the interfacial layer of Cu-d60A as Cu-d60A-S, etc.

4.3 Results and discussion

First, we determined the interfacial layer thickness (λ) of the NPs. We started with calculating the Debye–Waller Factor ($\langle u^2 \rangle$) against the radial distance R from the center of the NPs. As we discussed in our earlier study [7], DWF is the average square displacement $\langle r^2 \rangle$ of the atoms after a characteristic caging time τ_β. We define the Debye–Waller factor by the relation, $\langle u^2 \rangle = \langle r^2(\tau_\beta) \rangle$, where τ_β is the 'caging time' fast beta relaxation time, defined by the emergence of a plateau after the initial first decay of the intermediate scattering function. [107] This time can be determined at the minimum of the logarithmic derivative $d(ln\langle r^2(t) \rangle)/d(\ln t)$ and it typically has little T dependence and in the present study we simply take τ_β to equal 2 ps, following Leporini and coworkers [4,26] and our previous works. [7,8] We fitted the $\langle u^2 \rangle$ curves plotted against R to determine interfacial mobility scale λ where atoms have enhanced average mobility. As we described in earlier studies, $\langle u^2 \rangle$ decay exponentially from the surface, [7,49,76,140] and we fit the $\langle u^2 \rangle$ versus R based on equation, [141]

$$\langle u^2 \rangle = \langle u^2 \rangle_{core}[1 + \delta u \, exp(-x/\xi)] \qquad (4.3)$$

$$\delta u \equiv [\langle u^2(x = 0) \rangle - \langle u^2 \rangle_{core}]/\langle u^2 \rangle_{core}$$

where $\langle u^2 \rangle_{core}$ is the $\langle u^2 \rangle$ at the core or interior of the NPs where the $\langle u^2 \rangle$ is almost constant over radius, $\langle u^2(x = 0) \rangle$ is the $\langle u^2 \rangle$ at the outermost surface of the NPs and ξ is the $\langle u^2 \rangle$ length scale gradient. This equation can also be simplified to the form, [59,60,108,141,142]

$$\langle u^2 \rangle = \langle u^2 \rangle_{core} + A exp(- x/\xi) \tag{4.4}$$

where A is specified by Eq. (4.3). The onset of the NP interfacial layer is defined by the condition that the radial position at which $\langle u^2 \rangle$ value is 5 % larger than the magnitude $\langle u^2 \rangle$ values inside the core of the NP and the outer extent of this layer defined by the position of the outermost atom in this peripheral region of the NP. [7,29,51,76] Figure 4.2 shows the $\langle u^2 \rangle$ gradient as a function of distance R from the center of crystalline Cu and $Cu_{64}Zr_{36}$ metallic NPs with $d_{NP} = 60Å$ for a range of T.

Figure 4.3a shows the interfacial layer thicknesses for MG-d60A, MG-d30A, Cu-d60A and Cu-d30A NPs. The interfacial layer thickness tends increases with increase in T until it reaches to the characteristic temperature T_A, but then starts to decrease after T_A for metallic glass NPs. On the other hand, interfacial layer thickness keeps increasing with increase in T for crystalline Cu nanoparticles. The appearance of a non-monotonical temperature dependence and a peaking of the interfacial layer thickness in the $Cu_{64}Zr_{36}$ NPs was also observed in our previous work of $Cu_{64}Zr_{36}$ metallic glass and Cu crystalline thin films. [7] Zhang et al. [72] have recently discussed at length the non-monotonical temperature dependence of the width of the interfacial zone at length in glass forming polymer films, where the interfacial mobility scale was quantitatively related to the structural relaxation time rather than $\langle u^2 \rangle$ and where measurements confirming this apparent general trend are discussed. Apart from this being an observed general feature of the dynamics of glass-forming materials observed in both simulations and measurements performed so far, the explanation of this behavior must be speculative because of lack of a general

understanding of what controls the width of the interfacial zone under any conditions. We know that this scale does not scale with density, potential density and recent work has found that even the machine learning estimate of mobility, i.e., 'softness', is also highly inadequate. [257] Zhang et al. [72] have developed a mathematical model that semi-quantitatively describes the phenomenon based on a consideration of the very different slowing down of the dynamics in the free interfacial region and the interior of the material, but this model does no lead to any clear-cut physical 'explanation' of the ultimate cause of this intriguing and probably highly significant phenomenon. We note that is compelling simulation evidence that the change in the relative scale of the width of the interfacial mobility scale increases in a parallel fashion to the scale of string-like collective particle exchange motion in cooled liquids. [258] It is our suspicion that the interfacial mobility correlation length reflects the growth of intrinsic fluctuations associated with incipient glass formation in cooled liquids and with corresponding an incipient transition to a mobile fluid state when the material is heated from the glass state. However, we do not suggest this possibility in the present work since we really do not have the requisite data to support this hypothesis. Currently, we are working intensively to better understand the physical origin and nature of the interfacial mobile layer which is clearly important for understanding the reactivity and surface properties of both crystalline and glass materials. However, the exact reason for why this phenomenon occurs in the current metallic systems deserves further investigation. Interfacial and core $\langle u^2 \rangle$ as a function of T of crystalline Cu and $Cu_{64}Zr_{36}$ metallic glass NPs with $d_{NP} = 60$Å are shown in Figure 4.3b. A plot of $\langle u^2 \rangle$ against T shows linear trend at the lower (for example, 850K to 950K for MG-d60A-S and MG-d60A-C in Figure 4.3b). The DWF in interfacial region is much higher than in the NP core at the same T due to the highly anharmonic nature of the interatomic interactions in the interfacial zone. Despite the high mobility, the NP remains a crystal as defined by well-defined

lattice structure on average, but this solid has a high mobility so we may speak of a 'mobile solid layer' rather than a liquidlike interfacial layer. [7,76,131,134] We performed linear fitting over this T range and red and purple dotted lines intersect at 792 K. We estimate the onset temperature for glassy dynamics of the $Cu_{64}Zr_{36}$ metallic glass NPs having a diameter, $d_{NP} = 60$Å (MGd60A) to be ≈ 1205 K so we expect T_g should be near 800 K if we use the approximation $T_g \approx 2T_A/3$. [83] We also estimate Tammann temperature T_{TA} from the DWFs of the interfacial regions and core regions of the crystalline Cu and $Cu_{64}Zr_{36}$ metallic glass NPs, following the methodology utilized and described before for crystalline Cu and $Cu_{64}Zr_{36}$ metallic glass films. [7] We show our graphical estimation of T_{TA} for a crystalline Cu NP having a diameter, $d_{NP} = 60$Å (Cu-d60A) in Figure 4.3b. Green and blue dotted lines intersect at 770K, which is close to $T_{TA} \approx 2T_m/3 \approx 783$ K. Similarly, we found T_{TA} of crystalline Cu NPs having diameters, $d_{NP} = 40$Å (Cu-d40A) and $d_{NP} = 30$Å (Cu-d30A) are 745K and 700K, respectively. T_{TA} also decreases with a decrease in NP diameter in our crystalline Cu NPs, tacking the decrease in T_m. In particular, we find T_{TA} to retain its commonly observed phenomenology for bulk crystalline material, $T_{TA} \approx 2T_m/3$. We expect this result to be quite general and to be quite useful in estimating the onset of NP reactivity in applications.
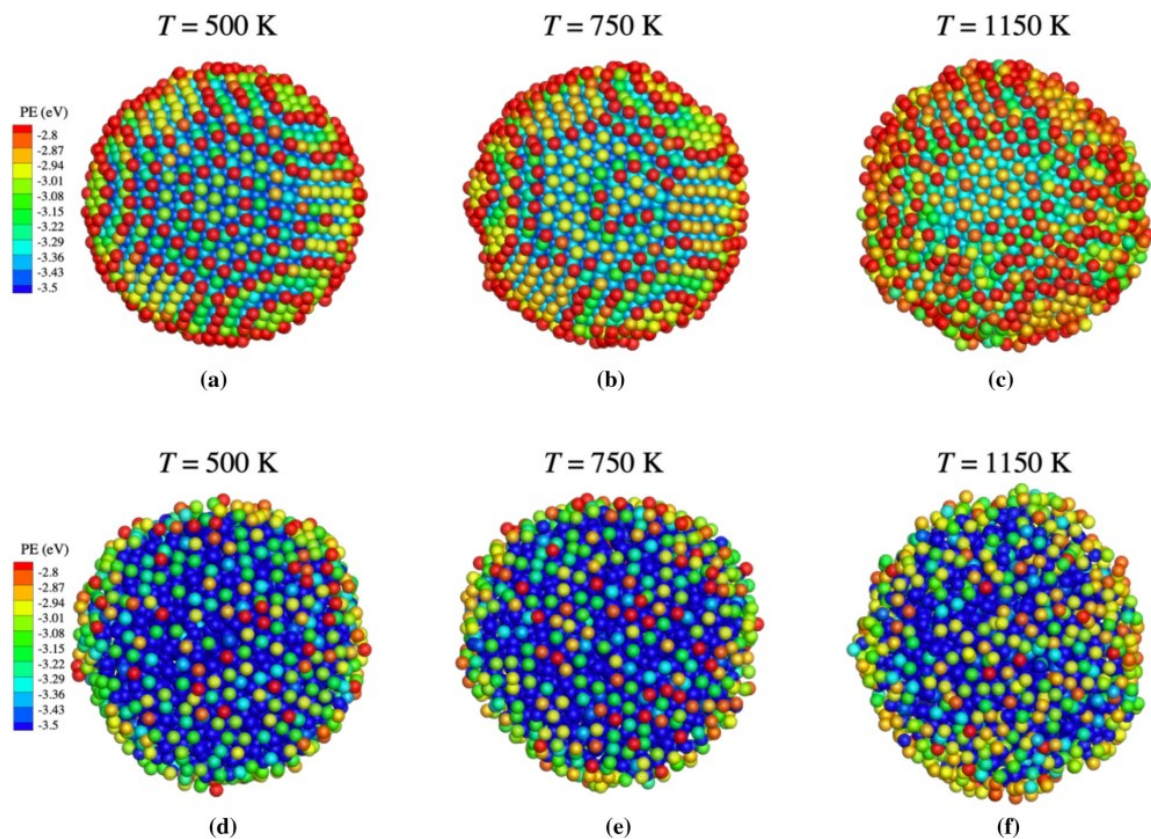
Figure 4.1: Snap shots of Cu and MG NPs at different T. The top images show the Cu NP below, at, and above the T_{TA}, where all Ts are below the T_m for a NP of this size, T_m (d_{NP} = 40Å; Cu = 1180K). Note the presence of islands of local order on the surface of crystalline NP even above T_{TA} and the NPs adopt a nearly roughly spherical shape, e.g., Gilbert et al. [259] even though they are in a crystalline state. The geometrical and properties of these NP are quite unlike the crystalline NP in its zero-temperature state in which faceted surfaces are normally highly prevalent. The normally 'round' nature of real crystalline nanoparticles is then a consequence of fluctuations of the interfacial atoms due to 'premelting'. The bottom image contrasts the crystalline NP with MG (d_{NP} = 40Å) NP having about the same size and at the same T as the crystalline Cu NP, which are correspondingly below, near and above the NP T_g. The presence of islands of persistently ordered regions on the surface of NPs below their T_m has been emphasized before by Wang et al. [260] and Zhang and Douglas [52] have discussed a rough analogy of this NP interfacial dynamics phenomenon with the plate tectonics in the earth's crust. Wang et al. [260] have also discussed the inherently heterogeneous nature of the interface of NPs in the premelting regime.
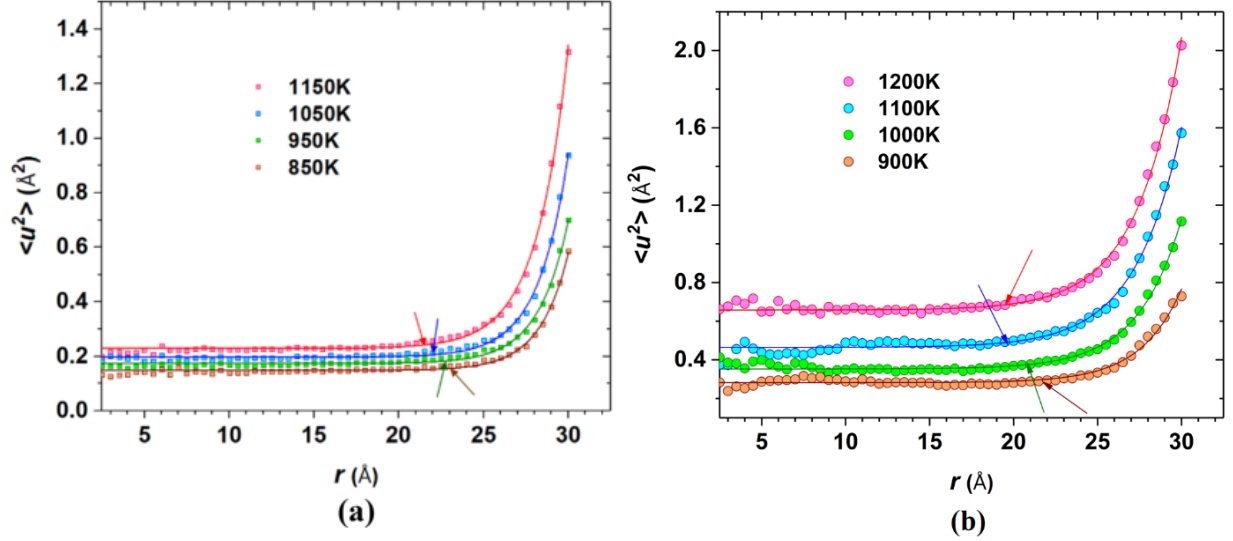
Figure 4.2: The $\langle u^2 \rangle$ gradient as a function of radial distance r from the center of NPs. **(a)** Crystalline Cu NPs with d_{NP} = 60Å (Cu-d60A) and **(b)** Cu$_{64}$Zr$_{36}$ metallic glass NPs with d$_{NP}$ = 60Å (MG-d60A) at different T. The solid lines are the fitted curve using the relation $\langle u^2 \rangle = \langle u^2 \rangle_{core} + A exp(-x/\xi)$. $\langle u^2 \rangle_{core}$ is approximately equal to the $\langle u^2 \rangle_{bulk}$ if the NPs have a significantly large core region. ξ values follow similar trend as the interfacial thickness with temperature, as shown in Figure 4.3a. For instance, ξ values for MG-d60A vary between 3.25Å and 6.26Å in the temperatures of interest. The fitted line is straight at the core but deviates near the interface. Nanoparticles with d_{NP} < 30Å do not have large enough cores for this this relation to apply. Arrows represent the point where $\langle u^2 \rangle$ increased by 5% from the core values.

Next, we calculated diffusivity D from the slope of mean square displacement (MSD) against time curve using the formula. A standard computational procedure is used to determine the diffusion coefficient, i.e,

$$D = \frac{1}{2} lim_{t \to \infty} \frac{d\langle \Delta r^2 \rangle}{dt} \qquad (4.5)$$

$$\langle \Delta r^2(t) \rangle = \frac{1}{N} \sum_i \left(r_i(t) - r_i(0) \right)^2$$

in the limit of long times, where $\mathbf{r}_i(0)$ and $\mathbf{r}_i(t)$ are i particle's initial and final atom positions after time t, respectively, and N is the total number of atoms. Needless to say, the Debye–Waller Factor $\langle u^2 \rangle$ is simply the MSD calculated between time $t = 0$ and $t = 2$ ps. We only consider the initial positions of particles to determine whether any particle belongs to the interfacial region or the interior of the NPs, because the number of atoms move out or into the interfacial region within the 2 ps time interval of any calculations is not significant. DWF at the interfaces as a function of T for MG-d60A-S, MG-d30A-S, MG-d20A-S, Cu-d60A-S, Cu-d30A-S and Cu-d20A-S are shown in Figure 4.4. Interfacial $\langle u^2 \rangle$ varies very slowly with decreasing diameter from 60Å to 40Å. The difference is so small between the interfaces of NPs with diameter 60Å and NPs with $d_{NP} =$ 50Å that they appear overlapping. Interfacial $\langle u^2 \rangle$ changes suddenly when the d_{NP} goes to 30Å when there is no core remains to significantly affect the overall dynamics of NPs and the whole NP behaves like an interface when $d_{NP} = 20$Å or below. The anharmonicity of the interatomic interaction is evidenced by a strongly nonlinear variation in $\langle u^2 \rangle$ with T that becomes especially prevalent in both the interfacial dynamics of crystalline and metallic glass materials. Unfortunately, we could not find any universal description of the T dependence of our $\langle u^2 \rangle$ data, and we leave the quantification of this overt anharmonicity for future work. Clearly, however, having a predictive model would be an essential ingredient in making the LM more predictive and we make a few comments about how this anharmonicity might be quantified.

We start with a comparison of the T variation of $\langle u^2 \rangle$ for the crystalline and metallic glass NPs in Figure 4.4 where the curvature reflecting the anharmonic interactions is clearly prevalent. It is generally appreciated that anharmonic interparticle interactions are a general feature of interfacial interparticle interactions [7,261] and in recent years sophisticated experimental methods such as extended x-ray-adsorption fine structure scattering measurements and corresponding

theoretical models of anharmonic dynamics have been developed to quantify this anharmonicity [262–268] which enable the determination of $\langle u^2 \rangle$ at higher temperatures, disordered systems and other systems in which anharmonicity is appreciable, as well as higher moments of the particle displacement distribution. We also note interesting work emphasizing significant changes of $\langle u^2 \rangle$, and anharmonic interparticle interactions, in materials exposed to radiation damage [269] and large changes in pressure. [68]
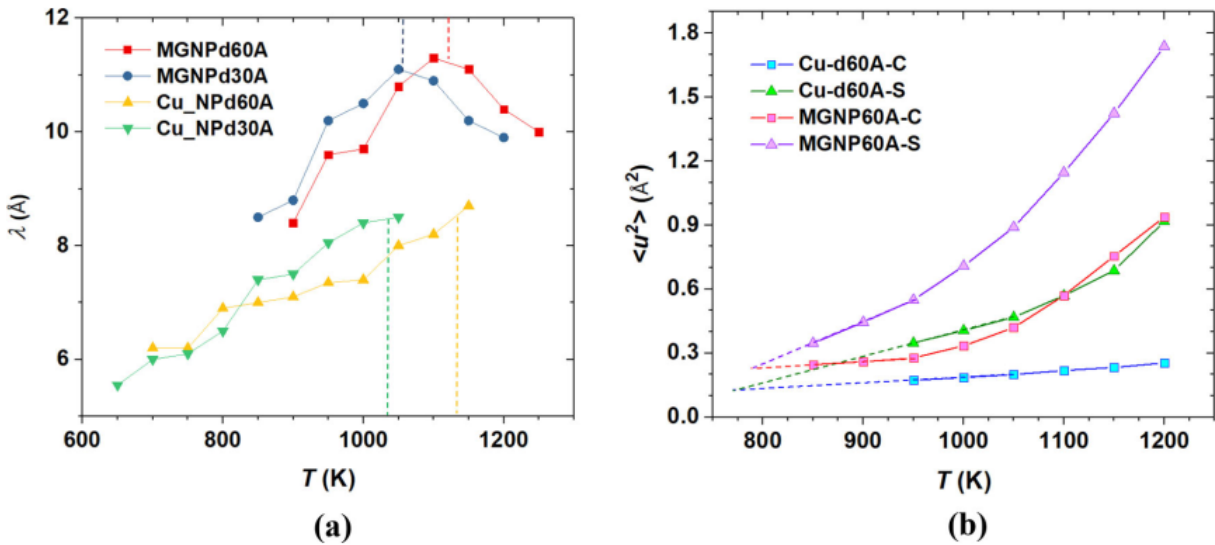
Figure 4.3: Surface thickness and Tammann temperature of nanoparticles. **(a)** Interfacial mobility scale λ as a function of T of crystalline Cu and $Cu_{64}Zr_{36}$ metallic glass NPs with $d_{NP} = 30\text{Å}$ and $d_{NP} = 60\text{Å}$ (Cu-d60A, Cu-d30A, MGd60A, MG-d30A). Vertical dotted lines represent T_A of the NPs. **(b)** $\langle u^2 \rangle$ as a function of temperature T at the interfaces and cores of crystalline Cu and $Cu_{64}Zr_{36}$ metallic glass NPs with diameter 60Å (Cu-d60A-S, Cu-d60A-C, MG-d60A-S and MG-d60A-C). An extrapolation of fit to our $\langle u^2 \rangle$ data is shown by the dotted lines. Extrapolated linearly fitted lines from interface and particle core regions intersect near the Tammann temperature T_{TA}. We find that T_{TA} coincides with T_g for the metallic glass NPs.
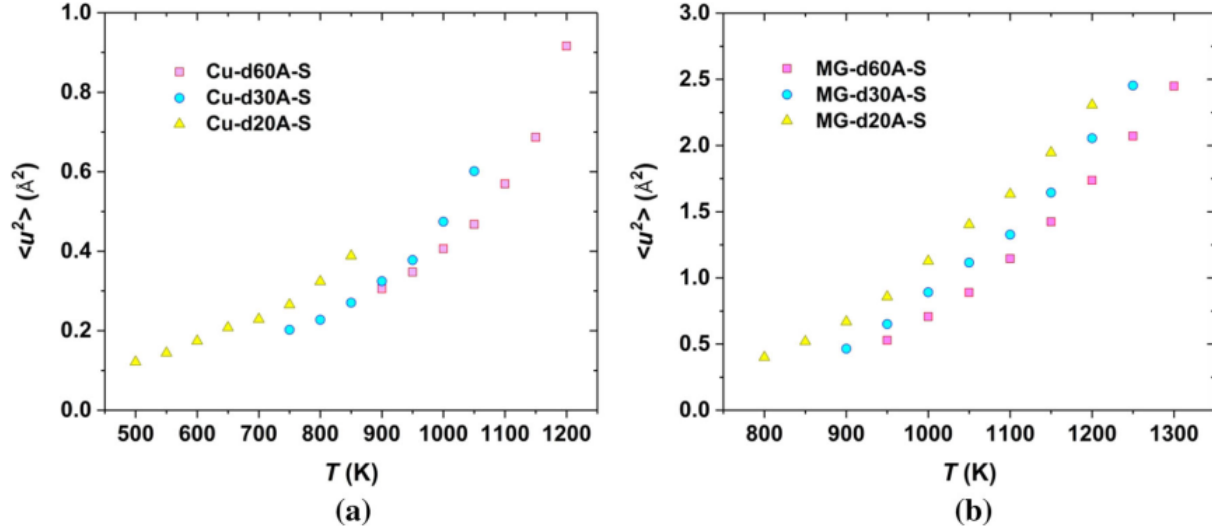
Figure 4.4: The average interfacial $\langle u^2 \rangle$ as a function of T of crystalline and MG NP.**(a)** Crystalline Cu NPs with $d_{NP} = 60$Å, $d_{NP} = 30$Å and $d_{NP} = 20$Å and **(b)** $Cu_{64}Zr_{36}$ metallic glass NPs with $d_{NP} = 60$Å, $d_{NP} = 30$Å and $d_{NP} = 20$Å at different T.

In recent studies, it has been found to be advantageous for experimental and modeling purposes to split $\langle u^2 \rangle$ into separate two pieces [270], a contribution $\langle u^2 \rangle_H$ arising from the harmonic interactions that dominate $\langle u^2 \rangle$ at low T when the particles are deeply trapped in their local potential wells and an anharmonic contribution $\langle u^2 \rangle_{Anh}$ estimated from measurement based on lattice dynamics calculations models incorporating anharmonic interparticle interactions that are appropriate to the given material. For bulk crystalline materials, $\langle u^2 \rangle_{Anh}$ has been determined to be proportional to the Grüneisen parameter γ_G, a standard measure of anharmonicity of interparticle interactions in strongly condensed materials and proportional to the thermal expansion coefficient of the material, a quantity that is simply zero in ideally anharmonic materials. This quantity provides an additional measure of anharmonicity that is often experimentally accessible. [270] Specifically, $\langle u^2 \rangle$ can be formally written in this general theoretical framework as,

$$\langle u^2 \rangle = \langle u^2 \rangle_H [1 + \delta \langle u^2 \rangle] \tag{4.6}$$

$$\delta \langle u^2 \rangle = \beta(T)[(\langle u^2 \rangle_H - \langle u^2 \rangle_0)/\langle u^2 \rangle_H]$$

Where $\langle u^2 \rangle_0 \equiv \langle u^2(T \to 0) \rangle$, the 'zero point contribution' to $\langle u^2 \rangle$ and the 'anharmonicity parameter' $\beta(T)$ equals, $\beta(T) = 2\gamma_G \delta V(T)$ where $\delta V(T) = [V(T) - V(T_0)]/V(T)$ is the relative change of volume of the material when T is changed from one temperature to another and T_o is a reference temperature below which anharmonicity effects can be taken as negligible so that $\langle u^2(T \leq T_0) \rangle \approx \langle u^2 \rangle_H$. This separation of $\langle u^2 \rangle$ into harmonic and anharmonic contributions has also been considered in an applications context of glass-forming materials where estimates of $\langle u^2 \rangle_H$ have been correlated with impact strength and toughness on polymer glass materials [271] and in connection to estimating the viscosity and relaxations of glass-forming liquids. [17,272] Equation (4.6) provides a natural starting point for modeling the temperature dependence of $\langle u^2 \rangle$ and for developing rational empirical estimates of this central parameter in the LM.

Diffusivity D at the interfaces as a function of T for $Cu_{64}Zr_{36}$ metallic glass NPs and Cu crystalline NPs with five different sizes are shown in Figure 4.5. Diffusivity at the interfaces of Crystalline Cu NPs and $Cu_{64}Zr_{36}$ metallic glass NPs show trends similar to the interfacial $\langle u^2 \rangle$. Note the inversion of the curvature of the Arrhenius plots of D for the crystalline and metallic glass NPs, as observed in our previous paper on crystalline and metallic glass films. [7] This change in curvature is characteristic of crystalline and glass-forming materials, as discussed in our previous work. [7] The curvature in Arrhenius plots of D are often relatively small in common crystalline metals, but in some materials involving heavy elements the non-Arrhenius dynamics is highly prevalent. [273,274] Anharmonic effects are evidently quite large in white phosphorous, for example, where the Arrhenius curve for D is highly curved upward upon approaching the melting temperature. [275] This relatively high curvature also tends to be rather strong in the interfacial

dynamics of crystalline materials where the curvature exhibits some universality when T is reduced by T_m. [49,74,75,276]
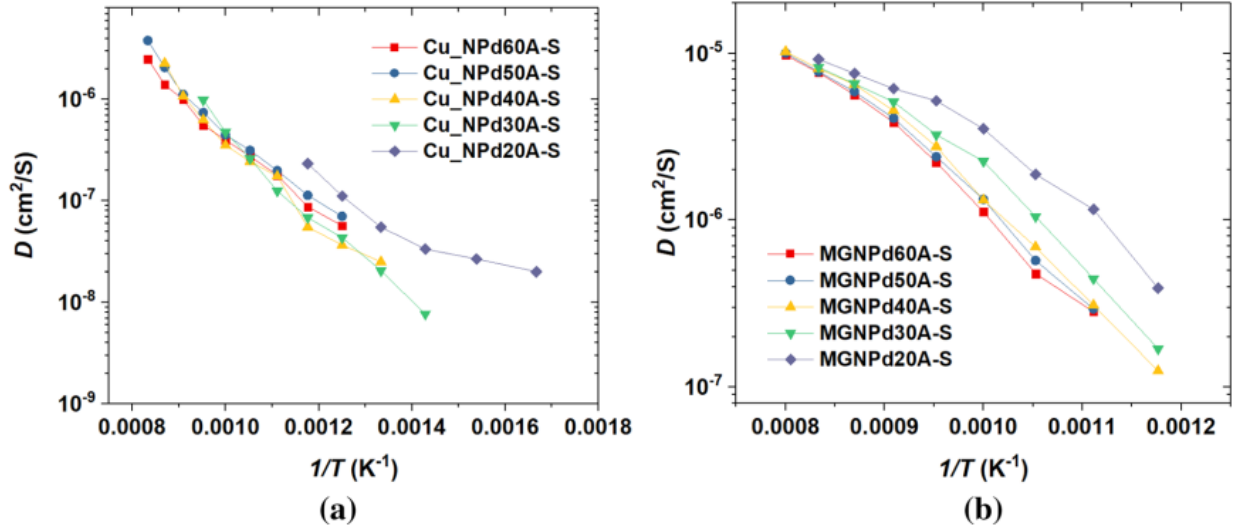
Figure 4.5: The interfacial diffusivity D as a function of T of crystalline Cu and MG NP. **(a)** Crystalline Cu NPs with different d_{NP} and **(b)** $Cu_{64}Zr_{36}$ metallic glass NPs with different d_{NP} at different T.

We obtain our estimate of the interfacial relaxation time in the usual way from the self-intermediate scattering function, F_S (q, t). This quantity is the Fourier transform of van Hove correlation function $G_s(r, t)$ describing the probability of particle displacement to a distance r from a given initial position in time, t. [277] For Brownian motion, $G_s(r, t)$ is just Gaussian function, but the strong anharmonic interactions in condensed materials cause to exhibit a more complicated variation in both crystalline and glass-forming materials. The Fourier transform of $F_S(q, t)$ is normally determined in experimental studies and in Figure 4.6 we show this quantity for the interfacial regions of both our crystalline and metallic glass NPs, where the variation of $F_S(q, t)$ with t is rather typical of the phenomenology of glass-forming liquids, a point made before in our

paper comparing the interfacial dynamics of crystalline and metallic glass films. [7] We notice an initial decay associated with the fast inertial dynamics that terminates at a caging time on the order of a ps over which a plateau in $F_S(q, t)$ emerges. [107] This initial decay is rather insensitive to T and characteristic of atomic and molecular liquids broadly. However, the structural relaxation time $\tau\alpha$ is determined from the second decay of at long times. In particular, $FS(q, t)$ is conventionally fit to a stretched exponential dorm $F_S(q,t) \propto exp(t/\tau_\alpha)^{\beta s}$ and τ_α is determined from this fit. As with quite numerous studies of glass-forming liquids in the past, we find our comparisons to this expected form for a range of NP sizes at $T = 1000$ K to describe our data for both the interfacial dynamics of the crystalline and metallic glass NPs rather well where, β (crystalline Cu) = 0.5 to 0.56 and β (Cu$_{64}$Zr$_{36}$) = 0.4 to 0.6 and our $\tau\alpha$ estimates are indicated below. We see that the β values of the crystalline NPs are almost constant and independent of size for the range we investigate, but β *seems to* increase somewhat as the particle diameter decreases in the case of the metallic glass NPs. It is not so obvious, perhaps, that the same functional form for $F_S(q, t)$ should apply to both the interfacial dynamics of crystalline and metallic glass NPs, but we find that this is indeed the case. This confirms our arguments above that the interfacial dynamics of crystalline materials should resemble glass-forming liquids (Equivalence is not implied here, however.). These observations are also consistent with our observations on crystalline films of Cu. [7]

We are now in apposition to test the localization model predictions for structural relaxation time τ_α and diffusion D in the interfacial regions of crystalline Cu and Cu$_{64}$Zr$_{36}$ metallic glass NPs. The onset temperature T_A was determined by following the steps described in detail in our previous work, [7] predicted by the generalized entropy theory of glass-formation [1] in the T range near the onset temperature for non-Arrhenius dynamics, as discussed in the Introduction. The LM predictions for the interfaces of crystalline Cu and Cu$_{64}$Zr$_{36}$ metallic glass NPs are presented in

Figure 4.7. We note that while there is some scatter, there are no free parameters in the localization model prediction for τ_α, but the LM predictions for D require an estimate of the decoupling exponent ζ using fractional Stokes-Einstein relation. We estimated the decoupling exponent for these systems to equal: ζ (Crystal Cu) = 0.23 to 0.4
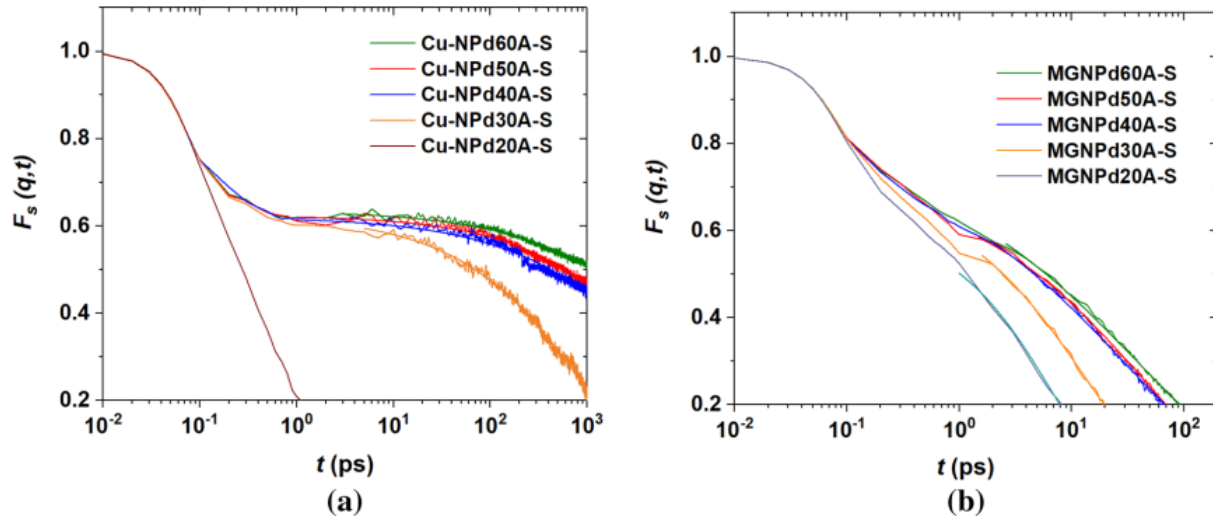
Figure 4.6: Self-intermediate scattering function of interfacial regions of nanoparticles. **(a)** Crystalline Cu NPs and **(b)** $Cu_{64}Zr_{36}$ metallic glass NPs with different d_{NP} at 1000 K.

We also tested the localization model predictions for structural relaxation time τ_α and diffusion D of overall $Cu_{64}Zr_{36}$ metallic glass NPs and compared their interfaces. Figure 4.8 shows the localization model prediction for interface and overall metallic glass NPs. Again, the LM predictions of D require estimates of ζ. We obtained a ζ estimate of about $\zeta \approx 0.5$ for both the NP interfacial region and metallic glass NPs as a whole, although there seems to be a systematic departure from a simple power law 'decoupling' relation between D and τ_α in these NPs a deviation that we do not see in the bulk materials and thin films.
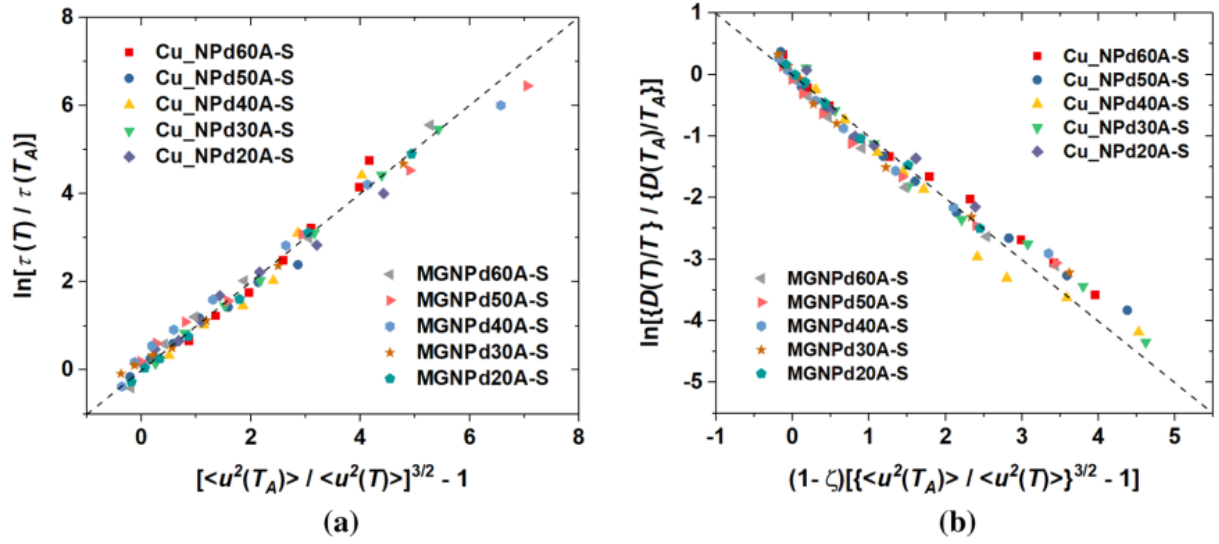
Figure 4.7: Test of Localization Model predictions for crystalline and metallic glass NPs. LM prediction for **(a)** the structural relaxation time τ_α **(b)** the diffusion coefficient D in the film interfacial regions of crystalline Cu and $Cu_{64}Zr_{36}$ metallic glass NPs.
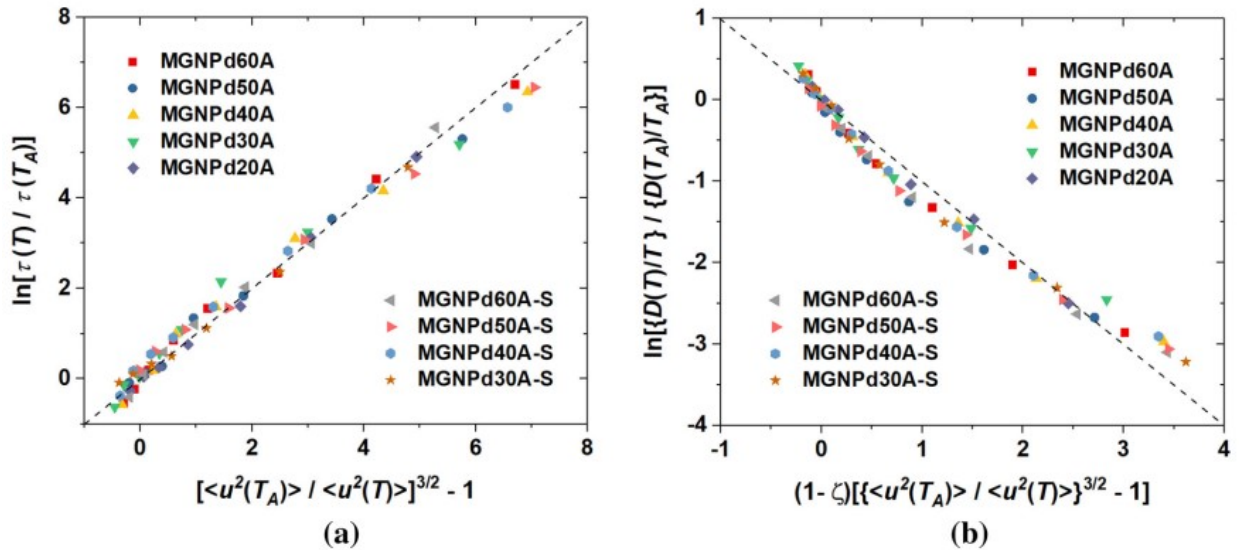
Figure 4.8: Test of Localization Model predictions for metallic glass NPs. LM prediction for **(a)** the structural relaxation time τ_α **(b)** the diffusion coefficient D in the film interfacial regions and overall $Cu_{64}Zr_{36}$ metallic glass NPs.

4.4 Conclusions

We have found that the localization model of the dynamics of condensed materials is able to account quantitatively for the temperature dependence of the structural relaxation time in the interfacial regions of both metallic glass and crystalline nanoparticles, extending our previous finding for the localization model to describe the structural relaxation time in interfacial region of thin films of crystalline and metallic glass materials and the dynamics of model metallic glass and crystalline materials in their bulk state. Together, these results are very encouraging regarding the generality of the localization model to a wide range of condensed materials, making the model potentially very useful in developing applications of nanoparticles and other nanostructured objects and patterns that rely on the control of interfacial dynamics.

Chapter 5: The Dynamics of Metal Nanoparticles on a Supporting Interacting Substrate

The interaction strength of the nanoparticles NPs with the supporting substrate can greatly influence both the rate and selectivity of catalytic reactions, but the origins of these changes in reactivity arising from the combined effects of NP structure and composition, and NP-substrate interaction are currently not well-understood. Since the dynamics of the NPs are implicated in many NP-based catalytic processes, we investigate how the supporting substrate alters the dynamics of representative Cu NPs on a model graphene substrate, and a formal extension of this model in which the interaction strength between the NPs and the substrate is varied. We particularly emphasize how the substrate interaction strength alters the local mobility and potential energy fluctuations in the NP interfacial region, given the potential relevance of such fluctuations to NP reactivity. We find the NP melting temperature T_m progressively shifts downward with an increasing NP-substrate interaction strength, and that this change in NP thermodynamic stability is mirrored by changes in local mobility and potential energy fluctuations in the interfacial region that can be described as "colored noise". Atomic diffusivity D in the "free" and substrate NP interfacial regions is quantified and observed variations are rationalized by the localization model linking D to the mean square atomic displacement on a "caging" timescale on the order of a ps. In summary, we find the supporting substrate strongly modulates the stability and dynamics of supported NPs, effects that have evident practical relevance for understanding changes in NP catalytic behavior derived from the supporting substrate.

5.1 Introduction

In diverse applications of nanoparticle (NP) catalysts in the synthesis of new materials and in energy conversion and materials recycling applications, the NPs are utilized by dispersing them on solid substrates [278,279], which serves to optimize chemical reactivity and inhibit their coalescence. It is generally appreciated that the chemical nature of the supporting substrate [280–287], along with the size and shape of the NPs [288–292], can significantly influence NP structure and catalytic reactivity so that there are physical, as well purely chemical, aspects of understanding this type of heterogeneous catalysis. Given the significant economic contribution of this type of catalysis reaction to the world's economy [293,294], there has correspondingly been much interest and scientific effort aimed at better understanding how NP composition, structure and the presence of an interacting substrate collectively give rise to strong variations in the rate and selectivity of catalytic reactions [283,294,295]. The ultimate goal of this type of research is to learn enough about the underlying physics of NPs, and their reactions, to actually *design* catalysts [279] that are optimal for producing new functional materials at a minimal economic cost and environmental impact [296]. An understanding of the dynamics of NPs on substrates is also of primary concern in the "stability" of catalysts since coalescence associated with the high interfacial mobility of NPs under reaction conditions often results in a significant reduction or complete loss of catalytic behavior. The challenge is to minimize this NP coalescence process while retaining NP reactivity.

Currently, the development of catalysts remains more of an art than a science, but new experimental methods probing the structure and dynamics of individual NP under reactive conditions have opened a window into the physics of these fascinating materials [285,297–301]. It is observed, for example, that many "ultrafine" NPs, whose size is on the order of a few nm or

smaller, can be highly effective heterogeneous catalysis materials, and that their shape and reactivity have been found to fluctuate [298–301] in apparent concert with their catalytic activity. [302] Even Au, which is normally considered a rather chemically inert material, can become highly reactive in an "ultrafine" particle size regime [303] This size-dependent change in reactivity has rather obvious ramifications for understanding the potential toxicity of NPs. Moreover, the optical properties, conductivity and band structure of ultrafine NPs have been observed to characteristically fluctuate in a similar highly intermittent fashion. [304,305] The "blinking" of the fluorescence intensity of quantum dots [305–307] can also be classified in this same category of fluctuation phenomena. In our investigation below, we observe and quantify property fluctuations, which are *intrinsic* to the dynamics of NPs.

These shape and property fluctuations are accompanied by high interfacial mobility of the crystalline NPs and by a general tendency for NP coalescence [203,219], which can compromise catalytic function. Interestingly, the shape of NPs can change in a reversible way when the reaction conditions and thus the chemistry of the substrate and the NP surface are altered [218,308] At first, it might be imagined that this change of NP structure and dynamics, and the emergence of "liquid-like" hydrodynamic properties, such as rapid particle coalescence and NP diffusion [203,219], is due to a large downward shift of the melting temperature T_m because of reduced NP size to a temperature (T) range over where the reaction occurs or the imaging measurements are performed. Accordingly, Cervates-Sodi and coworkers [309] describe "ultrafine" metal NPs under conditions where the particles show liquid-like mobility as being in a "viscous" state. However, Sun et al. [214] found that metal NPs in this "liquid-like" state can at the same time exhibit a high degree of crystalline structural order. Such NPs can also exhibit a paradoxical "pseudo-elasticity", in which there is full recovery of their shape after the NPs are significantly deformed. High-resolution

observations of crystalline Ga NPs have further revealed that the core of metal NPs can be in a solid-like state reminiscent of the bulk crystalline material, but at the same time the interfacial region of these crystal NPs can be in a highly mobile in which there is a "dynamic coexistence" between the interior and surface regions of the NPs. [25] One of the goals of our work below is to clarify the overall nature of the dynamics of NPs to enable a more unified description of their unique properties.

As a matter of related scientific interest, there has been intense interest in growing carbon nanotubes (CNT) using metallic NPs as the catalyst [26–28] and this has prompted atomic resolution imaging studies aimed at understanding and controlling CNT morphology and kinetics. In this context, it has often been observed that the metal NPs catalyzing the CNT growth are in a highly dynamic state under CNT growth conditions, where the NP interfacial fluctuations and their high interfacial mobility evidently have a direct impact on the structure of the CNTs grown from these "templates". [87,310–312] The study of CNT growth, and specialized efforts to understand and then engineer their chiral structure, along with other desirable aspects of their geometry, provide a continuous source of new information about metal NP interfacial dynamics. Data of this origin has proven to be valuable in our discussion below.

One of the most intriguing observations on the catalytic behavior of "ultrafine" metal particles supported on substrates, from the standpoint of the present study, is the observation of a temperature (T) range in which "dynamic coexistence", characterized by a spontaneous "surface restructuring" along with changes in the degree of NP crystallinity occur in time. Moreover, this phenomenon can be greatly altered when the NPs are supported on surfaces having a high affinity for the NPs. [280, 216] Our estimates of the NP melting temperature and the Tammann temperature T_{TA} (defined and estimated below) at which NP "premelting" initiates, indicate the overall breadth

of NP melting transition becomes progressively larger when the NP is supported on a substrate having a larger attractive interaction with the substrate. This phenomenon has crucial consequences for NP catalysis because T_{TA} is often directly associated with the onset of catalytic activity. [87,221,281] and this characteristic temperature is a recognized fundamental parameter in the design of heterogeneous catalysts. [6,7,86,87,198,221,281] Given the practical importance of T_{TA} in the engineering materials for heterogeneous catalysis applications, we quantitatively determine this characteristic temperature and its dependence on the NP-substrate interaction. It is evident from numerous previous experimental studies that some aspects of the dynamics of NPs derive or at least are greatly influenced by the supporting substrate and it is these observations that primarily motivate the present study. While there have been reports on changes in T_m of NPs supported on substrates in previous molecular dynamics simulations on small particle clusters [313–315], the existing findings are too fragmentary to conclude agreement or disagreement with the experimental trends just mentioned, and further simulation studies are warranted. We note that there have also been highly instructive simulations focusing on the vibrational dynamics of NPs supported on solid substrates [316,317] and simulations have provided insights into the mechanism of large spontaneous shape fluctuations that are characteristic of the dynamics of ultrafine NPs at elevated T, but still below their T_m [62].

Although a change in the structure of idealized low temperature perfectly crystalline NPs in isolation and supported on an attractive substrate under equilibrium conditions is expected from the Wolf construction [318] for "free" NPs and from the corresponding Winterbottom construction for substrate supported NPs [319–321], the NP shape becomes more complicated in the "premelted" regime where catalysis reactions are often performed. Nonetheless, the NPs are still crystalline "solids" in this regime so it is somewhat surprising that these crystalline NPs can rapidly

reconfigure their shape when the NP surface interaction is altered through a change of reaction conditions [319]. This "weird" phenomenon provides further, albeit indirect, evidence of a relatively high atomic mobility in "ultrafine" metal NPs. Another commonly reported attribute of heterogeneous catalysis reactions with metal surfaces is that catalytic behavior appears to be concentrated on the "non-crystalline" component of the catalyst.[38] These observations, and arguments relating to the possible existence of highly localized reactive regions on the NP surface, motivate the quantification of local potential energy and mobility fluctuations on the NP surface that might account for these hypothesized localized reactive regions.

Shifts in T_{TA} have been extensively discussed in the extensive literature on using metal NPs of different composition substrates to control CNT diameter and chiral structure. [87,198] Measurements also show that significant NP superheating can be achieved by embedding metal NPs in a matrix of another material, such as capping the NP with a graphene layer [231,322]. This type of measurement provides a testing ground for studying how the geometry of the interfacial constraints alters NP stability and reactivity, an important concern in applications. Recent work has shown that NP encapsulation can give rise to a significant stabilization of metal NPs against coalescence, while at the same time preserving their catalytic activity. [323] This type of NP interfacial engineering should then have many potential applications, and then motivates the quantification and predictive modelling of the atomic diffusivity of the NP interfacial atoms in regions having different curvatures. In our development below, we make "maps" of local mobility variations in the interfacial region of our simulated supported NPs.

As a background to the current study, our group has studied crystal melting, and the mobile interfacial layer in the mobile crystal phase of NPs [29,51,52], crystalline thin films [6,7], as well as the interfacial regions [49,76] and grain boundary regions [157] of bulk crystalline materials where the

crystalline material likewise exists in a mobile state somewhat similar in nature [6,7] to superionic crystalline materials [28] in which the material is crystalline, but where the atomic species counter-intuitively have liquid-like mobilities. This phenomenon is also emphasized in recent experimental studies of small crystalline NPs at elevated T, but where T is still below T_m. [310] Note that the loose term "premelting" does not mean that the interfacial region of the crystalline material can be described as being "liquid", as the interfacial region may retain a significant degree of order on average, while at the same time the atomic mobility is comparable to a typical liquid, a physical situation that arises in superionic crystalline materials.

In the present work, we extend our previous work on "free-standing" NPs to the case of a metal NP in contact with a solid substrate. As a representative NP, we choose a model crystalline Cu NP composed of 10, 000 Cu atoms and having a radius of about 6.2 nm. Since graphene [324–326] and graphene derivatives such as graphene oxide [327–329] are prevalently utilized as a support in catalysis applications and because the interaction potentials between Cu and are available, we first considered the representative specific model of Cu NPs supported on a graphene substrate. We found, however, that our Cu NPs did not have a high affinity for graphene, so we then extended this model to one in which the NPs have a stronger affinity for the substrate. This extension is based on the experimental observation that graphene tends to oxidize at elevated temperatures when exposed to oxygen, which we may expect to lead to an enhancement of the interaction of the NP with the substrate. This extended model is also motivated by the common use of metal oxide substrates as an NP support in catalysis applications where the attractive interaction between the NP and the substrate can likewise be expected to be relatively attractive. Since these interfaces in real materials are normally highly complex chemically, we were guided in our specific modelling of these interfaces by experimental studies of the morphology of supported NPs. In particular, we

simply "tuned" the interaction strength in the extended substrate model described above to qualitatively reproduce experimentally observed changes in NP shape in the "pre-melting" regime where catalytic reactions are often performed.

Our analysis of the simulated NPs supported on these model planar interacting substrates largely follows our former analysis of "free-standing" metal NPs, where we quantify the thickness of the mobile interfacial layer and the diffusivity in this layer, as well as diffusivity in the NP interior. A new feature of the present study is that a distinct mobile interfacial layer arises near the supporting substrate that is distinct from the "free" boundary interfacial region. In the system undergoing catalysis, this "free" boundary is exposed to reactive gases, but we do not include such reactive species in the present simulations. Rather, the current work focuses instead on the structure and dynamics of a model crystalline metal NP on an interacting substrate, where, as described above, we model in a rather idealized fashion in comparison to the chemically complex substrates encountered in real catalytic materials. We then view the current work as being a preliminary step in the direction of modelling catalysis of reactions of NPs on a supporting substrate.

After quantifying the large gradient in the interfacial mobility in our substrate-supported NPs, again following methods used in our recent work on free-standing NPs [6], we investigate fluctuations in the local potential energy and mobility in the interfacial region in view of the potential importance of such fluctuations in catalysis reactions involving metal NPs. In our previous work on free-standing metal NPs, we found that the potential energy and particle mobility exhibit correlated fluctuations that can be described by colored noise. [51] This observation of this correlated noise provides an opportunity for quantifying these fluctuations and metrology for

manipulating these fluctuations by controlling NP size, the surface composition of the substrate, temperature, and the interaction strength between the NP and the substrate.

Recently, there has been progress in directly modeling the catalytic reaction of a crystalline nanoparticle (Pt) supported on graphene with a model polymer material of interest in converting polymer waste materials into new monomer material that can be used to make new materials, i.e., "chemical recycling", by molecular dynamics simulation [330]. In this complementary work, the dynamics of the NPs was *completed neglected*, and the focus was instead on modelling the catalytic reaction where the NPs were treated as being fixed in shape and without any internal dynamics. Ultimately, the realistic modeling of the NP catalysis requires a more general treatment that considers both the dynamics of the NP on a supporting substrate, and the dynamics of the chemical reaction.

5.2 Simulation Details

All simulations in this study are conducted using molecular dynamics (MD) simulation which was performed using Large-scale atomic/molecular massively parallel simulator (LAMMPS), developed by Sandia National Laboratories [32]. The Nose-Hoover thermostat method is used to control temperature and Nose-Hoover style non-Hamiltonian equations of motion is applied for time integration during the simulation [40,41]. Constant pressure is maintained using Parrinello-Rahman algorithm [42]. Simulation timestep is 1 femtosecond (fs) for all simulations of this study. We start with creating a perfect face-centered cubic (FCC) copper crystal using LAMMPS simulation at 300 K. After relaxing the perfect Cu crystal at 300 K for 2 ns in NPT ensemble, a spherical part with 10, 000 atoms is cut to make a free-standing (FS) copper

nanoparticle (Cu NP) in a vacuum. A graphene (C) substrate is added under a Cu NP for simulation

of Cu NP on graphene substrate so that the (110) crystallographic plane of Cu crystal is parallel to

the graphene substrate. The Cu NP has a diameter close to 62 Å when free-standing and the

graphene substrate is approximately 120 Å × 120 Å at 300 K. We will refer to free-standing Cu

NP as FS-NP and Cu NP on graphene substrate as NP-on-C. All three directions of the simulation

box have periodic boundary conditions. Thirty angstrom thick vacuum layers are added above the

Cu NP and under the graphene substrate to make sure no Cu atom can interact with any atom of

surrounding simulation boxes. FS-NP has 30 Å thick vacuum layers in all directions.

Potential Parameters: For carbon-carbon interaction (C-C) of graphene substrate, AIREBO

Brenner/Stuart potential [38] is employed. A widely studied Mishin Embedded Atom Method (EAM)

potential [250] is used for copper-copper interaction (Cu-Cu). Lennard-Jones (LJ) potential is used

for carbon-copper interaction (C-Cu) with the potential parameters $\alpha = 3.0835$, $r_c = 7.5$ and three

different values of the potential well depth parameter ε. Huang et al used well depth parameter $\varepsilon =$

0.0117 eV for the simulation study of copper-graphene nanolayered composite [331]. In order to

understand the interaction between Cu and C atoms, we run the simulations using three different

NP-substate interaction strengths between Cu and C; ε values 0.0117, 0.0234 and 0.0351. In this

report, we will refer ε values of 0.0117, 0.0234 and 0.0351 as 1x, 2x and 3x, respectively. NPs-on-

C with Cu-C interaction strengths ε of 0.0117, 0.0234 and 0.0351 are referred to below as NP-on-

C-1x, NP-on-C-2x and NP-on-C-3x, respectively.

Before starting heating simulations, we run energy minimization to get the equilibrium

distance between Cu NP and graphene substrate. Then we heated up both FS-NP and NP-on-C

from 300 K to 1500 K, which is well above T_m of the Cu NP, as defined in the finite size NP by a

peak in the specific heat as a function of temperature (see Supplemental Information). The heating

rate was 1 K in 10 ps (i.e., 10^{11} K / s). Restart files are saved every 25 ps for constant temperature simulations. Depending on the temperature, simulations of relaxation at constant temperatures were run from 2 ns to 6 ns. We perform all relaxation simulations in a canonical (NVT) ensemble in this study.

5.3 Results and Discussion

5.3.1 Free-Standing Cu NP and Supported NP on a Planar Interacting Substrate

We started by investigating the effect of graphene substrate on the melting temperature (T_m) of Cu NP. The average potential energy (PE) of Cu atoms increases upon heating and this increase is abrupt during the melting of NP. [29] Note that we have only determined T_m upon heating (T_m^h). Therefore, any T_m mentioned in this report refers to T_m estimates upon heating (T_m^h), which is different from the T_m when solidifying upon cooling [332]. Figure S2 of Appendix B shows the change of PE over the approximate temperature (T); See SI for a discussion. The PE is calculated by taking an average of potential energies of all Cu atoms against time, where a rather sharp transition suggests a phase transition of the first order. It is evident that T_m of Cu FS-NP is close to 1250 K, but the PE gradient over T for supported Cu NP is less than the free-standing counterpart. To precisely determine T_m, we used the peak value of specific heat (C_p) derived from the slope of the PE vs. T curve. To determine the slope of the PE curve, we averaged PE over every 5 ps as shown in Figure S3 of Appendix B. We found T_m of Cu FS-NP is $\approx$ 1252 K and no change in T_m Cu NP when it is supported on graphene substrate with Cu-C interaction strength is 1x. However, a noticeable difference in T_m is found by doubling (2x) and tripling (3x) the Cu-C

interaction strength. For reference, T_m of Cu-on-C is $\approx$ 1232 K and $\approx$ 1222 K when Cu-C interaction strength is 2x and 3x, respectively. Ding et al. [314] found that T_m increases with an increase of the NP substrate interaction strength for Fe NPs, where the substrate was crystalline Fe. However, we find a decreasing T_m for Cu NP on our model graphene-inspired substrate when the interaction strength between Cu and the substrate is increased. Evidently, the sign of the shift of T_m depends on the nature of the interaction between the NP and the substrate.

Figure 5.1 shows the average potential energy of Cu atoms of FS-NP and NP-on-C-3x. At 500 K, the FS-NP and NP-on-C-3x NPs exhibit a similar shape where the NPs have well-defined facets. Above the Tammann temperature, however, where the interfacial mobility on the free surface starts to become appreciable, the facets on the NP surface start to disappear. The NPs on graphene adopt a rounder shape and become similar to a free-standing NP. An important structural change in the supported NPs is that the NP shape near an attractive substrate starts to become flattened for T exceeding near T_{TA}, and this flattening progressively grows to encompass a large part of the entire NP close to T_m where the NPs come to resemble liquid droplets in their shape. Above T_m, the NPs are generally non-spherical.
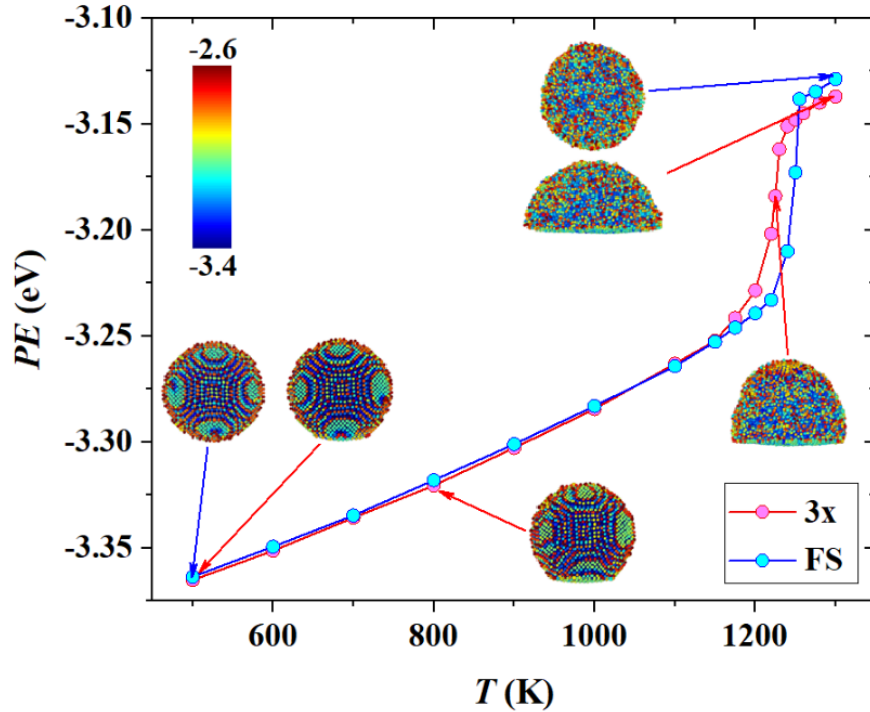
Figure 5.1: Average potential energy of the Cu atoms of free-standing Cu NP (FS-NP) and Cu NP on graphene with an enhanced (3x) interaction strength (NP-on-C-3x). At 500 K, both FS Cu NP and Cu NP on graphene have almost spherical shapes with facets. These facets are clearly visible without any significant change below the Tammann temperature (T_{TA}). There is a relatively small flat part on the Cu-C interface for NP-on-C-3x at $T < T_{TA}$. Above T_{TA}, FS-NP starts to get a spherical shape and facets start to disappear because of the initiation of surface pre-melting, as we have shown in our previous paper. [6] The flat Cu-C interface of graphene-supported Cu NP in this pre-melted regime also starts to become larger. After melting, the FS-NP becomes nearly spherical.

5.3.2 Definition of Interfacial and Core Regions of the NPs

For FS NP, we can define the free-surface layer and core regions of NP. The procedure of finding the surface thickness of FS NP is explained in detail in our previous work, [6] which is the same as the surface thickness calculation of thin films. [7] In addition to the free surface layer and core, we have Cu-C interface region for supported NP where Cu atoms are affected by C atoms of

the graphene substrate. Figure 5.2 shows the Cu NP supported on graphene substrate at 1200 K and different regions of NP. We will denote free surface and core by "S" and "C", respectively, and Cu-C interface by "int". We then designate the core of free-standing NP by the notation, FS-NP-C. Similarly, NP-on-C-3x-int designates the Cu-C interfacial region in which the interaction strength between Cu and C is tripled (3x).
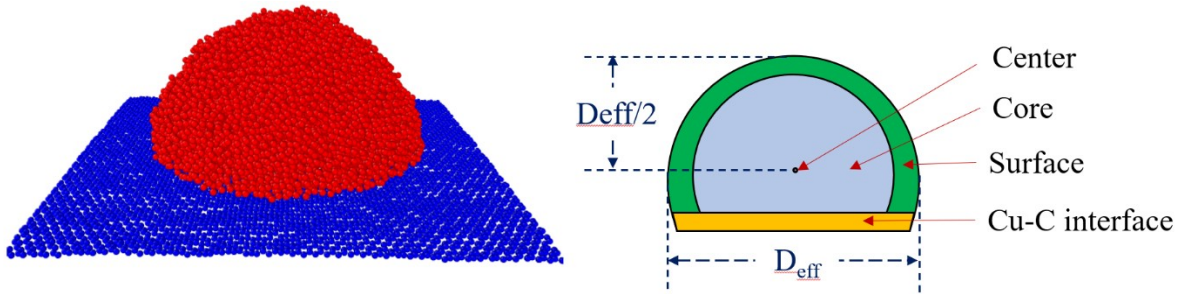
Figure 5.2: Supported Cu NP and effective center of supported NP. Cu NP on graphene substrate with 3x Cu-C interaction strength (Cu-on-C-3x) at 1200 K, which is close to T_m. The effective center of supported Cu NP can be obtained from the effective diameter (D_{eff}) as shown in this figure. This procedure of finding the NP "center" only applies if the center is inside the NP, which is the case for all Cu-C interaction strengths and the T range studied in the present work.

To define the effective thickness of the mobile interfacial layer of the Cu-C interfacial region near the supporting surface or the mobile interfacial region at the "free" NP surface, we determined the effective center of the supported NP as shown in Figure 5.2. Next, we determined "Debye-Waller factor" (DWF) or average $\langle u^2 \rangle$ of Cu atoms along with the radial distance from the effective center without considering the Cu atoms in the Cu-C interface. The free surface layer is considered where the average $\langle u^2 \rangle$ of Cu atoms is at least 5 % higher than the $\langle u^2 \rangle$ of Cu atoms at the core [6,7,49,76]. We describe the determination of $\langle u^2 \rangle$ in detail in our previous works. [6,7] Briefly, $\langle u^2 \rangle$ is defined by the average atomic displacement $\langle r^2 \rangle$ at a characteristic "caging time" or "fast beta

relaxation time" (τ_β)[107]. As in our previous works [6,7], we simply take the caging time to equal 2 ps in the present study. Thus, $\langle u^2 \rangle = \langle r^2(\tau_\beta = 2ps) \rangle = \frac{1}{N}\sum_{n=1}^{N}\{(x_2 - x_0)^2 + (y_2 - y_0)^2 + (z_2 - z_0)^2\}$, where, N is the number of atoms in the region of interest, (x_0, y_0, z_0) and (x_2, y_2, z_2) are the initial and final positions of the atoms after time $\tau_\beta = 2$ ps.

5.3.3 Tammann Temperature of Free-Standing and Substrate-Supported NPs

The Tammann temperature is the T at which the surface of the solid material first starts to become "mobile", which is often a necessary condition for chemical reactivity. As in our previous works, we can quantitatively estimate T_{TA}, from the intersection of the extrapolated lines of $\langle u^2 \rangle$ of surface and $\langle u^2 \rangle$ of core, a criterion that embodies the physical criterion that the interfacial region is more mobile than the interior of the material. Thus, we define the condition for T_{TA}: $\langle u^2(\text{surface}) \rangle = \langle u^2(\text{core}) \rangle$ at T_{TA}, which is normally well-below T_m. In particular, T_{TA} has often been reported to be in the range between 0.5 T_m and 0.67 T_m [83]. In our previous studies on free-standing NPs (FS-NP) [6] of different diameters, as well as free-standing thin films of different thicknesses [7], we found T_{TA} to be approximately 0.67 T_m. Similar to T_m, the T_{TA} of supported Cu NPs is reduced from the value of a FS-NP, as shown in Figure 5.3. In particular, we find that T_{TA} of FS-NP $\approx$ 785 K and T_{TA} of NP-on-C-3x NP $\approx$ 767 K. This type of shift in T_{TA} should translate into greater chemical reactivity at a lower temperature in many NP catalysis applications.
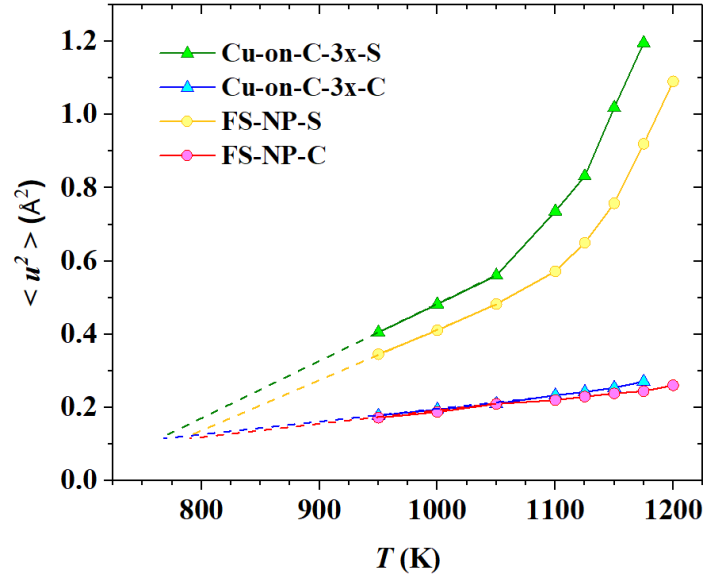
Figure 5.3: Tammann temperature from $\langle u^2 \rangle$ at the NP surface (S) and NP core (C). Debye-Waller factor or $\langle u^2 \rangle$ at the free surface (S) and NP core (C) regions of free-standing Cu NPs (FS-NP-S and FS-NP-C) and graphene supported Cu NPs with 3x interaction strength (NP-on-C-3x-S and NP-on-C-3x-C) as a function of temperature. Extrapolations, shown by dotted lines, from the linear parts of surface $\langle u^2(\text{surface}) \rangle$ and $\langle u^2(\text{core}) \rangle$ intersect near 785 K, which we take to define the Tammann temperature: $T_{TA} = 785$ K for a free-standing NP while $T_{TA} = 767$ K for a supported Cu NP on a substrate with 3x interaction strength.

Next, we took a closer look at values of $\langle u^2 \rangle$ in different regions of both free-standing and supported NPs. Figure 5.4 shows the $\langle u^2 \rangle$ of supported Cu NP with interaction strength 3x at the free surface, core and Cu-C interface, as well as $\langle u^2 \rangle$ for a free-standing Cu NP in its surface and core regions in the T range from near T_m. Surprisingly, $\langle u^2 \rangle$ near the Cu-C interface is higher than $\langle u^2 \rangle$ of both free surfaces of FS Cu NP and Cu NP on graphene with 3x interaction strength. The mobility of Cu atoms near the free surface and in the Cu-C interface is enhanced by the substrate. However, $\langle u^2 \rangle$ of the Cu-C interfacial region is lower than the free surfaces above T_m.
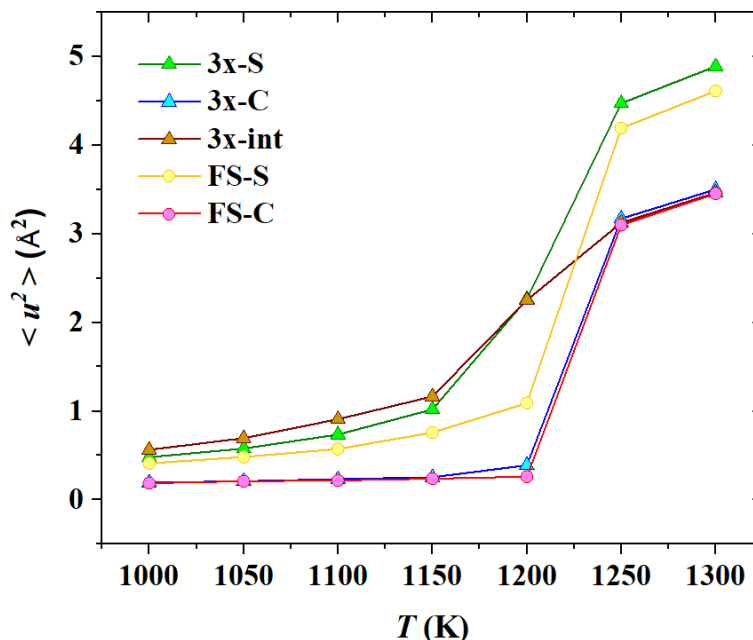
Figure 5.4: Debye-Waller parameter $\langle u^2 \rangle$ of Cu atoms near the free surface, NP core and Cu-C interfacial region of an NP-on-C substrate with 3x Cu-C strength and FS-NP at different T.

5.3.4 Mapping Spatial Fluctuations in $\langle u^2 \rangle$

In order to arrive at a clearer picture of atom mobilities at different regions of Cu NPs, we plotted $\langle u^2 \rangle$ maps. In Figure 5.5, we see the $\langle u^2 \rangle$ maps at the crystalline state of free-standing NP as well as NP on graphene with different Cu-C interaction strengths. Here the graphene substrate corresponds to the YZ-plane and the X-axis is perpendicular to the graphene substrate. Correspondingly, the vertical axis for Cu-on-C in Figure 5.5 is the distance (D) between Cu atoms and the graphene substrate along X-axis. For FS NP, we determined the baseline of the Cu atom having the lowest X coordinate value and the vertical axis is the distance between Cu atoms and the baseline. The horizontal axis (R) is defined as the distance between Cu atoms in YZ plane (plane parallel to the supporting substrate) to the center of the mass in the plane. The Cu atoms

near the free surface have higher mobility for FS NP as well as Cu-on-C NP. The Cu mobility near the Cu-C interface changes with changing interaction strength between Cu and C atoms.
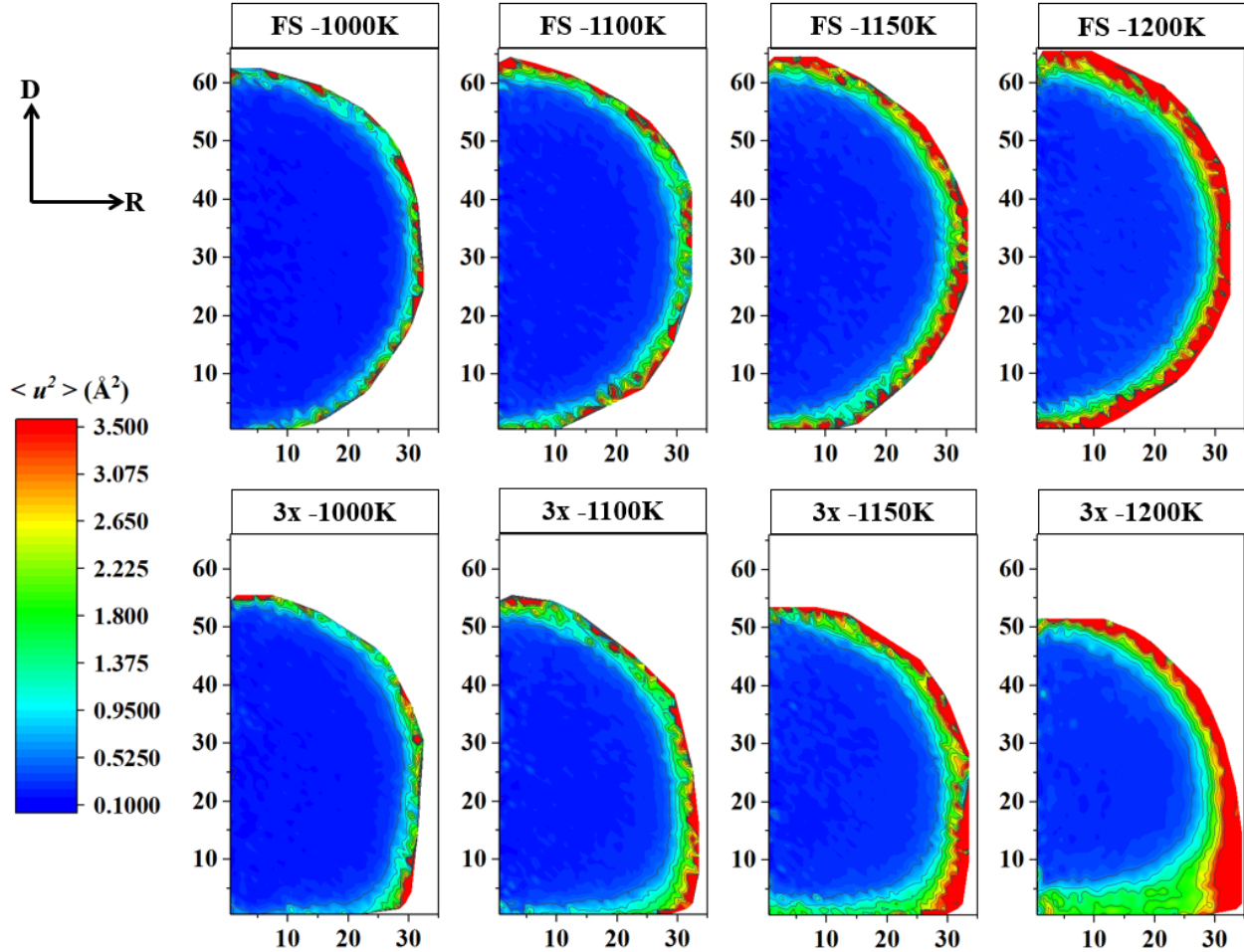
Figure 5.5: Mapping the gradients in $\langle u^2 \rangle$ in the interfacial region of the NP. The vertical axis represents the distance between the Cu atoms from the graphene substrate for Cu-on-C and the distance from the bottom-most Cu atom of FS NP. The horizontal axis represents the radial distance (R_{axis}) parallel to the substrate plane of Cu atoms from the axis of NPs.

In our previous studies [333], we suggested that $\langle u^2 \rangle$ can also be physically interpreted as a measure of local material "stiffness". In particular, we have shown that in both polymeric GF liquids [18] and metallic GF liquids [8], a linear scaling relationship between shear modulus G and k_B

$T / \langle u^2 \rangle$ could be established, and further, we showed the local elastic modulus and the local atomic stiffness showed a good correspondence in a metallic GF liquid [333]. In Figure 5.6 (top row), we show the local stiffness in the interfacial region of NP-on-C-3x at three different T, for comparison, we also show local stiffness fluctuation on the surface of a 60 Å Cu thin film at the same T (bottom row). The interfacial area increases upon the temperature in NP-on-C-3x due to the overall shape change, suggested in Figure 5.1. Compared with the thin film, the local stiffness fluctuation in NP-on-C-3x is highly non-homogeneous. Apparently, the furthest parts of the interfacial region, i.e., the contact line of the NP with the substrate, has lower effective stiffness, i.e., higher local mobility, and this lower stiffness region grows inwards as T approaches T_m, suggesting that the melting of the NP initiates near the "contact line" of NP with the substrate. It has recently become possible to measure such nanoscale stiffness fluctuations [334,335], although the measurements have so far been limited to metallic glass materials.
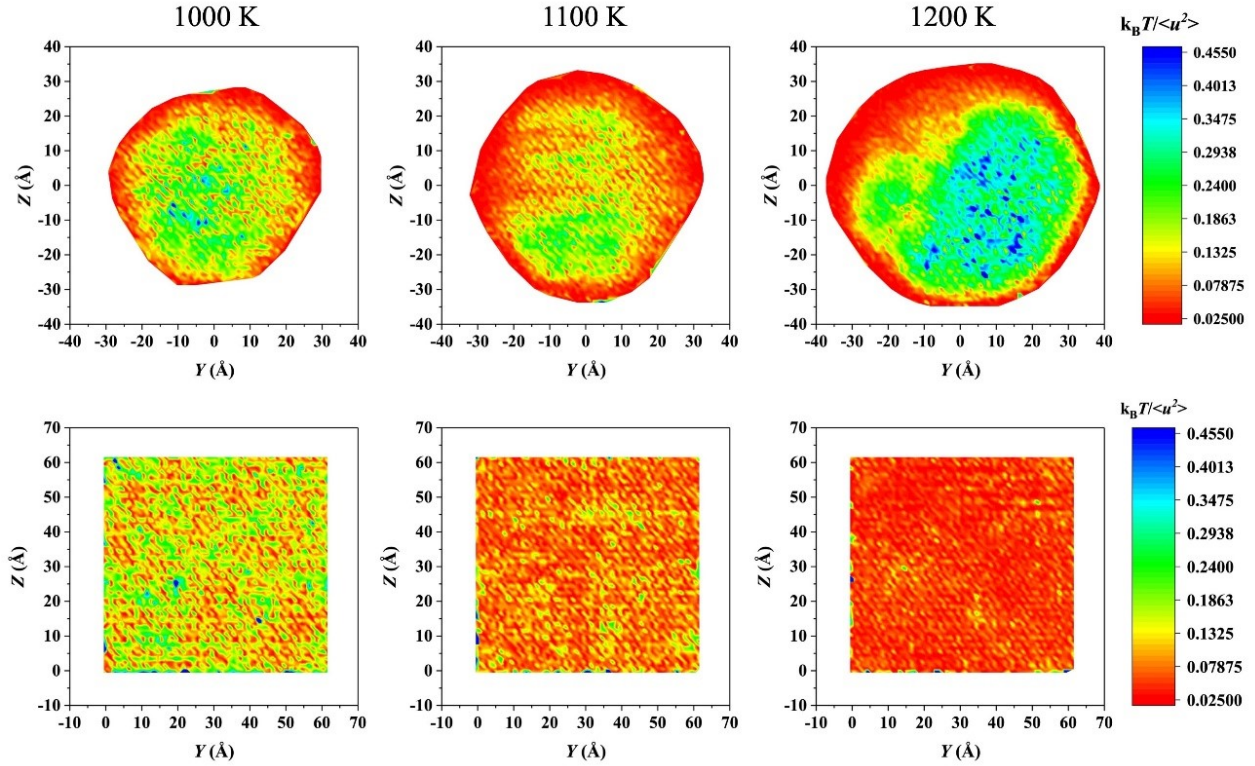
Figure 5.6: Local material stiffness, $k_B T / \langle u^2 \rangle$ of interfacial region in NP-on-C-3x (top row) and free surface in Cu thin (thickness $\approx$ 64 Å) films (bottom row) at three different T.

5.3.5 Probability Distribution Function $P(\langle u^2 \rangle)$ of Quake-Like Jumps in $\langle u^2 \rangle$

We next take a closer look at atomic motion in the interfacial region and examine how the interaction strength affects the interfacial dynamics of potential relevance to catalysis. In particular, we are interested in "erratic" jumps in either atomic position or potential energy. Figure 5.7a shows the "spectrum" of avalanche-like events for $\langle u^2 \rangle$ for representative mobile and immobile atoms in the interfacial region of NP-on-C-3x, and we quantify the intensity of these quake-like jumps in Figure 5.7a. In Figure 5.7b, we show the probability distribution function $P(\langle u^2 \rangle)$ of the intensity of these events, which follow a power-law form. It is stressed the NPs are in

an equilibrium state. Similar behavior has been observed and quantified previously in the interfacial dynamics of Ni NPs above their T_{TA} [52]. The scaling exponent γ, quantifying the quake intensity distribution, is obtained from fitting the magnitude of these events to a power-law, $P(\langle u^2 \rangle) \sim (\langle u^2 \rangle)^{-\gamma}$.

Figure 5.8 (a) shows the probability distribution function $P(\langle u^2 \rangle)$ of a FS Cu NP and supported Cu NP with tripled (3x) substrate interaction strength. As in our previous study of free Ni NPs, γ decreases with T in a nearly linear fashion, while we see here that γ decreases with an increase in the Cu-C interaction strength. The strength of the NP-substrate interaction modulates the distribution of the quake-like displacements in the NP interfacial region.
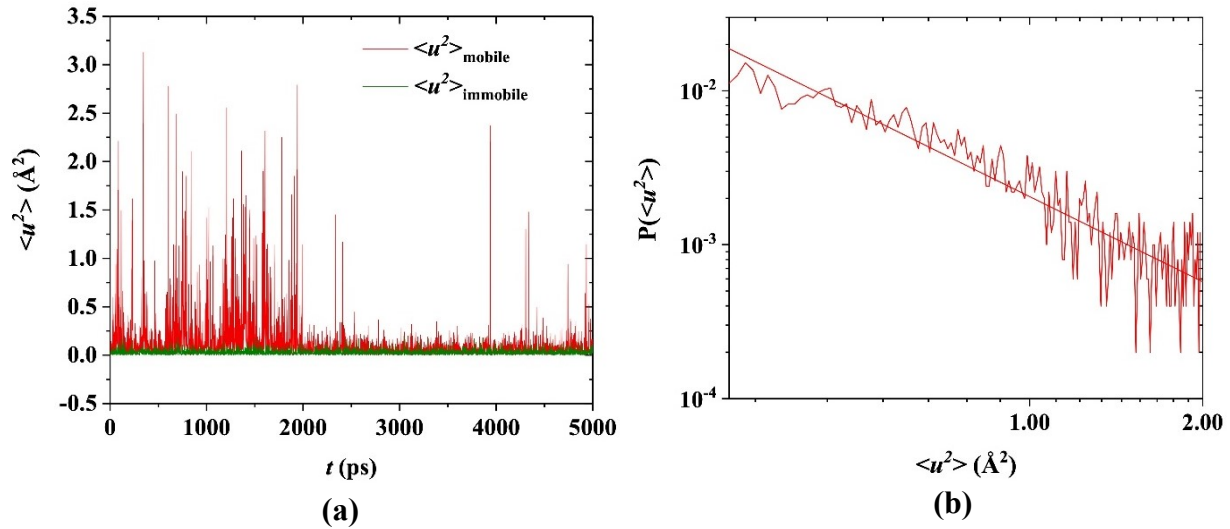
Figure 5.7: Quake-like jumps in atomic displacement in time and the distribution of their size distribution in magnitude. **(a)** The $\langle u^2 \rangle$ as a function of time for representative mobile and immobile atoms in the Cu-C interfacial region with a tripled (3x) interaction strength compared to graphene, where the mobile atom shows avalanche events, and **(b)** probability distribution of singular avalanche events, $P(\langle u^2 \rangle)$.
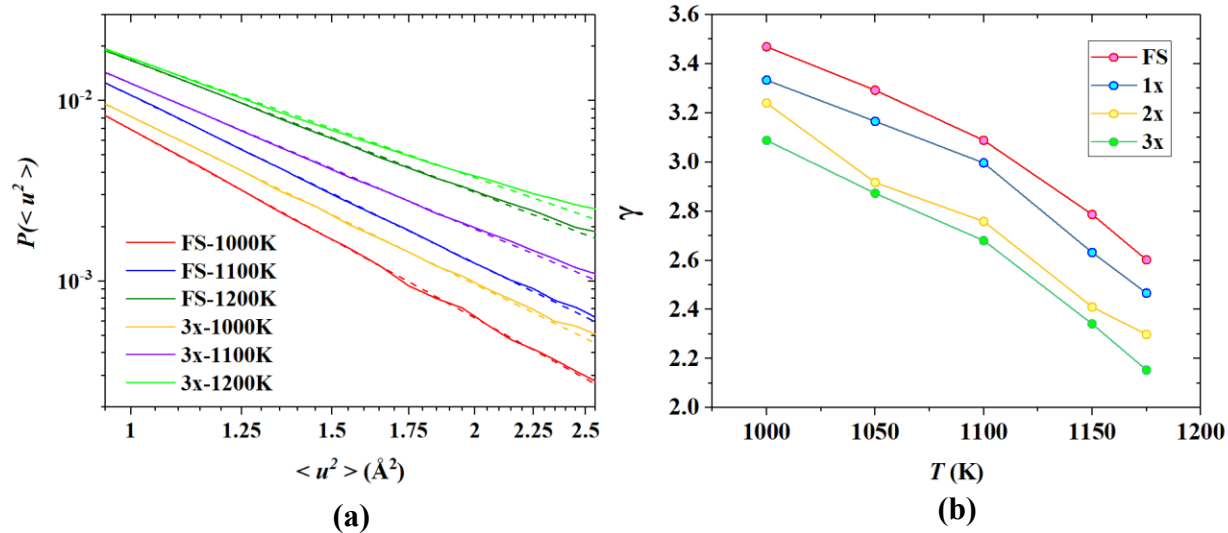
Figure 5.8: Probability distribution function P ($\langle u^2 \rangle$) of FS Cu NP and supported Cu NP with 3x interaction strengths (left) and the "quake scaling exponent" γ as a function of T.

In our previous study [52] of the interfacial dynamics in Ni NPs, we found that the potential energy fluctuations of atoms undergoing string-like collective motion showed well-defined fluctuations between two separated bands of potential energy. Here, we repeat this type of analysis to examine whether the same phenomenon exists when the substrate is present and how the interaction between NP with the substrate influences this striking phenomenon involving large local energy fluctuations on the NP surface. In Figure 5.9(a), we show the potential energy fluctuations and $\langle u^2 \rangle$ fluctuations of a mobile atom in the interfacial region of NP-on-C-3x and compare these fluctuations to an immobile "normal" in this region. In general, "normal" atoms, which are not participating in "erratic" jumps, fluctuate in a relatively regular fashion around an average value of $\langle u^2 \rangle$, while "mobile" atoms exhibit large fluctuations in potential energy (order of 1 eV) where there is a strong correlation between these telegraph signal-like changes in potential energy changes and spikes in displacement $\langle u^2 \rangle$ in the mobile atom positions. The inset of Figure 5.9(a) shows the potential energy of a mobile atom exhibits a bimodal distribution of potential

energy, suggesting the mobile atoms are jumping between two well-defined bands of potential energy states. This striking phenomenon was quantified in our previous work for free Ni NPs [52].

We next characterize these potential energy fluctuations by examining the average rate at which jumps occur between these bands of energy states. A successful jump was defined when a transition from the lower and upper energy state band (jump greater than $\Delta E > 0.3$ eV) occurs and a counter was assigned to each atom in the interfacial region to count the jumps. The inset of Figure 5.9(b) shows a near-linear relationship between jumps per atom and simulation time at all T, and the slopes of these lines provide a measure of the average jump rate. We further observe that the jump rate exhibits a near Arrhenius temperature dependence for all the different NP-substrate interaction strengths investigated, where the activation energy depends appreciably on the NP-substrate interaction strength. We again find evidence that the NP-substrate interaction modulates the NP dynamics in its interfacial region of the NPs.
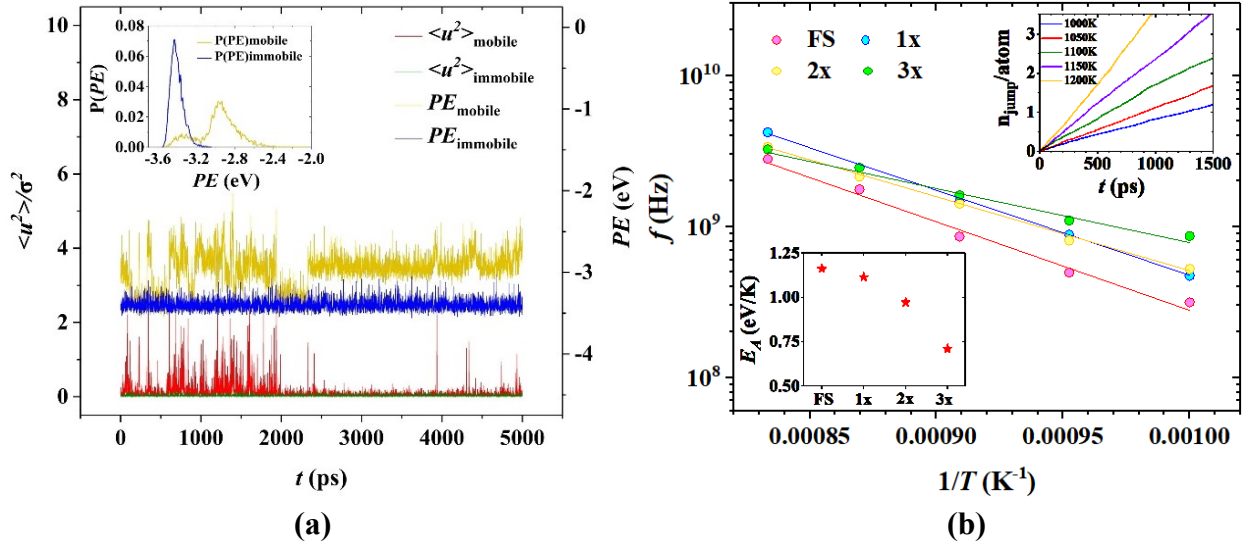
Figure 5.9: Potential energy fluctuations and the quantification of their average rate. **(a)** Potential energy and $\langle u^2 \rangle$ fluctuations of mobile and immobile atoms within the interfacial region of the NP-on-C-3x. Note the correlation between potential energy changes and the spikes in the local $\langle u^2 \rangle$ for the mobile atom. The inset shows a bimodal distribution of the potential energy of a mobile atom, suggesting the mobile atoms are jumping between two apparently well-defined bands of potential energy states. **(b)** The Arrhenius plot of jump rate in the interfacial region for different Cu-C interactions. A successful jump is defined as the increase of the potential energy of one atom larger than 0.3 eV. The inset on the top right corner shows that the successful jump per atom is a linear function of simulation time for all temperatures in the case of interface of NP-on-C-3x, where the slope is used to define jump rate. The inset at the left bottom corner shows the activation energy for the jump is sensitive to the Cu-C interaction, i.e., the higher interaction, the lower activation energy as a function of T.

5.3.6 Colored Noise in Particle Displacements and Potential Energy

The fluctuations in $\langle u^2 \rangle$ and the potential energy are not only correlated with each other in space, but also individually exhibit long-range correlations in the fluctuations in time which vary with T and the NP substrate interaction strength. We next quantify these fluctuations in mobility

128

and potential energy by looking at the power spectrum of the time series in these properties taken from our simulations where our development closely follows our previous work on free Ni NPs [52].

We first performed Fast Fourier Transformation (FFT) of the time series for $\langle u^2 \rangle$ and the potential energy as functions of time (t) to quantify the mobility and potential energy fluctuations of Cu atoms. Figure 5.10(a) shows the $\langle u^2 \rangle$ fluctuations of atoms in the interfacial region of the NP-on-C-3x in three different temperatures. A similar figure of the potential energy fluctuations is provided in the SI. In a standard fashion, we obtained noise exponents of $\langle u^2 \rangle$ and PE by fitting the amplitude curve as a function of frequency using the relation amplitude $\propto (1/f)^\alpha$ in the low-frequency regime. Figure 5.10(b) shows the representative amplitude vs. frequency at different temperatures supported Cu NP with 3x Cu-C interaction strength) and Figure 5.10(c) shows how the noise exponents of the $\langle u^2 \rangle$ fluctuations of FS-NP and the NP on different supporting substrates. We see that the T variation of the noise exponent associated with the mobility fluctuations is greatly reduced when the NP is supported on an attractive substrate. In our previous work, we found the T variation of this exponent was linked to the scale of collective atomic exchange motion in the interfacial region of crystalline materials, [50, 51] and in the internal dynamics of the protein ubiquitin (a model organic nanoparticle),[72] and we correspondingly anticipate the T dependence of the interfacial collective motion of the NPs to be relatively weak. We have confirmed this unexpected trend qualitatively in the supported Cu NPs, but we leave the quantification of this interesting effect to a future study.

We also observe in Figure 5.10(d) that the color of the noise for the potential energy fluctuations becomes redder, i.e., $\alpha_{PE,}$ becomes larger in magnitude, for an NP on a highly attractive substrate. Long-range correlations in mobility and potential are evidently modulated by varying the NP-substate interaction strength and temperature.
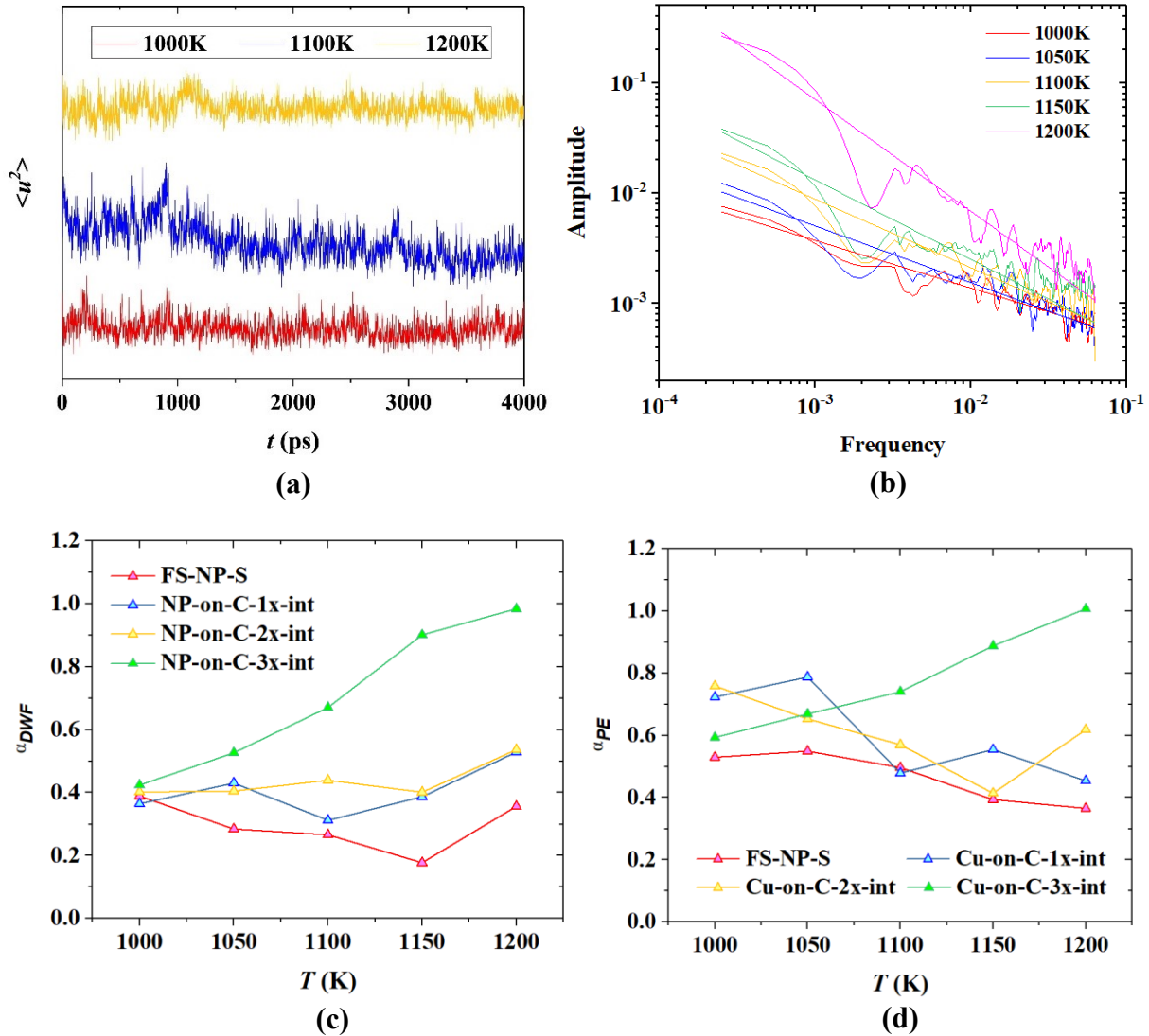
Figure 5.10: Noise exponents for potential energy and local mobility fluctuations. **(a)** DWF fluctuations of atoms in the interfacial region of the NP-on-C-3x as a function of simulation time at three temperatures. **(b)** Amplitude vs. Frequency from Fast Fourier Transform of fluctuation of $\langle u^2 \rangle$ vs t of NP-on-C-3x. **(c)** Noise exponent for mobility fluctuations, α_{DWF}. **(d)** Noise exponent for potential energy fluctuations, α_{PE}.

5.3.7 Diffusivity in the Nanoparticle Free Surface, Core and Solid Substate Regions

Next, we looked at the diffusivity of the atoms in different regions shown in Figure 5.2. We obtained diffusivity from the relations, $D = MSD/6t$ and $MSD = \frac{1}{N}\sum_{n=1}^{N}\{(x_t - x_0)^2 + (y_t - y_0)^2 + (z_t - z_0)^2\}$, where, N is the number of atoms in region of the interest, (x_0, y_0, z_0) and (x_t, y_t, z_t) are the initial positions and final positions of atoms after time t. Figure 5.11 shows D against T at surface and Cu-C interface of supported NPs with different interaction strengths as well as surface and core of free-standing NP. We have seen upward curvatures of Arrhenius plots of D for surfaces of metallic glass films and metallic glass NPs in our previous works [6,7]. We found very small or no curvature of Arrhenius plot of D for free surfaces of crystal NPs depending on their sizes [6]. In the present study, we found upward curvature before melting for interfaces as well as free surfaces of supported NPs. Note that we are studying relatively larger size NP and the effective diameter of supported NP is even larger than the free-standing NP of the same number of atoms.
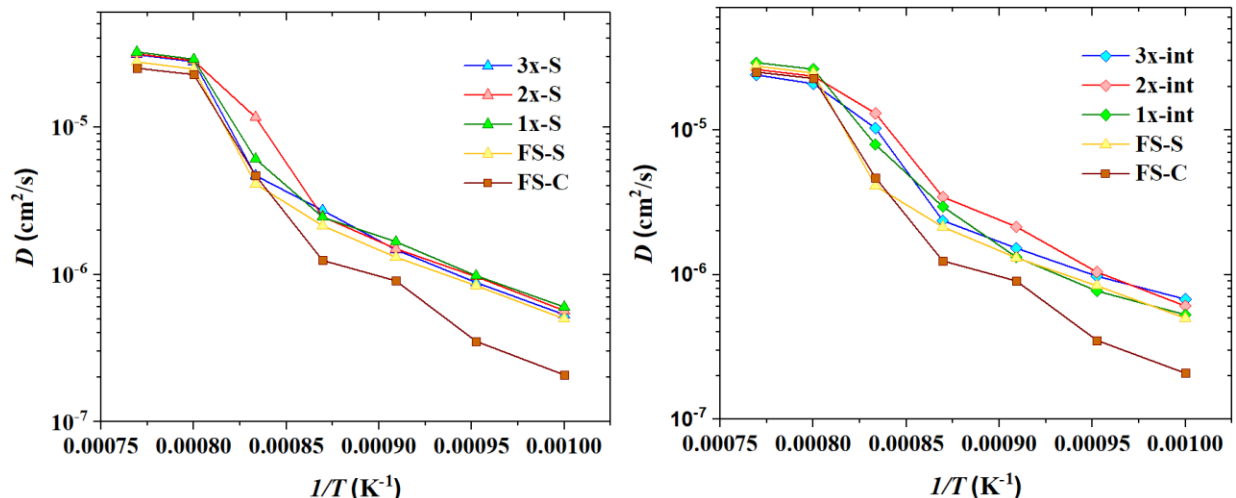
Figure 5.11: Arrhenius plots of the diffusion coefficient (D) of the Cu atoms in the free interfacial region and the Cu-C interfacial region for substates having different Cu-C strengths and for free-standing NPs for comparison.

5.3.8 Localization Model Estimates of the Structural Relaxation Time and Diffusion Coefficient in the NP Interfacial Regions

The structural relaxation time τ_α and diffusion coefficient D of the interfacial atoms are clearly of central importance in understanding NP catalysis, and it is of evident importance to quantify changes in "mobility" in the NP interfacial region, as defined by these long-time transport properties. In previous work, we have found that local values of $\langle u^2 \rangle$ values can be used to estimate gradients in these properties based on the localization model, [6,7] and we again closely follow this previous work on thin metallic films and nanoparticles (both crystalline and metallic glass metallic materials) to determine if this model applies to the more complex case of a metal NP supported on model interacting substrates.

We define the relaxation time from the self-intermediate scattering function (SISF), $F_s(q,t) = \langle exp[-iq\{r_i(t) - r_0(t)\}]\rangle$. In particular, $F_s(q^*,t)$ data as function of t is fitted to the relation $F_s(q,t) \propto exp[(t/\tau_\alpha)^{\beta_S}]$ with q^* corresponding to the peak position of the static structure factor to yield the relaxation time (τ_α) and β, is described in numerous previous works. [6–8,14,28] The diffusion coefficient D is defined by the standard relation mentioned above.

In our previous studies on thin film and nanoparticles with crystalline and amorphous structures, we found that relaxation time (τ_α) and diffusivity (D) can be predicted from $\langle u^2 \rangle$ in a range of temperatures using Localization Model (LM) [6–8,28]. In particular, the LM predict τ_α to follow the non-trivial relationship, $\tau_\alpha(T) = \tau_\alpha(T_A)exp[\{\langle u^2(T_A)\rangle/\langle u^2(T)\rangle\}^{3/2} - 1]$ [8] and the D can be predicted from the relation: $ln[\{D(T)/T\}/\{D(T_A)/T_A\}] = (1 - \zeta) [\{\langle u^2(T_A)\rangle/\langle u^2(T)\rangle\}^{3/2} - 1]$, [8] where ζ is a "decoupling exponent" obtained from fractional Stokes–Einstein" (FSE) relation, $D / T \propto (\tau_\alpha)^{1-\zeta}$.[9] The decoupling exponent is not theoretically well-understood at the moment, which limits the predictability of D based on the LM. Douglas and Leporini [19] have argued that breakdown of the Stokes-Einstein relation arises from long-lived immobile regions in the material in comparison for the time required for diffusion to become established.

This physical model offers some physical insight into the exponent based on established hydrodynamic results for fluids in heterogeneous fluids. In particular, Douglas and Leporini assume that the idealized spherical heterogeneities of glass-forming liquids all have the same size and the applicability of hydrodynamics to these heterogeneous materials. This model predicts ζ = 0.4 for the case when the dynamic heterogeneities have high dynamical contrast with the surrounding matrix, but an obvious extension of the model which treats the dynamic heterogeneities as being like droplets having a "fluidity" different than the surrounding matrix leads to a vanishing ζ when the mobility contrast is low. In this model, ζ primarily derives from

the dynamic contrast between the long-lived dynamic heterogeneities in glass-forming liquids and our images of the interfacial region of our surface-melted NPs indicate that the interfacial region of these NPs in their "pre-melted" state is likewise heterogeneous in its dynamics, even though it is not clear that the interfacial layer can be characterized as being "liquid-like" because of residual ordering apparent when averaging over long timescales. At any rate, we calculated D and τ_α at different regions of FS-NP and Cu-on-C model substrates having different interaction strengths with the NP. Evidently, the data in Figure 5.12 shows the localization model can reasonably predict τ_α and D can be estimated from $\langle u^2 \rangle$ in all NP regions and conditions simulated by taking ζ to be in the range, $\zeta = 0.33$ to 0.59.
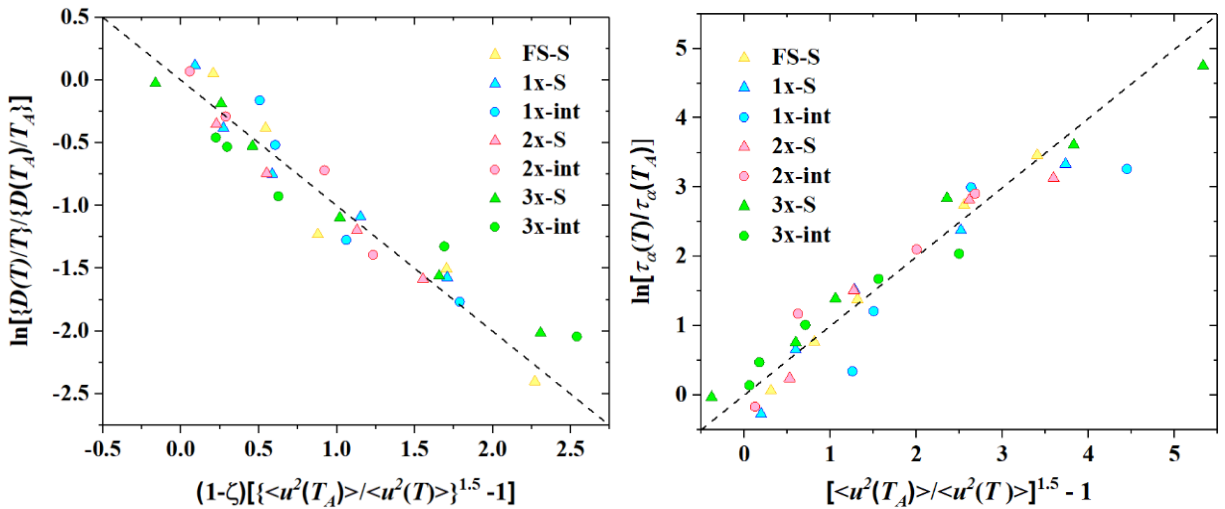
Figure 5.12: Test of the Localization Model prediction of the relaxation times (τ_α) and Cu diffusion coefficient (D) from $\langle u^2 \rangle$ for free-standing Cu NP and Cu NP supported on graphene with different interaction strengths with the Cu NP. We tested the applicability of the localization model for free surface of FS-NP and Cu-on-C as well as Cu-C interface regions of Cu-on-C NPs, where ζ is in the range, $\zeta = 0.33$ to 0.59.

5.4 Conclusions

The catalytical behavior has often been observed to depend strongly on the supporting substrate on which the NPs are loaded, suggesting that the substrate plays a more active role in the catalysis than just inhibiting the coalescence of the nanoparticles and optimizing the rate of diffusion-limited reactions by keeping the nanoparticles as separated as possible to increase the extent of the reaction. With a view that the substrate might be inducing appreciable changes in the dynamics in the nanoparticles of relevance to understanding the observed changes in reactivity, we simulated model metal (Cu) nanoparticles having a "typical" size ≈ 6 nm on a supporting substrate. Although or substrate was initially inspired by graphene substrates sometimes employed in applications, we later realized that the interfacial energy between this nanoparticle particle and graphene was rather weak and we then considered model substrates in which the strength of the NP substate interaction was multiplied by constant factors. Physically, this increased interaction strength could occur through the oxidation of the graphene exposed to the air at elevated temperatures or by choosing an oxide substrate of the kind often used in industrially relevant catalysis processes. Our artificial tuning of the nanoparticle surface interaction was intended to determine how the qualitative effect of the nanoparticle interfacial dynamics was altered by the boundary interaction without trying to model the complex chemistry of the real catalytic material.

We find that increasing the interaction strength of the nanoparticle with the substrate causes a loss of nanoparticle "stability", in the sense that both the melting temperature and the Tammann temperature are shifted downward. Since the Tammann temperature is generally appreciated as a critical parameter governing the catalytic activity of metal catalysts [83] in real catalytic reactions we focused on the physical mechanism by which the substrate influences this characteristic

temperature. Further, since fluctuations in the local particle mobility is plausibly significant for the local rates of catalytic reaction, we also investigated these fluctuations and found that they were likewise strongly modulated by varying the interaction strength between the NP and the substrate. We also found a large change in the activation energy of large fluctuations of the local potential energy in localized regions of the surface by varying the nanoparticle-substrate interaction strength, a phenomenon of obvious potential interest in understanding the enhancement of catalytic reactions by metal nanoparticles. Finally, we showed that we can estimate changes in the atomic diffusion coefficient and relaxation times in the interfacial regions of the nanoparticles through a consideration of local fluctuations of atomic position on a ps timescale. The importance of interfacial mobility is broadly appreciated in nanoparticle catalysis. There are evidently appreciable changes in the dynamics of nanoparticles that arise from their interaction with a substrate, and we may expect these changes will have a significant impact on the rate and selectivity of NP-based catalysis reactions. In future work, we will need to study the reaction process as well as the NP dynamics to fully understand how the nanoparticle dynamics and the reaction dynamics are coupled to give rise to the unique catalytic properties of metal nanoparticles and by extension their organic nanoparticle counterparts, enzymes.

Chapter 6: Conclusion

6.1 Summary of Conclusions

Localization model (LM) is potentially very useful for developing nanostructures. We found that this remarkable model can be used to predict very important long time dynamic parameter of glass formation, α-relaxation time from short time dynamic parameter Debye-Waller Factor (DWF) without any free parameter. LM can also be used to predict another important slow dynamic parameter, diffusion coefficient from DWF when diffusivity is related to α-relaxation time using decoupling exponent obtained from Fractional Stokes–Einstein (FSE) relation. We successfully tested localization model over wide range of temperature for –

- Free-standing $Cu_{64}Zr_{36}$ metallic glass thin films (MGTF) with thicknesses ranging from 10Å to 60Å.

- Interfaces of free-standing $Cu_{64}Zr_{36}$ MGTFs where atoms have higher mobility compared to the atoms of bulk $Cu_{64}Zr_{36}$ MG.

- Cores, if significantly exists, of free-standing $Cu_{64}Zr_{36}$ MGTFs where atoms have almost same mobility compared to the atoms of bulk $Cu_{64}Zr_{36}$ MG.

- Interfaces of free-standing 60Å thick Cu thin films (Cu-TF) with (100), (110) and (111) crystallographic orientation of free surface.

- Free-standing $Cu_{64}Zr_{36}$ metallic glass nanoparticles (MGNP) with diameters ranging from 20Å to 60Å.

- Interfaces and cores of free-standing $Cu_{64}Zr_{36}$ MGNPs.

- Interfaces of free-standing Cu nanoparticles (Cu-NP) with diameters ranging from 20Å to 60Å.

- Cu-NP with 10,000 atoms supported on interactive graphene substrate with three different interaction strengths between Cu atoms of NP and C atoms of substrate – 0.0117eV, 0.0234eV and 0.0351eV.

- Interfacial region of supported Cu-NPs exposed to vacuum and Cu-C interface, where Cu atoms of NP are directly affected by the C atoms of the substrate.

We also compared the dynamics of free interfaces of free-standing $Cu_{64}Zr_{36}$ MGTFs with different thicknesses and free-standing $Cu_{64}Zr_{36}$ MGNPs with different diameters with bulk $Cu_{64}Zr_{36}$ MG. To explore the science behind the catalytic properties of nanoparticles which often are supported on an interacting substrate, we also performed a comparative study of dynamics of Cu NPs supported on interacting graphene substrate. To understand the effects of graphene substrate, we also compared the dynamics of free interface of supported NP exposed to the vacuum, Cu-C interface, bulk-like core of Cu-NP, and free interface of free-standing Cu-NP of the same size. Finally, we compared the overall dynamics of supported Cu-NP and free-standing Cu-NP to understand the catalytic properties of NP. We found overall enhanced mobility of atoms with the presence of interactive substrate. Melting temperature, as well as Tammann temperature where the enhanced mobility of interface first immerges, of NP becomes lower with the presence of interacting substrate.

Moreover, we confirmed that Tammann temperature of crystalline materials and glass-transition temperature of amorphous materials can be precisely determined from the intersection of extrapolated curves of interface and core DWF plots at lower temperature where DWF varies linearly with temperature. We estimated Tammann temperature and glass-transition temperature

of free-standing $Cu_{64}Zr_{36}$ MGTFs, $Cu_{64}Zr_{36}$ MGNPs, Cu-TF, and Cu-NPs as well as supported Cu-NPs.

6.2 Recommended Future Works

1. So far, we have only studied the interfacial dynamics of free-standing thin films and nanoparticles, and supported nanoparticles in the perfect vacuum. In the real-life situation, free interface is rarely exposed to perfect vacuum. In addition, glass-forming properties affected by pressure. Therefore, more work is needed to understand the interfacial dynamics when interface exposed to gas or liquid under

2. We have performed comparative study on dynamics of free interface and Cu-C interface of Cu-NP supported on interacting supporting graphene substrate, free interface of free-standing Cu-NP, and core of Cu-NP (bulk Cu). The Cu-C interface where the dynamics of Cu atoms are directly affected by the C atoms of the substrate. In this Cu-C interface, we have two parts – (a) part where Cu atoms are only affected by the C atoms of the substrate and (b) the part where Cu atoms are close to both substrate and free surface. In order to get a clear idea how Cu atoms are affected by the C atoms of the substrate, we need to study Cu atoms that are only affected by the substrate. Thus, we should perform crystalline Cu thin films supported one side on graphene substrate and another side exposed to vacuum. Moreover, we need to compare three different crystallographic orientations, (100), (110) and (111), of free surface and Cu-C interface of Cu thin films as we have done for free-standing crystalline Cu thin films.

3.   In this study, we have studied single thin film and nanoparticles. In future, we also should know how interfacial dynamics of interacting more than one thin films and/or nanoparticles both free-standing and supported conditions.

4.   We have studied the dynamics of free-standing $Cu_{64}Zr_{36}$ metallic glass thin films and nanoparticles. We should continue research on supported metallic glass thin films and nanoparticles.

5.   To understand the effect of interacting substrate, we can also enclave the nanoparticles inside nanotube or fullerenes in addition to only a substrate below the nanopartilcle.

6.   Graphene layers are also formed on nanoparticles supported on other supportive materials for biological applications. Therefore, it is worth exploring the case where nanoparticle is supported on an interactive substrate and also covered its domed-shape size by graphene.

7.   Voronoi volume believed to be the possible measure of free volume. Moreover, relaxation time and Voronoi volume is also correlated, although there is not enough scientific study to confirm that. Relation between free volume and Voronoi volume is also not confirmed yet. [24] It is worth conducting extensive study on this relationship; which is another future research. Ultimately, finding relationship between Voronoi volume, free volume, DWF and relaxation time will be an interesting continuation of this study.

References

1. Dudowicz J, Freed K F, D. J. F. Generalized Entropy Theory of Polymer Glass Formation. *Adv. Chem. Phys.* **137**, 125 (2008).

2. Martinez, L.-M. & Angell, C. A. A thermodynamic connection to the fragility of glass-forming liquids. *Nature* **410**, 663–667 (2001).

3. Zanotto, E. D. & Mauro, J. C. The glassy state of matter: Its definition and ultimate fate. *J. Non. Cryst. Solids* **471**, 490–495 (2017).

4. Larini, L., Ottochian, A., De Michele, C. & Leporini, D. Universal scaling between structural relaxation and vibrational dynamics in glass-forming liquids and polymers. *Nat. Phys.* **4**, 42–45 (2008).

5. Lancelotti, R. F., Cassar, D. R., Nalin, M., Peitl, O. & Zanotto, E. D. Is the structural relaxation of glasses controlled by equilibrium shear viscosity? *J. Am. Ceram. Soc.* **104**, 2066–2076 (2021).

6. Mahmud, G., Zhang, H. & Douglas, J. F. Localization model description of the interfacial dynamics of crystalline Cu and $Cu_{64}Zr_{36}$ metallic glass nanoparticles. *Eur. Phys. J. E* **44**, 33 (2021).

7. Mahmud, G., Zhang, H. & Douglas, J. F. Localization model description of the interfacial dynamics of crystalline Cu and $Cu_{64}Zr_{36}$ metallic glass films. *J. Chem. Phys.* **153**, 124508 (2020).

8. Douglas, J. F., Betancourt, B. A. P., Tong, X. & Zhang, H. Localization model description of diffusion and structural relaxation in glass-forming Cu-Zr alloys. *J. Stat. Mech. Theory Exp.* **2016**, 54048 (2016).

9. Zhang, H., Wang, X. & Douglas, J. F. Localization model description of diffusion and structural relaxation in superionic crystalline UO_2. *J. Chem. Phys.* **151**, 071101 (2019).

10. Khonik, V. Understanding of the Structural Relaxation of Metallic Glasses within the Framework of the Interstitialcy Theory. *Metals (Basel).* **5**, 504–529 (2015).

11. SCHUH, C., HUFNAGEL, T. & RAMAMURTY, U. Mechanical behavior of amorphous alloys. *Acta Mater.* **55**, 4067–4109 (2007).

12. Binder, K. & Kob, W. *Glassy Materials and Disordered Solids*. (WORLD SCIENTIFIC, 2011). doi:10.1142/7300.

13. Donati, C. *et al.* Stringlike Cooperative Motion in a Supercooled Liquid. *Phys. Rev. Lett.* **80**, 2338–2341 (1998).

14. Zhang, H. *et al.* Role of string-like collective atomic motion on diffusion and structural relaxation in glass forming Cu-Zr alloys. *J. Chem. Phys.* **142**, 164506 (2015).

15. Kauzmann, W. The Nature of the Glassy State and the Behavior of Liquids at Low Temperatures. *Chem. Rev.* **43**, 219–256 (1948).

16. Adam, G. & Gibbs, J. H. On the Temperature Dependence of Cooperative Relaxation Properties in Glass-Forming Liquids. *J. Chem. Phys.* **43**, 139–146 (1965).

17. Buchenau, U. & Zorn, R. A Relation Between Fast and Slow Motions in Glassy and Liquid Selenium. *Europhys. Lett.* **18**, 523–528 (1992).

18. Pazmiño Betancourt, B. A., Hanakata, P. Z., Starr, F. W. & Douglas, J. F. Quantitative relations between cooperative motion, emergent elasticity, and free volume in model glass-forming polymer materials. *Proc. Natl. Acad. Sci. U. S. A.* **112**, 2966–2971 (2015).

19. Douglas, J. . & Leporini, D. Obstruction model of the fractional Stokes–Einstein relation in glass-forming liquids. *J. Non. Cryst. Solids* **235**–**237**, 137–141 (1998).

20. Hall, R. W. & Wolynes, P. G. The aperiodic crystal picture and free energy barriers in glasses. *J. Chem. Phys.* **86**, 2943–2948 (1987).

21. Angell, C. . Relaxation in liquids, polymers and plastic crystals — strong/fragile patterns and problems. *J. Non. Cryst. Solids* **131**–**133**, 13–31 (1991).

22. Angell, C. A. Formation of Glasses from Liquids and Biopolymers. *Science (80-.).* **267**, 1924–1935 (1995).

23. Pederson, U. R. & Schrøder, T. B. *Long-time simulations of viscous liquids from strong correlations to crystallization*. PhD thesis, Danish National Research Foundation Centre "Glass and Time", IMFUFA, Department of Science, Systems and Models, Roskilde University, Denmark (2009).

24. Starr, F. W., Sastry, S., Douglas, J. F. & Glotzer, S. C. What Do We Learn from the Local Geometry of Glass-Forming Liquids? *Phys. Rev. Lett.* **89**, 125501 (2002).

25. David S. Simmons, Marcus T. Cicerone, Qin Zhong, Madhusudan Tyagic, J. F. D. Generalized localization model of relaxation in glass-forming liquids. *Soft Matter* **8**, 11455–11461 (2012).

26. Ottochian, A. & Leporini, D. Universal scaling between structural relaxation and caged dynamics in glass-forming systems: Free volume and time scales. *J. Non. Cryst. Solids* **357**, 298–301 (2011).

27. Turnbull, D. & Cohen, M. H. Free-Volume Model of the Amorphous Phase: Glass Transition. *J. Chem. Phys.* **34**, 120–125 (1961).

28. Zhang, H., Wang, X., Chremos, A. & Douglas, J. F. Superionic UO 2 : A model anharmonic crystalline material. *J. Chem. Phys.* **150**, 174506 (2019).

29. Zhang, H., Kalvapalle, P. & Douglas, J. F. String-like collective atomic motion in the interfacial dynamics of nanoparticles. *Soft Matter* **6**, 5944 (2010).

30. Zhang, W. B. *et al.* Size effect on atomic structure in low-dimensional Cu-Zr amorphous systems. *Sci. Rep.* **7**, 7291 (2017).

31. Moulijn, J. ., van Diepen, A. . & Kapteijn, F. Catalyst deactivation: is it predictable? *Appl. Catal. A Gen.* **212**, 3–16 (2001).

32.   Plimpton, S. Fast Parallel Algorithms for Short-Range Molecular Dynamics. *J. Comput. Phys.* **117**, 1–19 (1995).

33.   Jones, J. E. On the determination of molecular fields.—I. From the variation of the viscosity of a gas with temperature. *Proc. R. Soc. London. Ser. A, Contain. Pap. a Math. Phys. Character* **106**, 441–462 (1924).

34.   Jones, J. E. On the determination of molecular fields. —II. From the equation of state of a gas. *Proc. R. Soc. London. Ser. A, Contain. Pap. a Math. Phys. Character* **106**, 463–477 (1924).

35.   Lennard-Jones, J. E. Cohesion. *Proc. Phys. Soc.* **43**, 461–482 (1931).

36.   Daw, M. S. & Baskes, M. I. Embedded-atom method: Derivation and application to impurities, surfaces, and other defects in metals. *Phys. Rev. B* **29**, 6443–6453 (1984).

37.   Daw, M. S., Foiles, S. M. & Baskes, M. I. The embedded-atom method: a review of theory and applications. *Mater. Sci. Reports* **9**, 251–310 (1993).

38.   Stuart, S. J., Tutein, A. B. & Harrison, J. A. A reactive potential for hydrocarbons with intermolecular interactions. *J. Chem. Phys.* **112**, 6472–6486 (2000).

39.   Verlet, L. Computer 'Experiments' on Classical Fluids. I. Thermodynamical Properties of Lennard-Jones Molecules. *Phys. Rev.* **159**, 98–103 (1967).

40.   Nosé, S. A unified formulation of the constant temperature molecular dynamics methods. *J. Chem. Phys.* **81**, 511–519 (1984).

41.   Hoover, W. G. Canonical dynamics: Equilibrium phase-space distributions. *Phys. Rev. A* **31**, 1695–1697 (1985).

42.   Parrinello, M. & Rahman, A. Polymorphic transitions in single crystals: A new molecular dynamics method. *J. Appl. Phys.* **52**, 7182–7190 (1981).

43.   Wang, X. *et al.* Sample size effects on strength and deformation mechanism of Sc75Fe25 nanoglass and metallic glass. *Scr. Mater.* **116**, 95–99 (2016).

44.   Zhong, C. *et al.* The size-dependent non-localized deformation in a metallic alloy. *Scr. Mater.* **101**, 48–51 (2015).

45.   Zhong, C. *et al.* On the critical thickness for non-localized to localized plastic flow transition in metallic glasses: A molecular dynamics study. *Scr. Mater.* **114**, 93–97 (2016).

46.   Li, Q.-K. & Li, M. Surface structure and properties of NiZr model metallic glasses: A molecular dynamics simulation. *J. Non. Cryst. Solids* **354**, 2060–2065 (2008).

47.   Böddeker, B. & Teichler, H. Dynamics near free surfaces of molecular dynamics simulated Ni0.5Zr0.5 metallic glass films. *Phys. Rev. E* **59**, 1948–1956 (1999).

48.   Dong, T. Q., Hoang, V. V. & Lauriat, G. Molecular simulation of freestanding amorphous nickel thin films. *Thin Solid Films* **545**, 584–591 (2013).

49.   Zhang, H., Yang, Y. & Douglas, J. F. Influence of string-like cooperative atomic motion on surface diffusion in the (110) interfacial region of crystalline Ni. *J. Chem. Phys.* **142**,

084704 (2015).

50. Zhang, H., Khalkhali, M., Liu, Q. & Douglas, J. F. String-like cooperative motion in homogeneous melting. *J. Chem. Phys.* **138**, 12A538 (2013).

51. Zhang, H. & Douglas, J. F. Glassy interfacial dynamics of Ni nanoparticles: part I Colored noise, dynamic heterogeneity and collective atomic motion. *Soft Matter* **9**, 1254–1265 (2013).

52. Zhang, H. & Douglas, J. F. Glassy interfacial dynamics of Ni nanoparticles: Part II Discrete breathers as an explanation of two-level energy fluctuations. *Soft Matter* **9**, 1266–1280 (2013).

53. Suni, I. I. & Seebauer, E. G. Surface self diffusion at high temperatures: new simulational insights. *Thin Solid Films* **272**, 229–234 (1996).

54. Ediger, M. D. & Forrest, J. A. Dynamics near Free Surfaces and the Glass Transition in Thin Polymer Films: A View to the Future. *Macromolecules* **47**, 471–478 (2014).

55. Yu, L. Surface mobility of molecular glasses and its importance in physical stability. *Adv. Drug Deliv. Rev.* **100**, 3–9 (2016).

56. Garcia-Barriocanal, J. *et al.* Colossal Ionic Conductivity at Interfaces of Epitaxial ZrO2:Y2O3/SrTiO3 Heterostructures. *Science (80-.).* **321**, 676–680 (2008).

57. Knoner, G., Reimann, K., Rower, R., Sodervall, U. & Schaefer, H.-E. Enhanced oxygen diffusivity in interfaces of nanocrystalline ZrO2*Y2O3. *Proc. Natl. Acad. Sci.* **100**, 3870–3873 (2003).

58. Ma, J. *et al.* Fast surface dynamics enabled cold joining of metallic glasses. *Sci. Adv.* **5**, eaax7256 (2019).

59. Allen, R. E., De Wette, F. W. & Rahman, A. Calculation of Dynamical Surface Properties of Noble-Gas Crystals. II. Molecular Dynamics. *Phys. Rev.* **179**, 887–891 (1969).

60. Allen, R. E. & De Wette, F. W. Calculation of Dynamical Surface Properties of Noble-Gas Crystals. I. The Quasiharmonic Approximation. *Phys. Rev.* **179**, 873–886 (1969).

61. Allen, R. E. & De Wette, F. W. Mean-Square Amplitudes of Vibration at a Surface. *Phys. Rev.* **188**, 1320–1323 (1969).

62. Yang, Y., Zhang, H. & Douglas, J. F. Origin and Nature of Spontaneous Shape Fluctuations in "Small" Nanoparticles. *ACS Nano* **8**, 7465–7477 (2014).

63. F.A. Lindemann. The Calculation of Molecular Vibration Frequencies. *Zeitschrift für Phys.* **11**, 609–612 (1910).

64. Gilvarry, J. J. The Lindemann and Grüneisen Laws. *Phys. Rev.* **102**, 308 (1956).

65. H.Bilgram, J. Dynamics at the solid-liquid transition: Experiments at the freezing point. *Phys. Rep.* **153**, 1–89 (1987).

66. Hartmut Löwen. Melting, freezing and colloidal suspensions. *Phys. Rep.* **237**, 249–324 (1994).

67. Reimar Finken, Matthias Schmidt, H. L. Freezing transition of hard hyperspheres. *Phys. Rev. E* **65**, 016108 (2001).

68. Luo, S.-N. Vibrational density of states and Lindemann melting law. *J. Chem. Phys.* **122**, 194709 (2005).

69. Hung, J.-H., Patra, T. K., Meenakshisundaram, V., Mangalara, J. H. & Simmons, D. S. Universal localization transition accompanying glass formation: insights from efficient molecular dynamics simulations of diverse supercooled liquids. *Soft Matter* **15**, 1223–1242 (2019).

70. Pazmiño Betancourt, B. A., Douglas, J. F. & Starr, F. W. Fragility and cooperative motion in a glass-forming polymer–nanoparticle composite. *Soft Matter* **9**, 241–254 (2013).

71. Becchi, M., Giuntoli, A. & Leporini, D. Molecular layers in thin supported films exhibit the same scaling as the bulk between slow relaxation and vibrational dynamics. *Soft Matter* **14**, 8814–8820 (2018).

72. Zhang, W., Starr, F. W. & Douglas, J. F. Reconciling computational and experimental trends in the temperature dependence of the interfacial mobility of polymer films. *J. Chem. Phys.* **152**, 124703 (2020).

73. Devyatko, Y. N. & Rogozhkin, S. V. Point defects at low-index surfaces of fcc metals and the anomalous behaviour of surface atoms at elevated temperatures. *Vacuum* **56**, 279–285 (2000).

74. Gjostein, N. A. *Surfaces and Interfaces I. Chemical and Physical Characteristics*. (Syracuse University Press, 1967).

75. Bonzel, H. P. A surface diffusion mechanism at high temperature. *Surf. Sci.* **21**, 45–60 (1970).

76. Wang, X., Tong, X., Zhang, H. & Douglas, J. F. String-like collective motion and diffusion in the interfacial region of ice. *J. Chem. Phys.* **147**, 194508 (2017).

77. Jayanthi, C. S., Tosatti, E. & Pietronero, L. Surface melting of copper. *Phys. Rev. B* **31**, 3456–3459 (1985).

78. Häkkinen, H. & Manninen, M. Computer simulation of disordering and premelting of low-index faces of copper. *Phys. Rev. B* **46**, 1725–1742 (1992).

79. Bonzel, H. P. & Gjostein, N. A. Molecular Processes on Solid Surfaces. in *Molecular Processes on Solid Surfaces* (eds. Draugcis, E., Gretz, R. D. & Jaffee, R. J.) (MCGraw-Hill, 1969).

80. Papageorgiou, D. G. & Evangelakis, G. A. Multiple excitations and self-diffusion processes on and near the Cu(110) surface by molecular dynamics simulations. *Surf. Sci.* **461**, L543–L549 (2000).

81. Swallen, S. F. *et al.* Organic Glasses with Exceptional Thermodynamic and Kinetic Stability. *Science (80-.).* **315**, 353–356 (2007).

82. Steltenpohl, A. & Memmel, N. Energetic and Entropic Contributions to Surface Diffusion

and Epitaxial Growth. *Phys. Rev. Lett.* **84**, 1728–1731 (2000).

83. Merkle, R. & Maier, J. On the Tammann-Rule. *J. Inorg. Gen. Chem.* **631**, 1163–1166 (2005).

84. Conkling, J. A. & Mocella, C. *Chemistry of Pyrotechnics: Basic Principles and Theory*. (Taylor & Francis Group, 1985).

85. Cybulski, A., Sharma, M. M., Sheldon, R. A. & Moulijn, J. A. *Fine Chemicals Manufacture Technology and Engineering*. (Elsevier Science, 2001).

86. Golunski, S. E. Final Analysis. *Platin. Met. Rev.* **51**, 162–162 (2007).

87. Lobo, L. S. & Carabineiro, S. A. C. Explaining Bamboo-Like Carbon Fiber Growth Mechanism: Catalyst Shape Adjustments above Tammann Temperature. *C — J. Carbon Res.* **6**, 18 (2020).

88. Dai, Y., Lu, P., Cao, Z., Campbell, C. T. & Xia, Y. The physical chemistry and materials science behind sinter-resistant catalysts. *Chem. Soc. Rev.* **47**, 4314–4331 (2018).

89. Finch, G. I. & Sinha, K. P. On Reaction in the Solid State. *Proc. R. Soc. Lond. A. Math. Phys. Sci.* **239**, 145–153 (1957).

90. Dash, J. G., Rempel, A. W. & Wettlaufer, J. S. The physics of premelted ice and its geophysical consequences. *Rev. Mod. Phys.* **78**, 695–741 (2006).

91. Sakka, S. & Mackenzie, J. D. Relation between apparent glass transition temperature and liquids temperature for inorganic glasses. *J. Non. Cryst. Solids* **6**, 145–162 (1971).

92. Boyer, R. F. The Relation of Transition Temperatures to Chemical Structure in High Polymers. *Rubber Chem. Technol.* **36**, 1303–1421 (1963).

93. Danilov, D., Hahn, H., Gleiter, H. & Wenzel, W. Mechanisms of Nanoglass Ultrastability. *ACS Nano* **10**, 3241–3247 (2016).

94. Tian, L. *et al.* Approaching the ideal elastic limit of metallic glasses. *Nat. Commun.* **3**, 609 (2012).

95. Jiang, Q. K. *et al.* Super elastic strain limit in metallic glass films. *Sci. Rep.* **2**, 852 (2012).

96. Jiang, Q. K. *et al.* The effect of size on the elastic strain limit in Ni60Nb40 glassy films. *Acta Mater.* **61**, 4689–4695 (2013).

97. Jang, D., Gross, C. T. & Greer, J. R. Effects of size on the strength and deformation mechanism in Zr-based metallic glasses. *Int. J. Plast.* **27**, 858–867 (2011).

98. Lee, S.-W., Jafary-Zadeh, M., Chen, D. Z., Zhang, Y.-W. & Greer, J. R. Size Effect Suppresses Brittle Failure in Hollow Cu 60 Zr 40 Metallic Glass Nanolattices Deformed at Cryogenic Temperatures. *Nano Lett.* **15**, 5673–5681 (2015).

99. Jang, D. & Greer, J. R. Transition from a strong-yet-brittle to a stronger-and-ductile state by size reduction of metallic glasses. *Nat. Mater.* **9**, 215–219 (2010).

100. Gu, X. W. *et al.* Mechanisms of Failure in Nanoscale Metallic Glass. *Nano Lett.* **14**, 5858–

5864 (2014).

101. Adibi, S. *et al.* A transition from localized shear banding to homogeneous superplastic flow in nanoglass. *Appl. Phys. Lett.* **103**, 211905 (2013).

102. Adibi, S., Branicio, P. S., Zhang, Y.-W. & Joshi, S. P. Composition and grain size effects on the structural and mechanical properties of CuZr nanoglasses. *J. Appl. Phys.* **116**, 043522 (2014).

103. Chen, D. Z. *et al.* Nanometallic Glasses: Size Reduction Brings Ductility, Surface State Drives Its Extent. *Nano Lett.* **13**, 4462–4468 (2013).

104. Wang, X. L. *et al.* Plasticity of a scandium-based nanoglass. *Scr. Mater.* **98**, 40–43 (2015).

105. Mendelev, M. I., Sordelet, D. J. & Kramer, M. J. Using atomistic computer simulations to analyze x-ray diffraction data from metallic glasses. *J. Appl. Phys.* **102**, 043501 (2007).

106. Lad, K. N., Jakse, N. & Pasturel, A. Signatures of fragile-to-strong transition in a binary metallic glass-forming liquid. *J. Chem. Phys.* **136**, 104509 (2012).

107. Pazmiño Betancourt, B. A., Starr, F. W. & Douglas, J. F. String-like collective motion in the α - and β -relaxation of a coarse-grained polymer melt. *J. Chem. Phys.* **148**, 104508 (2018).

108. Maradudin, A. A. & Melngailis, J. Some Dynamical Properties of Surface Atoms. *Phys. Rev.* **133**, A1188–A1193 (1964).

109. Clark, B. C., Herman, R. & Wallis, R. F. Theoretical Mean-Square Displacements for Surface Atoms in Face-Centered Cubic Lattices with Applications to Nickel. *Phys. Rev.* **139**, A860–A867 (1965).

110. Maradudin, A. A. & Flinn, P. A. Anharmonic Contributions to the Debye-Waller Factor. *Phys. Rev.* **129**, 2529–2547 (1963).

111. Dürr, H., Schneider, R. & Fauster, T. Anomalous dynamical behavior of the Cu(110) surface. *Phys. Rev. B* **43**, 12187–12194 (1991).

112. MacRae, A. U. & Germer, L. H. Thermal Vibrations of Surface Atoms. *Phys. Rev. Lett.* **8**, 489–490 (1962).

113. Jiang, Q. T., Fenter, P. & Gustafsson, T. Geometric structure and surface vibrations of Cu(001) determined by medium-energy ion scattering. *Phys. Rev. B* **44**, 5773–5778 (1991).

114. Yang, L. & Rahman, T. Enhanced anharmonicity on Cu(110). *Phys. Rev. Lett.* **67**, 2327–2330 (1991).

115. Fowler, D. E. & Barth, J. V. Structure and dynamics of the Cu(001) surface investigated by medium-energy ion scattering. *Phys. Rev. B* **52**, 2117–2124 (1995).

116. Cao, Y. & Conrad, E. Anomalous thermal expansion of Ni(001). *Phys. Rev. Lett.* **65**, 2808–2811 (1990).

117. Needs, R. J., Godfrey, M. J. & Mansfield, M. Theory of surface stress and surface reconstruction. *Surf. Sci.* **242**, 215–221 (1991).

118. Pavlovska, A., Dobrev, D. & Bauer, E. Surface melting versus surface non-melting: an equilibrium shape study. *Surf. Sci.* **286**, 176–181 (1993).

119. Takeuchi, N., Chan, C. T. & Ho, K. M. Theoretical study of noble-metal (100) surface reconstructions using first-principles techniques. *Phys. Rev. Lett.* **63**, 1273–1276 (1989).

120. Fiorentini, V., Methfessel, M. & Scheffler, M. Reconstruction mechanism of fcc transition metal (001) surfaces. *Phys. Rev. Lett.* **71**, 1051–1054 (1993).

121. Modak, V. P., Pathak, H., Thayer, M., Singer, S. J. & Wyslouzil, B. E. Experimental evidence for surface freezing in supercooled n-alkane nanodroplets. *Phys. Chem. Chem. Phys.* **15**, 6783 (2013).

122. Celestini, F., Ercolessi, F. & Tosatti, E. Can Liquid Metal Surfaces Have Hexatic Order? *Phys. Rev. Lett.* **78**, 3153–3156 (1997).

123. Schroeder, M. R. *Fractals, chaos, power laws : minutes from an infinite paradise*. (W H Freeman & Co, New York, 1991).

124. Ryu, S., Kang, K. & Cai, W. Entropic effect on the rate of dislocation nucleation. *Proc. Natl. Acad. Sci.* **108**, 5174–5178 (2011).

125. Zhu, T., Li, J., Samanta, A., Leach, A. & Gall, K. Temperature and Strain-Rate Dependence of Surface Dislocation Nucleation. *Phys. Rev. Lett.* **100**, 025502 (2008).

126. Faupel, F. *et al.* Diffusion in metallic glasses and supercooled melts. *Rev. Mod. Phys.* **75**, 237–280 (2003).

127. Boisvert, G., Lewis, L. J. & Yelon, A. Many-Body Nature of the Meyer-Neldel Compensation Law for Diffusion. *Phys. Rev. Lett.* **75**, 469–472 (1995).

128. Boisvert, G., Mousseau, N. & Lewis, L. J. Surface diffusion coefficients by thermodynamic integration: Cu on Cu(100). *Phys. Rev. B* **58**, 12667–12670 (1998).

129. Kürpick, U. Self-diffusion on (100), (110), and (111) surfaces of Ni and Cu: A detailed study of prefactors and activation energies. *Phys. Rev. B* **64**, 075418 (2001).

130. Starr, F. W., Douglas, J. F. & Sastry, S. The relationship of dynamical heterogeneity to the Adam-Gibbs and random first-order transition theories of glass formation. *J. Chem. Phys.* **138**, 12A541 (2013).

131. Molenbroek, A. M. & Frenken, J. W. M. Anharmonicity but absence of surface melting on Al(001). *Phys. Rev. B* **50**, 11132–11141 (1994).

132. Frenken, J. W. M., Huussen, F. & van der Veen, J. F. Evidence for anomalous thermal expansion at a crystal surface. *Phys. Rev. Lett.* **58**, 401–404 (1987).

133. Cao, Y. & Conrad, E. H. Approach to thermal roughening of Ni(110): A study by high-resolution low-energy electron diffraction. *Phys. Rev. Lett.* **64**, 447–450 (1990).

134. Zeppenfeld, P., Kern, K., David, R. & Comsa, G. No Thermal Roughening on Cu(110) up to 900 K. *Phys. Rev. Lett.* **62**, 63–66 (1989).

135. Faraday, M. I. Note on regelation. *Proc. R. Soc. London* **10**, 440–450 (1860).

136. Tammann, G. Zur Überhitzung von Kristallen. *Z. Phys. Chem.* **68**, 205 (1910).

137. Stranski, I. N. Über den Schmelzvorgang bei nichtpolaren Kristallen. *Naturwissenschaften* **30**, 425 (1942).

138. Armand, G. & Zeppenfeld, P. Surface anharmonicity on Cu(110). *Phys. Rev. B* **40**, 5936–5940 (1989).

139. Bienfait, M. Surface Premelting of CH4 Thin Films. *Europhys. Lett.* **4**, 79–84 (1987).

140. Alsayed, A. M., Islam, M. F., Zhang, J., Collings, P. J. & Yodh, A. G. Premelting at Defects Within Bulk Colloidal Crystals. *Science (80-.).* **309**, 1207–1210 (2005).

141. Feuchtwang, T. E. Dynamics of a Semi-Infinite Crystal Lattice in a Quasiharmonic Approximation. II. The Normal-Mode Analysis of a Semi-Infinite Lattice. *Phys. Rev.* **155**, 731–744 (1967).

142. Wallis, R. F., Clark, B. C. & Herman, R. Effects of Surface Force-Constant Changes on the Atomic Mean Square Displacements in Face-Centered Cubic Crystals with a Free Surface. *Phys. Rev.* **167**, 652–658 (1968).

143. Scheidler, P., Kob, W. & Binder, K. Cooperative motion and growing length scales in supercooled confined liquids. *Europhys. Lett.* **59**, 701–707 (2002).

144. Scheidler, P., Kob, W. & Binder, K. The Relaxation Dynamics of a Supercooled Liquid Confined by Rough Walls. *J. Phys. Chem. B* **108**, 6673–6686 (2004).

145. Peter, S., Meyer, H. & Baschnagel, J. Thickness-dependent reduction of the glass-transition temperature in thin polymer films with a free surface. *J. Polym. Sci. Part B Polym. Phys.* **44**, 2951–2967 (2006).

146. Zhang, J. *et al.* Molecular dynamics simulation of the melting behavior of copper nanorod. *Comput. Mater. Sci.* **143**, 248–254 (2018).

147. Bonzel, H. P. & Latta, E. E. Surface self-diffusion on Ni(110): Temperature dependence and directional anisotropy. *Surf. Sci.* **76**, 275–295 (1978).

148. Seebauer, E. Estimating surface diffusion coefficients. *Prog. Surf. Sci.* **49**, 265–330 (1995).

149. Horváth, J., Dyment, F. & Mehrer, H. Anomalous self-diffusion in a single crystal of α-zirconium. *J. Nucl. Mater.* **126**, 206–214 (1984).

150. Murzaev, R. T. *et al.* Discrete breathers in alpha-uranium. *Eur. Phys. J. B* **89**, 168 (2016).

151. Seeger, A. The mechanisms of diffusion in metals and alloys. *J. Less Common Met.* **28**, 387–418 (1972).

152. Okada, Y., Ikeda, M. & Aniya, M. Non-Arrhenius ionic conductivity in solid electrolytes: A theoretical model and its relation with the bonding nature. *Solid State Ionics* **281**, 43–48 (2015).

153. Truhlar, D. G. & Kohen, A. Convex Arrhenius plots and their interpretation. *Proc. Natl. Acad. Sci.* **98**, 848–851 (2001).

154. Liang, Z.-X., Lee, T., Resing, K. A., Ahn, N. G. & Klinman, J. P. Thermal-activated protein mobility and its correlation with catalysis in thermophilic alcohol dehydrogenase. *Proc. Natl. Acad. Sci.* **101**, 9556–9561 (2004).

155. Nagel, Z. D., Dong, M., Bahnson, B. J. & Klinman, J. P. Impaired protein conformational landscapes as revealed in anomalous Arrhenius prefactors. *Proc. Natl. Acad. Sci.* **108**, 10520–10525 (2011).

156. Li, Y., Petroski, J. & El-Sayed, M. A. Activation Energy of the Reaction between Hexacyanoferrate(III) and Thiosulfate Ions Catalyzed by Platinum Nanoparticles. *J. Phys. Chem. B* **104**, 10956–10959 (2000).

157. Zhang, H., Srolovitz, D. J., Douglas, J. F. & Warren, J. A. Grain boundaries exhibit the dynamics of glass-forming liquids. *Proc. Natl. Acad. Sci. U. S. A.* **106**, 7735–7740 (2009).

158. Rosato, V., Pontikis, V. & Ciccotti, G. Cooperative Premelting Effects on a (110) FCC Surface: A Molecular Dynamics Study. *MRS Proc.* **63**, 241 (1985).

159. Dodd, C. & MI, H. P. Viscosity and Density in the Supercooled Liquid State. *Proc. Phys. Soc. Sect. B* **62**, 454–460 (1949).

160. Greenwood, N. N. & Martin, R. L. Discontinuities in the physical properties of supercooled liquids. *Proc. R. Soc. London. Ser. A. Math. Phys. Sci.* **215**, 46–65 (1952).

161. Sharma, R., Chee, S.-W., Herzing, A., Miranda, R. & Rez, P. Evaluation of the Role of Au in Improving Catalytic Activity of Ni Nanoparticles for the Formation of One-Dimensional Carbon Nanostructures. *Nano Lett.* **11**, 2464–2471 (2011).

162. Lobo, L. S. Mechanism of Catalytic CNTs Growth in 400–650 °C Range: Explaining Volcano Shape Arrhenius Plot and Catalytic Synergism Using both Pt (or Pd) and Ni, Co or Fe. *C* **5**, 42 (2019).

163. Heuer, J. K., Okamoto, P. R., Lam, N. Q. & Stubbins, J. F. Relationship between segregation-induced intergranular fracture and melting in the nickel–sulfur system. *Appl. Phys. Lett.* **76**, 3403–3405 (2000).

164. Psurek, T., Soles, C. L., Page, K. A., Cicerone, M. T. & Douglas, J. F. Quantifying Changes in the High-Frequency Dynamics of Mixtures by Dielectric Spectroscopy †. *J. Phys. Chem. B* **112**, 15980–15990 (2008).

165. Anopchenko, A., Psurek, T., VanderHart, D., Douglas, J. F. & Obrzut, J. Dielectric study of the antiplasticization of trehalose by glycerol. *Phys. Rev. E* **74**, 031501 (2006).

166. Riggleman, R. A., Douglas, J. F. & de Pablo, J. J. Antiplasticization and the elastic properties of glass-forming polymer liquids. *Soft Matter* **6**, 292–304 (2010).

167. Cicerone, M. T. & Douglas, J. F. β-Relaxation governs protein stability in sugar-glass matrices. *Soft Matter* **8**, 2983 (2012).

168. De Michele, C., Del Gado, E. & Leporini, D. Scaling between structural relaxation and particle caging in a model colloidal gel. *Soft Matter* **7**, 4025 (2011).

169. Fujimoto, K. & Kaneko, K. How fast elements can affect slow dynamics. *Phys. D Nonlinear*

Phenom. **180**, 1–16 (2003).

170. Pettini, M. & Landolfi, M. Relaxation properties and ergodicity breaking in nonlinear Hamiltonian dynamics. *Phys. Rev. A* **41**, 768–783 (1990).

171. Matsuyama, H. J. & Konishi, T. Multistage slow relaxation in a Hamiltonian system: The Fermi-Pasta-Ulam model. *Phys. Rev. E* **92**, 022917 (2015).

172. Chirikov, B. V. A universal instability of many-dimensional oscillator systems. *Phys. Rep.* **52**, 263–379 (1979).

173. Casetti, L., Livi, R. & Pettini, M. Gaussian Model for Chaotic Instability of Hamiltonian Flows. *Phys. Rev. Lett.* **74**, 375–378 (1995).

174. Dauxois, T., Ruffo, S. & Torcini, A. Modulational estimate for the maximal Lyapunov exponent in Fermi-Pasta-Ulam chains. *Phys. Rev. E* **56**, R6229–R6232 (1997).

175. Cretegny, T., Dauxois, T., Ruffo, S. & Torcini, A. Localization and equipartition of energy in the β-FPU chain: Chaotic breathers. *Phys. D Nonlinear Phenom.* **121**, 109–126 (1998).

176. Kaneko, K. & Konishi, T. Diffusion in Hamiltonian dynamical systems with many degrees of freedom. *Phys. Rev. A* **40**, 6130–6133 (1989).

177. Yamaguchi, Y. Y. & Konishi, T. A Geometrical Model for Stagnant Motion in Hamiltonian Systems with Many Degrees of Freedom. *Prog. Theor. Phys.* **99**, 139–144 (1998).

178. Xia, W. *et al.* Energy renormalization for coarse-graining polymers having different segmental structures. *Sci. Adv.* **5**, eaav4683 (2019).

179. Bernu, B., Hansen, J. P., Hiwatari, Y. & Pastore, G. Soft-sphere model for the glass transition in binary alloys: Pair structure and self-diffusion. *Phys. Rev. A* **36**, 4891–4903 (1987).

180. Goldstein, M. Some Thermodynamic Aspects of the Glass Transition: Free Volume, Entropy, and Enthalpy Theories. *J. Chem. Phys.* **39**, 3369–3374 (1963).

181. Goldstein, M. Viscous Liquids and the Glass Transition: A Potential Energy Barrier Picture. *J. Chem. Phys.* **51**, 3728–3739 (1969).

182. Caruthers, J. M. & Medvedev, G. A. Quantitative model of super-Arrhenian behavior in glass forming materials. *Phys. Rev. Mater.* **2**, 055604 (2018).

183. Medvedev, G. A. & Caruthers, J. M. A Quantitative Model of Super-Arrhenian Behavior in Glass-Forming Polymers. *Macromolecules* **52**, 1424–1439 (2019).

184. Schweizer, K. S. & Yatsenko, G. Collisions, caging, thermodynamics, and jamming in the barrier hopping theory of glassy hard sphere fluids. *J. Chem. Phys.* **127**, 164505 (2007).

185. Mirigian, S. & Schweizer, K. S. Elastically cooperative activated barrier hopping theory of relaxation in viscous fluids. II. Thermal liquids. *J. Chem. Phys.* **140**, 194507 (2014).

186. Mittal, J. Using Compressibility Factor as a Predictor of Confined Hard-Sphere Fluid Dynamics †. *J. Phys. Chem. B* **113**, 13800–13804 (2009).

187. Turnbull, D. & Cohen, M. H. On the Free-Volume Model of the Liquid-Glass Transition. *J. Chem. Phys.* **52**, 3038–3041 (1970).

188. Fox, T. G. & Flory, P. J. The glass temperature and related properties of polystyrene. Influence of molecular weight. *J. Polym. Sci.* **14**, 315–319 (1954).

189. Hildebrand, J. H. & Lamoreaux, R. H. Fluidity: A General Theory. *Proc. Natl. Acad. Sci.* **69**, 3428–3431 (1972).

190. Cohen, M. H. & Grest, G. S. Liquid-glass transition, a free-volume approach. *Phys. Rev. B* **20**, 1077–1098 (1979).

191. Dyre, J. C. Colloquium : The glass transition and elastic models of glass-forming liquids. *Rev. Mod. Phys.* **78**, 953–972 (2006).

192. Zaccai, G. How Soft Is a Protein? A Protein Dynamics Force Constant Measured by Neutron Scattering. *Science (80-.).* **288**, 1604–1607 (2000).

193. Livi, R., Pettini, M., Ruffo, S., Sparpaglione, M. & Vulpiani, A. Equipartition threshold in nonlinear large Hamiltonian systems: The Fermi-Pasta-Ulam model. *Phys. Rev. A* **31**, 1039–1045 (1985).

194. Das, M. & Green, J. R. Critical fluctuations and slowing down of chaos. *Nat. Commun.* **10**, 2155 (2019).

195. Xu, W.-S., Douglas, J. F. & Freed, K. F. Influence of Cohesive Energy on the Thermodynamic Properties of a Model Glass-Forming Polymer Melt. *Macromolecules* **49**, 8341–8354 (2016).

196. Torquato, S. Hyperuniform states of matter. *Phys. Rep.* **745**, 1–95 (2018).

197. Flach, S. & Siewert, J. Dynamical scaling properties of a one-dimensional Phi4 lattice model-comparison with mode coupling theory. *J. Phys. Condens. Matter* **4**, L363–L370 (1992).

198. Lobo, L. S. & Carabineiro, S. A. C. Kinetics and mechanism of catalytic carbon gasification. *Fuel* **183**, 457–469 (2016).

199. Schwarzschild, B. M. Catalysis of carbon gasification. *Phys. Today* **34**, 19–21 (1981).

200. Lobo, L. S. Nucleation and growth of carbon nanotubes and nanofibers: Mechanism and catalytic geometry control. *Carbon N. Y.* **114**, 411–417 (2017).

201. Hofmann, S., Csányi, G., Ferrari, A. C., Payne, M. C. & Robertson, J. Surface Diffusion: The Low Activation Energy Path for Nanotube Growth. *Phys. Rev. Lett.* **95**, 036101 (2005).

202. Tian, Y. *et al.* Fast coalescence of metallic glass nanoparticles. *Nat. Commun.* **10**, 5249 (2019).

203. José-Yacamán, M. *et al.* Surface Diffusion and Coalescence of Mobile Metal Nanoparticles. *J. Phys. Chem. B* **109**, 9703–9711 (2005).

204. Goudeli, E. & Pratsinis, S. E. Crystallinity dynamics of gold nanoparticles during sintering or coalescence. *AIChE J.* **62**, 589–598 (2016).

205. Cao, A., Lu, R. & Veser, G. Stabilizing metal nanoparticles for heterogeneous catalysis. *Phys. Chem. Chem. Phys.* **12**, 13499 (2010).

206. Kuo, C.-W., Jeng, S.-C., Wang, H.-L. & Liao, C.-C. Application of nanoparticle-induced vertical alignment in hybrid-aligned nematic liquid crystal cell. *Appl. Phys. Lett.* **91**, 141103 (2007).

207. Ko, S. H. *et al.* All-inkjet-printed flexible electronics fabrication on a polymer substrate by low-temperature high-resolution selective laser sintering of metal nanoparticles. *Nanotechnology* **18**, 345202 (2007).

208. Park, B. K., Kim, D., Jeong, S., Moon, J. & Kim, J. S. Direct writing of copper conductive patterns by ink-jet printing. *Thin Solid Films* **515**, 7706–7711 (2007).

209. Kim, D. & Moon, J. Highly Conductive Ink Jet Printed Films of Nanosilver Particles for Printable Electronics. *Electrochem. Solid-State Lett.* **8**, J30 (2005).

210. Weber, B. *et al.* Molecular Insight into the Slipperiness of Ice. *J. Phys. Chem. Lett.* **9**, 2838–2842 (2018).

211. Sun, Y., Zhu, L., Kearns, K. L., Ediger, M. D. & Yu, L. Glasses crystallize rapidly at free surfaces by growing crystals upward. *Proc. Natl. Acad. Sci.* **108**, 5990–5995 (2011).

212. Wu, T. & Yu, L. Surface Crystallization of Indomethacin Below T g. *Pharm. Res.* **23**, 2350–2355 (2006).

213. Zhu, L., Jona, J., Nagapudi, K. & Wu, T. Fast Surface Crystallization of Amorphous Griseofulvin Below T g. *Pharm. Res.* **27**, 1558–1567 (2010).

214. Sun, J. *et al.* Liquid-like pseudoelasticity of sub-10-nm crystalline silver particles. *Nat. Mater.* **13**, 1007–1012 (2014).

215. Cao, C. R. *et al.* Liquid-like behaviours of metallic glassy nanoparticles at room temperature. *Nat. Commun.* **10**, 1966 (2019).

216. Losurdo, M., Suvorova, A., Rubanov, S., Hingerl, K. & Brown, A. S. Thermally stable coexistence of liquid and solid phases in gallium nanoparticles. *Nat. Mater.* **15**, 995–1002 (2016).

217. Aguado, A. Neither solid nor liquid. *Nat. Mater.* **15**, 931–933 (2016).

218. Hansen, P. L. *et al.* Atom-Resolved Imaging of Dynamic Shape Changes in Supported Copper Nanocrystals. *Science (80-.).* **295**, 2053–2055 (2002).

219. Miki-Yoshida, M., Tehuacanero, S. & José-Yacamán, M. On the high temperature coalescence of metallic nanocrystals. *Surf. Sci.* **274**, L569–L576 (1992).

220. Iijima, S. & Ichihashi, T. Structural instability of ultrafine particles of metals. *Phys. Rev. Lett.* **56**, 616–619 (1986).

221. Baker, R. The relationship between particle motion on a graphite surface and Tammann temperature. *J. Catal.* **78**, 473–476 (1982).

222. Klemperer, W. & Vaida, V. Molecular complexes in close and far away. *Proc. Natl. Acad.*

Sci. **103**, 10584–10588 (2006).

223. Kulmala, M. How Particles Nucleate and Grow. *Science (80-.).* **302**, 1000–1001 (2003).

224. Molina, M. J. Polar Ozone Depletion(Nobel Lecture). *Angew. Chemie Int. Ed. English* **35**, 1778–1785 (1996).

225. Johnston, J. C. & Molinero, V. Crystallization, Melting, and Structure of Water Nanoparticles at Atmospherically Relevant Temperatures. *J. Am. Chem. Soc.* **134**, 6650–6659 (2012).

226. Zhou, Y., Vitkup, D. & Karplus, M. Native proteins are surface-molten solids: application of the lindemann criterion for the solid versus liquid state 1 1Edited by A. R. Fersht. *J. Mol. Biol.* **285**, 1371–1375 (1999).

227. Haddadian, E. J., Zhang, H., Freed, K. F. & Douglas, J. F. Comparative Study of the Collective Dynamics of Proteins and Inorganic Nanoparticles. *Sci. Rep.* **7**, 41671 (2017).

228. Horstmann, R. & Vogel, M. Common behaviors associated with the glass transitions of water-like models. *J. Chem. Phys.* **147**, 034505 (2017).

229. Riggleman, R. A., Douglas, J. F. & de Pablo, J. J. Tuning polymer melt fragility with antiplasticizer additives. *J. Chem. Phys.* **126**, 234903 (2007).

230. Blodgett, M. E., Egami, T., Nussinov, Z. & Kelton, K. F. Proposal for universality in the viscosity of metallic liquids. *Sci. Rep.* **5**, 13837 (2015).

231. Yeshchenko, O. A., Dmitruk, I. M., Alexeenko, A. A. & Dmytruk, A. M. Size-dependent melting of spherical copper nanoparticles embedded in a silica matrix. *Phys. Rev. B* **75**, 085434 (2007).

232. Voronin, B. . & Volkov, S. . Ionic conductivity of fluorite type crystals CaF2, SrF2, BaF2, and SrCl2 at high temperatures. *J. Phys. Chem. Solids* **62**, 1349–1358 (2001).

233. Deng, C. & Schuh, C. A. Atomistic Simulation of Slow Grain Boundary Motion. *Phys. Rev. Lett.* **106**, 045503 (2011).

234. Xu, W.-S., Douglas, J. F., Xia, W. & Xu, X. Investigation of the Temperature Dependence of Activation Volume in Glass-Forming Polymer Melts under Variable Pressure Conditions. *Macromolecules* **53**, 6828–6841 (2020).

235. Xu, W.-S., Douglas, J. F., Xia, W. & Xu, X. Understanding Activation Volume in Glass-Forming Polymer Melts via Generalized Entropy Theory. *Macromolecules* **53**, 7239–7252 (2020).

236. Sausset, F., Tarjus, G. & Viot, P. Tuning the Fragility of a Glass-Forming Liquid by Curving Space. *Phys. Rev. Lett.* **101**, 155701 (2008).

237. Tarjus, G., Sausset, F. & Viot, P. Statistical Mechanics of Liquids and Fluids in Curved Space. in 251–310 (2011). doi:10.1002/9781118158715.ch4.

238. Chevalier, Y. & Bolzinger, M.-A. Emulsions stabilized with solid nanoparticles: Pickering emulsions. *Colloids Surfaces A Physicochem. Eng. Asp.* **439**, 23–34 (2013).

239. Dinsmore, A. D. *et al.* Colloidosomes: Selectively Permeable Capsules Composed of Colloidal Particles. *Science (80-.).* **298**, 1006–1009 (2002).

240. Bausch, A. R. *et al.* Grain Boundary Scars and Spherical Crystallography. *Science (80-.).* **299**, 1716–1718 (2003).

241. Stratford, K., Adhikari, R., Pagonabarraga, I., Desplat, J.-C. & Cates, M. E. Colloidal Jamming at Interfaces: A Route to Fluid-Bicontinuous Gels. *Science (80-.).* **309**, 2198–2201 (2005).

242. Ding, Y. *et al.* Polymer Viscoelasticity and Residual Stress Effects on Nanoimprint Lithography. *Adv. Mater.* **19**, 1377–1382 (2007).

243. Chen, Y. *et al.* Hierarchically Patterned Elastomeric and Thermoplastic Polymer Films through Nanoimprinting and Ultraviolet Light Exposure. *ACS Omega* **3**, 15426–15434 (2018).

244. Zhang, W. *et al.* The interfacial zone in thin polymer films and around nanoparticles in polymer nanocomposites. *J. Chem. Phys.* **151**, 124705 (2019).

245. Takagi, M. Electron-Diffraction Study of Liquid-Solid Transition of Thin Metal Films. *J. Phys. Soc. Japan* **9**, 359–363 (1954).

246. Buffat, P. & Borel, J.-P. Size effect on the melting temperature of gold particles. *Phys. Rev. A* **13**, 2287–2298 (1976).

247. Couchman, P. R. & Jesser, W. A. Thermodynamic theory of size dependence of melting temperature in metals. *Nature* **269**, 481–483 (1977).

248. Jiang, Q., Zhang, S. & Zhao, M. Size-dependent melting point of noble metals. *Mater. Chem. Phys.* **82**, 225–227 (2003).

249. Lu, H. M., Li, P. Y., Cao, Z. H. & Meng, X. K. Size-, Shape-, and Dimensionality-Dependent Melting Temperatures of Nanocrystals. *J. Phys. Chem. C* **113**, 7598–7602 (2009).

250. Mishin, Y., Mehl, M. J., Papaconstantopoulos, D. A., Voter, A. F. & Kress, J. D. Structural stability and lattice defects in copper: Ab initio , tight-binding, and embedded-atom calculations. *Phys. Rev. B* **63**, 224106 (2001).

251. Uppenbrink, J. & Wales, D. J. Structure and dynamics of model metal clusters. *J. Chem. Phys.* **98**, 5720–5733 (1993).

252. Noya, E. G., Doye, J. P. K. & Calvo, F. Theoretical study of the melting of aluminum clusters. *Phys. Rev. B* **73**, 125407 (2006).

253. Neal, C. M., Starace, A. K. & Jarrold, M. F. Ion calorimetry: Using mass spectrometry to measure melting points. *J. Am. Soc. Mass Spectrom.* **18**, 74–81 (2007).

254. Aguado, A. & Jarrold, M. F. Melting and Freezing of Metal Clusters. *Annu. Rev. Phys. Chem.* **62**, 151–172 (2011).

255. Doye, J. P. K. & Wales, D. J. Global minima for transition metal clusters described by

Sutton–Chen potentials. *New J. Chem.* **22**, 733–744 (1998).

256. Noya, E. G., Doye, J. P. K., Wales, D. J. & Aguado, A. Geometric magic numbers of sodium clusters: Interpretation of the melting behaviour. *Eur. Phys. J. D* **43**, 57–60 (2007).

257. Sussman, D. M., Schoenholz, S. S., Cubuk, E. D. & Liu, A. J. Disconnecting structure and dynamics in glassy thin films. *Proc. Natl. Acad. Sci.* **114**, 10601–10605 (2017).

258. Hanakata, P. Z., Douglas, J. F. & Starr, F. W. Interfacial mobility scale determines the scale of collective motion and relaxation rate in polymer films. *Nat. Commun.* **5**, 4163 (2014).

259. Gilbert, B., Huang, F., Zhang, H., Waychunas, G. A. & Banfield, J. F. Nanoparticles: Strained and Stiff. *Science (80-.).* **305**, 651–654 (2004).

260. Wang, N., Rokhlin, S. I. & Farson, D. F. Nonhomogeneous surface premelting of Au nanoparticles. *Nanotechnology* **19**, 415701 (2008).

261. Wenzel, L. *et al.* Enhanced anharmonicity in the interaction of low- Z adsorbates with metal-surfaces. *Phys. Rev. Lett.* **64**, 1765–1768 (1990).

262. Stern, E. A., Līvņš, P. & Zhang, Z. Thermal vibration and melting from a local perspective. *Phys. Rev. B* **43**, 8850–8860 (1991).

263. Frenkel, A. I. & Rehr, J. J. Thermal expansion and x-ray-absorption fine-structure cumulants. *Phys. Rev. B* **48**, 585–588 (1993).

264. Yokoyama, T., Ohta, T. & Sato, H. Thermal expansion and anharmonicity of solid Kr studied by extended x-ray-absorption fine structure. *Phys. Rev. B* **55**, 11320–11329 (1997).

265. Kiguchi, M. *et al.* Surface structures and thermal vibrations of Ni and Cu thin films studied by extended x-ray-absorption fine structure. *Phys. Rev. B* **61**, 14020–14027 (2000).

266. Van Hung, N. & Rehr, J. J. Anharmonic correlated Einstein-model Debye-Waller factors. *Phys. Rev. B* **56**, 43–46 (1997).

267. Yokoyama, T. & Ohta, T. Temperature-Dependent EXAFS Study on Supported Silver and Palladium Clusters: Comparison of Their Interatomic Potentials with Those of Bulk Metals. *Jpn. J. Appl. Phys.* **29**, 2052–2058 (1990).

268. Van Hung, N., Hue, T. T., Khoa, H. D. & Vuong, D. Q. Anharmonic correlated Debye model high-order expanded interatomic effective potential and Debye-Waller factors of bcc crystals. *Phys. B Condens. Matter* **503**, 174–178 (2016).

269. Liu, P. C., Okamoto, P. R., Zaluzec, N. J. & Meshii, M. Boron-implantation-induced crystalline-to-amorphous transition in nickel: An experimental assessment of the generalized Lindemann melting criterion. *Phys. Rev. B* **60**, 800–814 (1999).

270. HUNG, N. VAN, TIEN, T. S., HUNG, L. H. & FRAHM, R. R. ANHARMONIC EFFECTIVE POTENTIAL, LOCAL FORCE CONSTANT AND EXAFS OF HCP CRYSTALS: THEORY AND COMPARISON TO EXPERIMENT. *Int. J. Mod. Phys. B* **22**, 5155–5166 (2008).

271. Soles, C. L. *et al.* Importance of Sub-Nanosecond Fluctuations on the Toughness of

Polycarbonate Glasses. *Macromolecules* **53**, 6672–6681 (2020).

272. Buchenau, U., Zorn, R. & Ramos, M. A. Probing cooperative liquid dynamics with the mean square displacement. *Phys. Rev. E* **90**, 042312 (2014).

273. Sangiovanni, D. G. *et al.* Superioniclike Diffusion in an Elemental Crystal: bcc Titanium. *Phys. Rev. Lett.* **123**, 105501 (2019).

274. Knorr, P. & Herzig, C. Tracer diffusion of hafnium, niobium and zirconium in Hf-Nb alloys. *J. Phys. Condens. Matter* **7**, 9185–9200 (1995).

275. Nachtrieb, N. H. & Handler, G. S. Self-Diffusion in α White Phosphorus. *J. Chem. Phys.* **23**, 1187–1193 (1955).

276. Rhead, G. E. On surface diffusion and the existence of "two-dimensional" liquids. *Surf. Sci.* **15**, 353–357 (1969).

277. McQuarrie, D. A. *Statistical mechanics*. (University Science Books, Sausalito, CA, 2000).

278. Bell, A. T. The Impact of Nanoscience on Heterogeneous Catalysis. *Science (80-.).* **299**, 1688–1691 (2003).

279. Jimenez-Izal, E. & Alexandrova, A. N. Computational Design of Clusters for Catalysis. *Annu. Rev. Phys. Chem.* **69**, 377–400 (2018).

280. Li, L. *et al.* Noncrystalline-to-Crystalline Transformations in Pt Nanoparticles. *J. Am. Chem. Soc.* **135**, 13062–13072 (2013).

281. Veith, G. M. *et al.* Thermal stability and catalytic activity of gold nanoparticles supported on silica. *J. Catal.* **262**, 92–101 (2009).

282. Haruta, M. Size- and support-dependency in the catalysis of gold. *Catal. Today* **36**, 153–166 (1997).

283. van Deelen, T. W., Hernández Mejía, C. & de Jong, K. P. Control of metal-support interactions in heterogeneous catalysts to enhance activity and selectivity. *Nat. Catal.* **2**, 955–970 (2019).

284. Cargnello, M. *et al.* Control of Metal Nanocrystal Size Reveals Metal-Support Interface Role for Ceria Catalysts. *Science (80-.).* **341**, 771–773 (2013).

285. Zhang, S. *et al.* Dynamical Observation and Detailed Description of Catalysts under Strong Metal–Support Interaction. *Nano Lett.* **16**, 4528–4534 (2016).

286. Ha, H., Yoon, S., An, K. & Kim, H. Y. Catalytic CO Oxidation over Au Nanoparticles Supported on CeO 2 Nanocrystals: Effect of the Au–CeO 2 Interface. *ACS Catal.* **8**, 11491–11501 (2018).

287. Ro, I., Resasco, J. & Christopher, P. Approaches for Understanding and Controlling Interfacial Effects in Oxide-Supported Metal Catalysts. *ACS Catal.* **8**, 7368–7387 (2018).

288. Narayanan, R. & El-Sayed, M. A. Changing Catalytic Activity during Colloidal Platinum Nanocatalysis Due to Shape Changes: Electron-Transfer Reaction. *J. Am. Chem. Soc.* **126**, 7194–7195 (2004).

289. Narayanan, R. & El-Sayed, M. A. Catalysis with Transition Metal Nanoparticles in Colloidal Solution: Nanoparticle Shape Dependence and Stability. *J. Phys. Chem. B* **109**, 12663–12676 (2005).

290. Lee, I., Morales, R., Albiter, M. A. & Zaera, F. Synthesis of heterogeneous catalysts with well shaped platinum particles to control reaction selectivity. *Proc. Natl. Acad. Sci.* **105**, 15241–15246 (2008).

291. Lee, I., Delbecq, F., Morales, R., Albiter, M. A. & Zaera, F. Tuning selectivity in catalysis by controlling particle shape. *Nat. Mater.* **8**, 132–138 (2009).

292. Mostafa, S. *et al.* Shape-Dependent Catalytic Properties of Pt Nanoparticles. *J. Am. Chem. Soc.* **132**, 15714–15719 (2010).

293. Zaera, F. Outstanding Mechanistic Questions in Heterogeneous Catalysis. *J. Phys. Chem. B* **106**, 4043–4052 (2002).

294. Cuenya, B. R. Synthesis and catalytic properties of metal nanoparticles: Size, shape, support, composition, and oxidation state effects. *Thin Solid Films* **518**, 3127–3150 (2010).

295. Ahmadi, M., Mistry, H. & Roldan Cuenya, B. Tailoring the Catalytic Properties of Metal Nanoparticles via Support Interactions. *J. Phys. Chem. Lett.* **7**, 3519–3533 (2016).

296. Nørskov, J. K., Bligaard, T., Rossmeisl, J. & Christensen, C. H. Towards the computational design of solid catalysts. *Nat. Chem.* **1**, 37–46 (2009).

297. Sambur, J. B. & Chen, P. Approaches to Single-Nanoparticle Catalysis. *Annu. Rev. Phys. Chem.* **65**, 395–422 (2014).

298. Fang, Y. *et al.* Intermittent photocatalytic activity of single CdS nanoparticles. *Proc. Natl. Acad. Sci.* **114**, 10566–10571 (2017).

299. Xu, W., Kong, J. S. & Chen, P. Probing the catalytic activity and heterogeneity of Au-nanoparticles at the single-molecule level. *Phys. Chem. Chem. Phys.* **11**, 2767 (2009).

300. Zhou, X., Xu, W., Liu, G., Panda, D. & Chen, P. Size-Dependent Catalytic Activity and Dynamics of Gold Nanoparticles at the Single-Molecule Level. *J. Am. Chem. Soc.* **132**, 138–146 (2010).

301. Xu, W., Kong, J. S., Yeh, Y.-T. E. & Chen, P. Single-molecule nanocatalysis reveals heterogeneous reaction pathways and catalytic dynamics. *Nat. Mater.* **7**, 992–996 (2008).

302. Chen, T., Zhang, Y. & Xu, W. Size-dependent catalytic kinetics and dynamics of Pd nanocubes: a single-particle study. *Phys. Chem. Chem. Phys.* **18**, 22494–22502 (2016).

303. Cortie, M. & van der Lingen, E. Catalytic gold nano-particles. *Mater. Forum* **26**, 1–14 (2002).

304. Marchak, D. *et al.* Large Anisotropic Conductance and Band Gap Fluctuations in Nearly Round-Shape Bismuth Nanoparticles. *Nano Lett.* **12**, 1087–1091 (2012).

305. Bradac, C. *et al.* Observation and control of blinking nitrogen-vacancy centres in discrete nanodiamonds. *Nat. Nanotechnol.* **5**, 345–349 (2010).

306. Frantsuzov, P., Kuno, M., Jankó, B. & Marcus, R. A. Universal emission intermittency in quantum dots, nanorods and nanowires. *Nat. Phys.* **4**, 519–522 (2008).

307. Pelton, M., Grier, D. G. & Guyot-Sionnest, P. Characterizing quantum-dot blinking using noise power spectra. *Appl. Phys. Lett.* **85**, 819–821 (2004).

308. Nolte, P. *et al.* Shape Changes of Supported Rh Nanoparticles During Oxidation and Reduction Cycles. *Science (80-.).* **321**, 1654–1658 (2008).

309. Cervantes-Sodi, F. *et al.* Viscous State Effect on the Activity of Fe Nanocatalysts. *ACS Nano* **4**, 6950–6956 (2010).

310. Hofmann, S. *et al.* In situ Observations of Catalyst Dynamics during Surface-Bound Carbon Nanotube Nucleation. *Nano Lett.* **7**, 602–608 (2007).

311. Moseler, M., Cervantes-Sodi, F., Hofmann, S., Csányi, G. & Ferrari, A. C. Dynamic Catalyst Restructuring during Carbon Nanotube Growth. *ACS Nano* **4**, 7587–7595 (2010).

312. Lin, P. A. *et al.* Direct evidence of atomic-scale structural fluctuations in catalyst nanoparticles. *J. Catal.* **349**, 149–155 (2017).

313. Blaisten-Barojas, E., Garzón, I. L. & Avalos-Borja, M. Melting and freezing of Lennard-Jones clusters on a surface. *Phys. Rev. B* **36**, 8447–8455 (1987).

314. Ding, F., Rosén, A., Curtarolo, S. & Bolton, K. Modeling the melting of supported clusters. *Appl. Phys. Lett.* **88**, 133110 (2006).

315. Antonelli, A., Khanna, S. N. & Jena, P. Thermal stability of supported metal clusters. *Phys. Rev. B* **48**, 8263–8266 (1993).

316. Roldan Cuenya, B. *et al.* Anomalous lattice dynamics and thermal properties of supported size- and shape-selected Pt nanoparticles. *Phys. Rev. B* **82**, 155450 (2010).

317. Roldan Cuenya, B. *et al.* Thermodynamic properties of Pt nanoparticles: Size, shape, support, and adsorbate effects. *Phys. Rev. B* **84**, 245438 (2011).

318. Wulff, G. XXV. Zur Frage der Geschwindigkeit des Wachsthums und der Auflösung der Krystallflächen. *Zeitschrift für Krist. - Cryst. Mater.* **34**, 449–530 (1901).

319. Winterbottom, W. . Equilibrium shape of a small particle in contact with a foreign substrate. *Acta Metall.* **15**, 303–310 (1967).

320. Henry, C. R. Morphology of supported nanoparticles. *Prog. Surf. Sci.* **80**, 92–116 (2005).

321. Enterkin, J. A., Poeppelmeier, K. R. & Marks, L. D. Oriented Catalytic Platinum Nanoparticles on High Surface Area Strontium Titanate Nanocuboids. *Nano Lett.* **11**, 993–997 (2011).

322. Zhong, J. Superheating of Ag nanoparticles embedded in Ni matrix. *Acta Mater.* **49**, 2897–2904 (2001).

323. Liu, S. *et al.* Ultrastable Au nanoparticles on titania through an encapsulation strategy under oxidative atmosphere. *Nat. Commun.* **10**, 5790 (2019).

324. Fan, X. Graphene: A Promising Two-Dimensional Support for Heterogeneous Catalysts. *Front. Mater.* **1**, (2015).

325. Julkapli, N. M. & Bagheri, S. Graphene supported heterogeneous catalysts: An overview. *Int. J. Hydrogen Energy* **40**, 948–979 (2015).

326. Yan, Y. *et al.* A recent trend: application of graphene in catalysis. *Carbon Lett.* **31**, 177–199 (2021).

327. Haxhiaj, I. *et al.* Platinum nanoparticles supported on reduced graphene oxide prepared in situ by a continuous one-step laser process. *Appl. Surf. Sci.* **469**, 811–820 (2019).

328. do Nascimento, J. R., D'Oliveira, M. R., Veiga, A. G., Chagas, C. A. & Schmal, M. Synthesis of Reduced Graphene Oxide as a Support for Nano Copper and Palladium/Copper Catalysts for Selective NO Reduction by CO. *ACS Omega* **5**, 25568–25581 (2020).

329. *Graphene-Based Nanomaterial Catalysis*. (BENTHAM SCIENCE PUBLISHERS, 2022). doi:10.2174/97898150404941220101.

330. Zhang, W., Starr, F. W., Beers, K. L. & Douglas, J. F. Reactive Molecular Dynamics Simulations of the Depolymerization of Polyethylene Using Graphene-Oxide-Supported Platinum Nanoparticles. *J. Phys. Chem. A* **126**, 3167–3173 (2022).

331. Huang, H. *et al.* Radiation damage resistance and interface stability of copper–graphene nanolayered composite. *J. Nucl. Mater.* **460**, 16–22 (2015).

332. Zhang, H., Kalvapalle, P. & Douglas, J. F. String-Like Collective Atomic Motion in the Melting and Freezing of Nanoparticles. *J. Phys. Chem. B* **115**, 14068–14076 (2011).

333. Wang, X., Zhang, H. & Douglas, J. F. The initiation of shear band formation in deformed metallic glasses from soft localized domains. *J. Chem. Phys.* **155**, 204504 (2021).

334. Liu, Y. H. *et al.* Characterization of Nanoscale Mechanical Heterogeneity in a Metallic Glass by Dynamic Force Microscopy. *Phys. Rev. Lett.* **106**, 125504 (2011).

335. Wang, D. P., Qiao, J. C. & Liu, C. T. Relating structural heterogeneity to β relaxation processes in metallic glasses. *Mater. Res. Lett.* **7**, 305–311 (2019).

Appendix A: Supplementary Information of Chapter 3

Supplementary Information: Localization Model Description of the Interfacial Dynamics of Crystalline Cu and $Cu_{64}Zr_{36}$ Metallic Glass Films

A.1 Arrhenius Plots of the Self-Diffusion Coefficient $D(T)$

The atomic self-dffusion coefficient is calculated in the usual fashion by first determining the mean square displacement, $MSD = \langle \frac{1}{N}\sum_{n=1}^{N}\{(x_i - x_0)^2 + (y_i - y_0)^2 + (z_i - z_0)^2\}\rangle$, where (x_0, y_0, z_0) and (x_i, y_i, z_i) are particle's initial and final positions after time t, respectively, and N is the number of atoms. We consider only the initial position of the atoms to determine whether they belong to the interface or inside the films regardless of their final position for all calculations in this study. We only consider three dimensional interfacial dynamics. After calculating the MSD for sufficiently long time, we estimated D from the slope of the fitted MSD versus t at long times, *i.e.,* $D = slope/6$. Some example MSD plots are given the Figure S1. Slope of all curves were taken from the linear fittings of the curves.
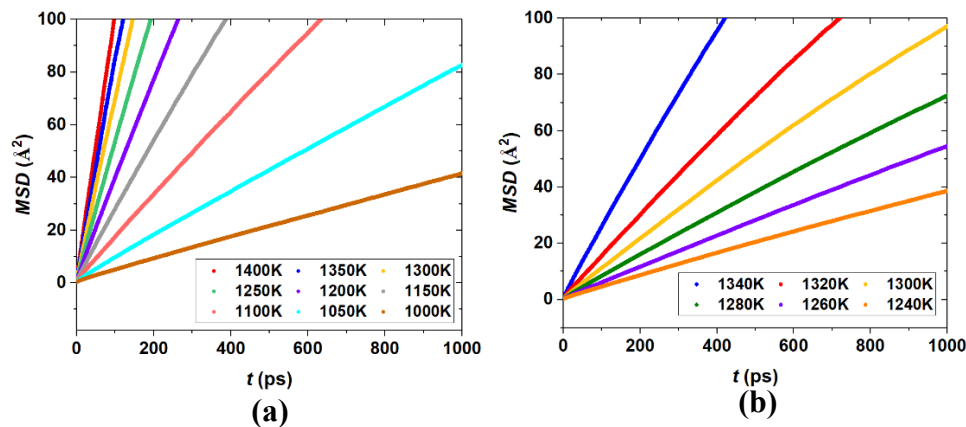
Figure S1. Mean square displacement against time of (a) metallic glass film terface (MGF60A-S) and (b) the interface of Crystalline Cu film with (110) crystallographic orientation (Cu111F-S) at different temperatures.

A.2 Debye-Waller Factor (DWF)

We estimate the DWF from the expression for the MSD of all the particles at the "caging" time, $t = 2ps$. The DWF is then defined as, $\langle u^2 \rangle = \langle \frac{1}{N} \sum_{n=1}^{N} \{(x_2 - x_0)^2 + (y_2 - y_0)^2 + (z_2 - z_0)^2\} \rangle$, where (x_0, y_0, z_0) and (x_2, y_2, z_2) are particle's initial and final positions after time $t = 2ps$, respectively, and N is the number of atoms. Initially, we determined the center of the films, which is the plane perpendicular to the thickness direction slicing the film into two equal pieces. We estimated $\langle u^2 \rangle$ by averaging over 1Å interval thickness slices along the thickness of all metallic glass films, starting from the center of the films. We chose appropriate thickness intervals for crystalline Cu films depending on the crystallographic orientations perpendicular to the thickness direction (i.e., the crystallographic orientation of the film surface) so that all intervals contain a significant number of atoms. For example, the distance between two consecutive (110) planes is ≈1.28Å. So, we determined $\langle u^2 \rangle$ of the interface of Cu film with surface crystallographic orientation (110) in every 1.28Å interval. Figure S2 shown the comparison of the normalized $\langle u^2 \rangle$ along the thickness at 1300 K for metallic glass and crystalline Cu films. In the core region of crystalline Cu films, all three crystallographic surface orientation have the same values of $\langle u^2 \rangle$, to within numerical uncertainty, and this value is also consistent with $\langle u^2 \rangle$ values estimated from the bulk Cu material at the same T. Similarly, $\langle u^2 \rangle$ for the core atoms of the metallic glass films are nearly identical to $\langle u^2 \rangle$ values estimated from the bulk metallic glass. The film core atoms of the metallic glass films are more mobile than the core atoms of crystalline Cu films at the same T.
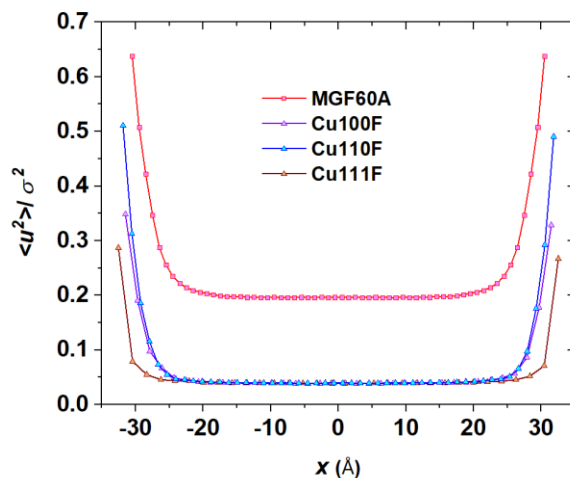
Figure S2. Comparison of the gradient in $\langle u^2 \rangle$, normalized by the square of the geometrical interparticle distance scale σ^2, as a function of distance in Å from the center of the film in at a common $T = 1300$ K for a metallic glass with thickness ≈ 60Å (MGF60A) and for a free-standing crystalline Cu film with a free interface having a (100), (110) and (111) orientations (Cu100F, Cu110 and Cu111F) and a thickness ≈ 64Å.

Figure S3 shows the normalized $\langle u^2 \rangle$ of the interface, core regions and the average value for the entire metallic glass films as function of temperature for the representative materials prescribed in the figure caption.
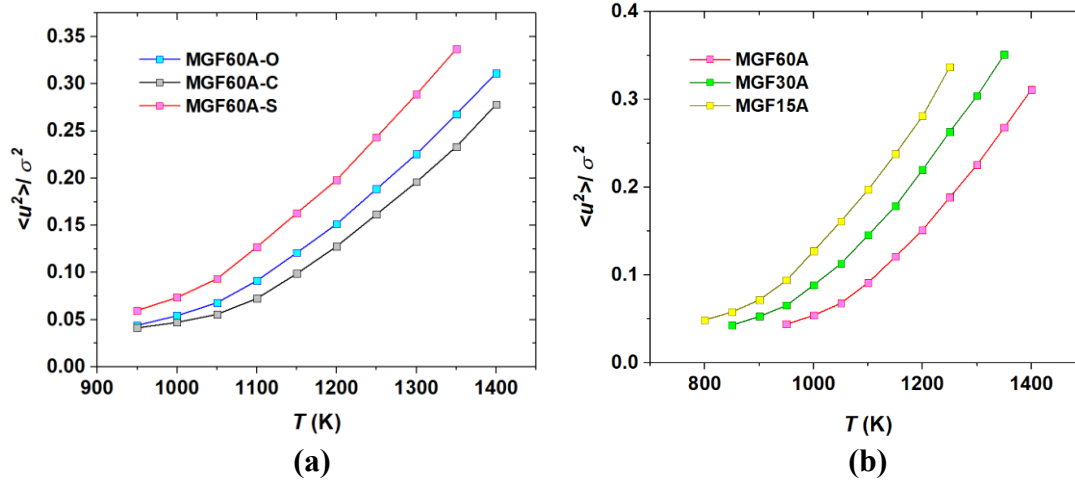
Figure S3. Illustrative plot of $\langle u^2 \rangle$ normalized by the square of the geometrical interparticle distance scale σ^2 **(a)** Interface and core regions of the metallic glass for the materials: ≈ 60Å (MGF60A-S, MGF60A-C and MGF60A-O), **(b)** Normalized $\langle u^2 \rangle$ averaged over entire film for metallic glass materials having a range of thicknesses: ≈ 60Å, ≈ 30Å and ≈ 15Å (MGF60A-O, MGF30A-O and MGF15A-O).
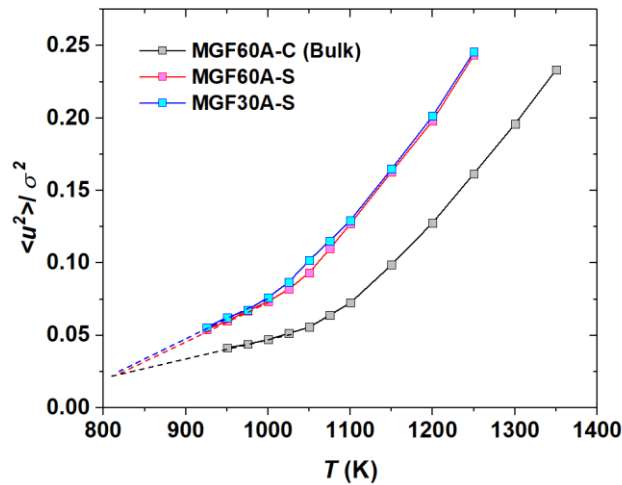
Figure S4. Illustrative plot of $\langle u^2 \rangle$ normalized by the square of the geometrical interparticle distance scale σ^2 for the interfacial mobile region of metallic glass films having thicknesses of 60Å and 30Å (MGF60A-S and MGF30A-S) for the "bulk" material, calculated from the inner film region (from the film center to 10Å on both sides along the thickness) of MGF60A. The $\langle u^2 \rangle$ for interfacial and core regions extrapolate to a common temperature (Tammann temperature), as found in the main text for the MGF50A-S and MGF40A-S materials.

A.3 Anisotropy of DWF

We only considered $\langle u^2 \rangle$ values averaged over all three spatial coordinates directions in the current manuscript and we are aware of earlier studies [59,60] indicating the components of $\langle u^2 \rangle$ can be different in plane that normal to the interface, because it is not clear how these asymmetries might be measured experimentally in the physically interesting case when the interfacial layer is thicker than an atomic layer. In Figure S5, we show the $\langle u^2 \rangle$ exhibits different values along different directions.

Interfacial dynamics along perpendicular and planar direction don't differ a lot for metallic glass films. However, interfacial dynamics vary significantly from planar to perpendicular direction depending on the crystallographic orientation of the film surface. Further study is needed to understand the anisotropic interfacial dynamics of films.
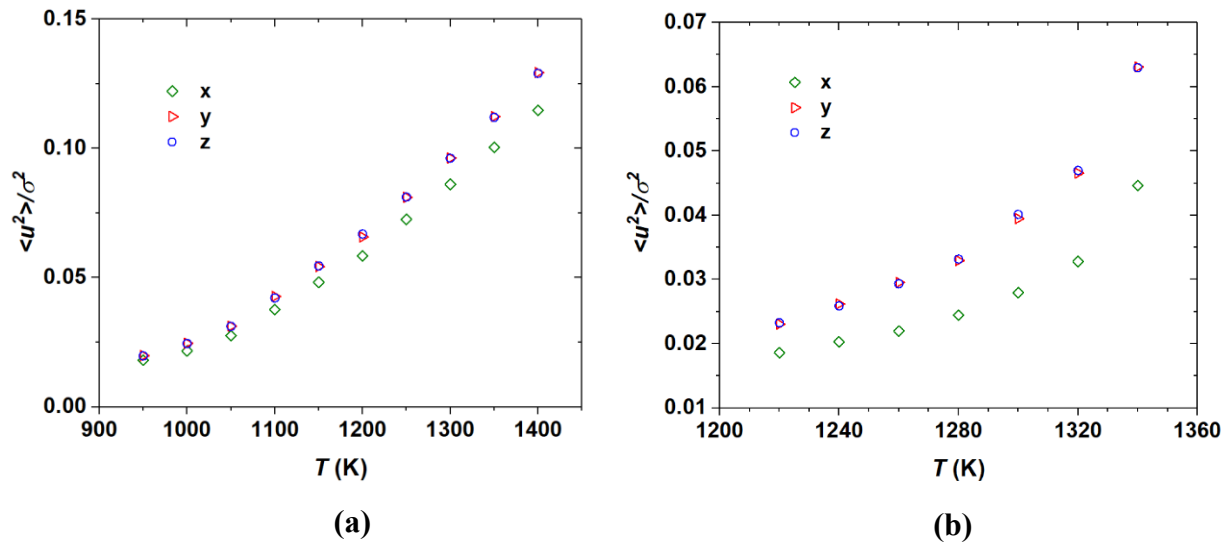
Figure S5. Debye-Waller $\langle u^2 \rangle$ factor as a function of temperature in different directions in **(a)** a metallic glass films with thickness ≈ 60 Å and **(b)** a crystalline Cu film with (100) surface orientation and thickness ≈ 64 Å.

A.4 Relaxation Time from Self-intermediate Scattering Function as a Function of Temperature

We determined the average structural τ_α from the self-intermediate scattering function $F_s(t)$ after fast beta relaxation regime to the equation, $F_S(q,t) \propto exp\left[(t/\tau_\alpha)^\beta\right]$ with the scattering wavevector fixed by convention to the interparticle separation distance. These fits at different T provide $\tau_\alpha(T)$ estimates where β varies with sample and T in a range between 0.35 and 0.7 for the simulation conditions studied. An Arrhenius curve showing τ_α for the representative metallic glass MGF60A is shown in Figure S6.
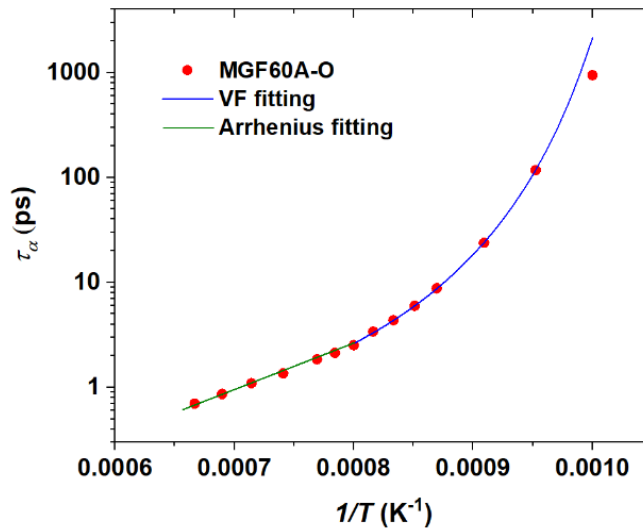
Figure S6. Structural or "alpha" relaxation time τ_α of the MGF60A-O with T. At T above the onset tempearture for non-Arrhenius relaxation T_A, the relaxation time τ_α follows an Arrhenius relation to a good approximation, and we fit our data in this T regime to the Arrhenius equation, $\tau_\alpha \sim exp\left(-\frac{E_A}{k_B T}\right)$. At temperatures below T_A, we correspondingly fit our τ_α data to the the Vogel-Fulcher-Tammann relation (VFT) [22] $\tau_\alpha \sim exp\left[-\frac{E_A T_0}{k_B(T-T_0)}\right]$, where E_A, T_0 and the proportionality constant τ_α are fitting parameters. In the comparison with the localization model (LM) [8], we only consider alpha relaxation times below T_A.

A.5 Decoupling Relation for Representative Metallic Glass Sample

We determined the decoupling exponent ζ from the Fractional Stokes-Einstein relation, $\frac{D}{T} \sim (\frac{1}{\tau_\alpha})^{1-\zeta}$. This scaling relation between D/T and τ_α is shown for an illustrative metallic glass (MGF60A-O) in Figure S7 where ζ is determined from the fitted slope in this plot. In general, we found ζ to range between 0.43 to 0.51 for our metallic glass samples. The decoupling exponent ζ was taken to equal $\zeta_{100} = 0.58$, $\zeta_{110} = 0.64$ and $\zeta_{111} = 0.41$ for the interfaces of crystalline Cu material (the subscripts represent the crystallographic orientation of the Cu film surface).
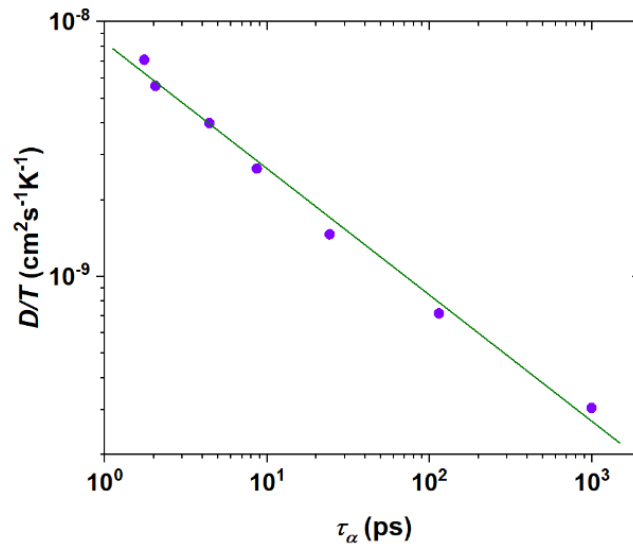
Figure S7. Fractional Stokes-Einstein or decoupling plot relating D/T to τ_α for MGF60A-O. In this representative example, the decoupling exponent ζ is estimated to equal, $\zeta = 0.51$.

A.6 Graphical Estimation of the Characteristic Temperature T_A

We determined the caging temperature T_A, which is an onset temperature in the glass-forming liquids following the same procedure described in our previous work for Cu-Zr metallic

glass systems. [14] Relaxation is Arrhenius above T_A and non-Arrhenius below T_A. According to the entropy theory of glass-formation activation enthalpy, the activation enthalpy $\Delta H_a(T)$ for the structural relaxation time τ_α follows a universal quadratic temperature relation, $\Delta H_a(T)/\Delta H_a(T_A) \approx 1 + C(T/T_A)^2$. This relation is restricted to a T range between T_A and crossover temperature T_c and T_A. The characteristic temperature T_c is a "crossover temperature" separating the high and low T regimes of glass-formation in which ΔH exhibits different T dependences. We determined T_A for all metallic glass systems by fitting to equation (5). T_A for MGTF60A (See Fig. S8) was found to be approximately 1195K, which is similar to our previous finding for the bulk form of this metallic glass. [14] T_A was found to be lower for thinner films metallic glass systems. For crystalline Cu thin films, T_A is assumed to equal the equilibrium melting temperature T_m, as mentioned in the text. Here, C is a constant describing "fragility" in the high temperature range of glass formation where the Vogel-Fulcher-Tammann relation no longer applies.
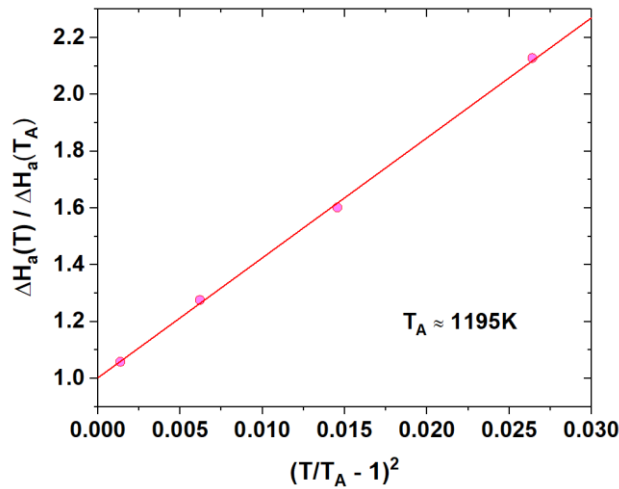

Figure S8. Reduced activation enthalpy, $\Delta H_a(T)/\Delta H_a(T_A)$, as a function of reduced temperature for diffusion coefficient of MGF60A-O.

A.7 Surface Thickness and λ

Figure S9 shows the λ, which provides a measure of average interfacial width, against temperature for MGF60A and MGF30A. This curve follows the trend similar to the calculated interfacial width versus temperature curve shown in Figure 2(a) of the main text.
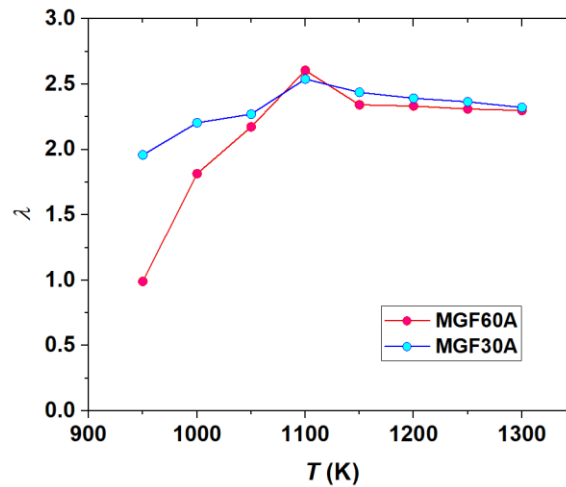

Figure S9. Constant λ obtained from the fitting of $\langle u^2 \rangle$ versus thickness curve using the equation $\langle u^2 \rangle / \sigma^2 = \langle u^2(core) \rangle / \sigma^2 + B\ exp(x/\lambda)$ against temperature for MGF60A and MGF30A.

A.8 Effective Dimensionality

Rhead suggested that the interfacial region is similar to a "quasi-two- dimensional fluid" rather than a crystal lattice with vacancies, etc. [276] This naturally explains why the diffusion in the interfacial layer is similar to a liquid near the melting temperature.
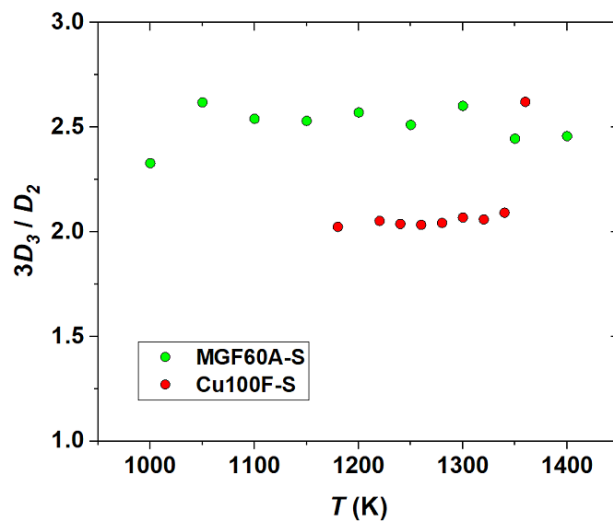
Figure S10. The effective dimensionality ($3D_3/D_2$) of metallic glass films with thickness $\approx 60\text{Å}$ and a crystalline Cu film with (100) surface orientation and thickness $\approx 64\text{Å}$. Effective dimensionality of metallic glass film is well above 2 in whole temperature range we studied but effective dimensionality of crystalline film is almost equal to 2 in all temperatures except at melting temperature. Therefore, metallic glass film interface always behaves 3-dimensional even in lower temperature but crystal film interface only behaves 3-dimensional at very high temperature.

Appendix B: Supplementary Information of Chapter 5

Supplementary Information: The Dynamics of Metal Nanoparticles on a Supporting Interacting Substrate

B.1 Cu NP on Graphene substrate

We started with putting a perfect Cu nanoparticle with 10,000 atoms on a graphene substrate and running energy minimization simulation to get the optimum distance between the graphene substrate and Cu NP. We started heating simulation at 300K; where Cu NP was in its perfect shape as shown in figure S1 (upper left). With increasing temperature, the adjacent side of the NP begins to flatten. Finally, it takes the domed shape after melting (1250K in the Figure S1).
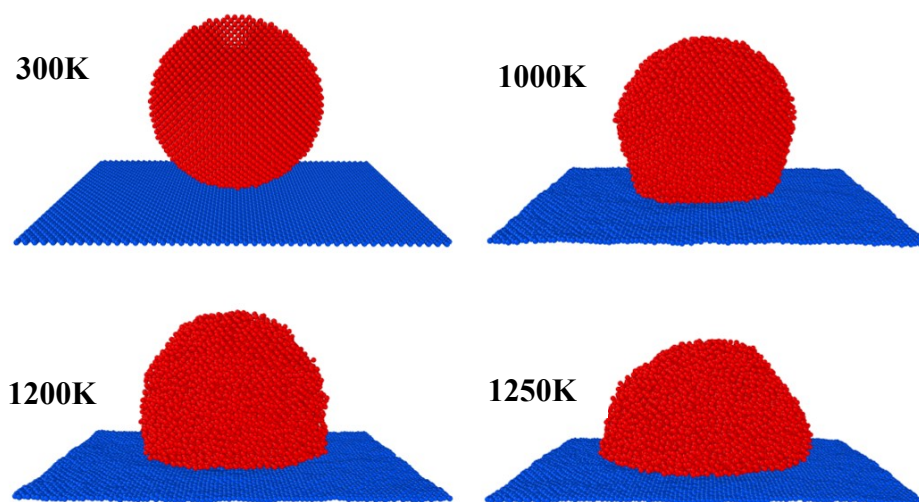
Figure S1: Initial configuration of Cu NP on graphene substrate at 300K (upper left), Cu NP on C with 3x interaction strength at 1000K (upper right), at 1200K (lower left) and at 1250K (lower right). Note that, the contact area between Cu NP and graphene substrate keeps increasing with increase in temperature. This increase in contact area strongly depends the interaction strength between Cu and C atoms.

B.2 Potential Energy versus *T* of Free-Standing and Supported Cu NPs

Figure (S2) shows the average potential energy of Cu atoms (PE) against approximate temperature. We have taken the time of the simulation to determine an "effective temperature" *T* because temperature fluctuations during the heating process are substantial. Melting temperature of NP is affected by the interactive supporting substrate.
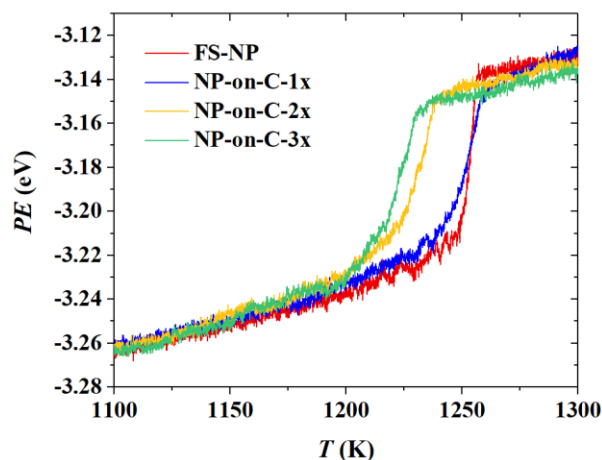

Figure S2: Average potential energy (PE) against approximate temperature (*T*) near melting temperature of free-standing Cu NP (NP-FS) and Cu NP on graphene with different strengths of Cu-C substrate interaction strength.

In order to find the exact melting temperature of the NP, we determined the average potential energy of Cu atoms in every 5 ps near melting temperature. Figure S3 (a) is showing the average potential energy of Cu atoms against temperature for free-standing and supported Cu NPs. Next, we calculated specific heat capacity from the slope of these curves as shown in the Figure S3 (b). The exact melting temperature is at the peak of the *Cp* against *T* plot.
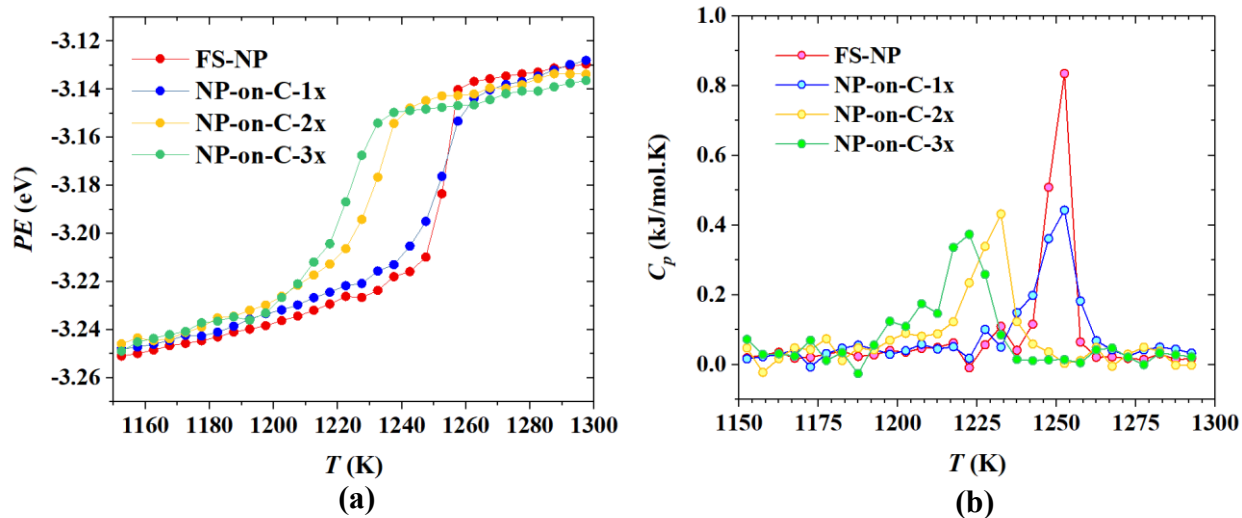
Figure S3: PE of Cu atoms in free-standing and graphene supported Cu NP near melting temperature averaged over every 5 ps (left). Specific heat capacity C_p derived from the potential energy (PE) as a function of T ($C_p = d(PE)/dT$).

B.3 Colored Noise in Potential Energy Fluctuations

Figure S4 shows the fluctuation of average potential energy of Cu-C interfacial Cu atoms of supported NP with 3x Cu-C interaction strength.
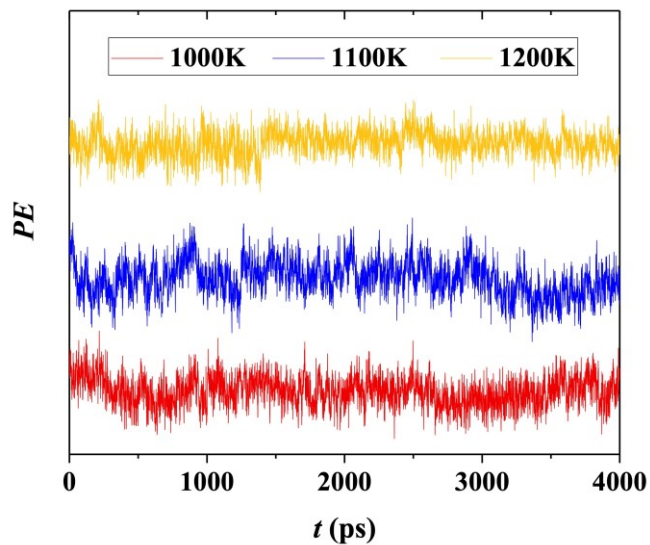
Figure S4: Potential energy fluctuations of atoms in the interfacial region of a NP supported C-3x substrate as a function of simulation t for at three temperatures.

B.4 Self-Intermediate Scattering Function

An example self-intermediate scattering function plot at a wide range of temperature of Cu-C interface part of Cu NP supported on graphene where interaction strength between Cu and C is 3x is shown in Figure S5.
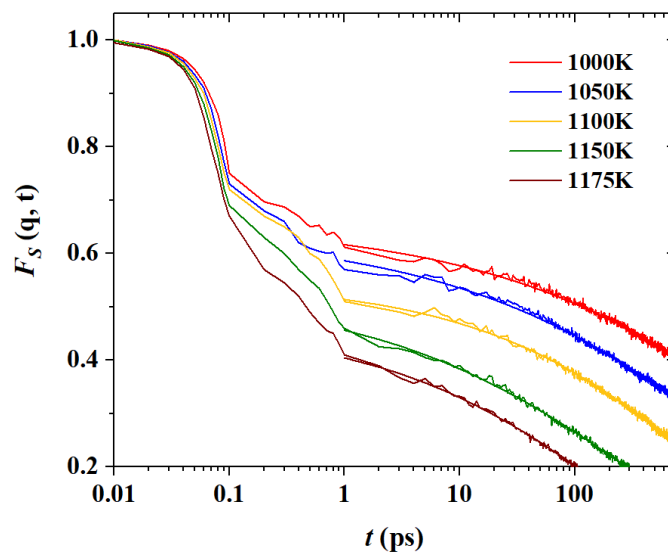
Figure S5: Self-intermediate scattering function plot of the Cu-C interfacial region when Cu-C interaction strength is 3x with the fitted lines.

B.5 Decoupling exponent

Decoupling exponents (ζ) are estimated from Fractional Stokes-Einstein (FSE) relation, $D/T \propto (1/\tau_\alpha)^{1-\zeta}$. A representative D/T against α-relaxation plot is given in Figure S6 below; where we found $\zeta = 0.57$ for the free surface of Cu NP supported on graphene with Cu-C interaction strength is 3x.
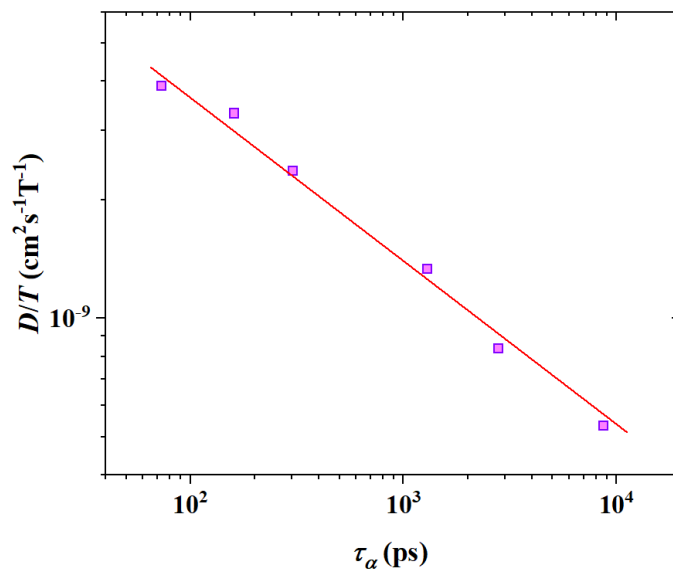
Figure S6: Fractional Stokes-Einstein or decoupling plot relating D/T to τ_α for the free surface of Cu NP supported on graphene with 3x interaction strength between Cu and C.